

PATH AND WAKE OF A RISING BUBBLE

Cover image: *Air bubbles from divers rising to the surface, Hawaii.*
Photo taken by Ed Robinson, underwater photographer.

ISBN 90 365 15262

Copyright © 2001 by A.W.G. de Vries, Enschede, The Netherlands

PATH AND WAKE OF A RISING BUBBLE

PROEFSCHRIFT

ter verkrijging van
de graad van doctor aan de Universiteit Twente,
op gezag van de rector magnificus,
prof. dr. F.A. van Vught,
volgens besluit van het College voor Promoties
in het openbaar te verdedigen
op donderdag 15 februari 2001 te 15.00 uur.

door

Antoine Wilhelmus Gerardus de Vries

geboren op 10 juni 1972
te Sittard

Dit proefschrift is goedgekeurd door de promotor:

prof. dr. ir. L. van Wijngaarden

en de assistent promotor:

dr. ir. A. Biesheuvel

TABLE OF CONTENTS

1	Introduction	1
1	Motivation	1
2	Outline	3
2	Previous work	5
1	Dimensionless numbers	5
2	Flow around a bubble	6
3	Path and shape instability	7
4	Contamination	12
5	Bubble-bubble and bubble-wall interactions	13
6	Wakes	14
7	Aim of thesis	16
3	Experimental method and Analysis tools	17
1	Water tank and bubble generation	17
2	Visualisation method	18
3	Temperature gradient effects	19
4	Image analysis	23
4	Free rising bubbles in quiescent water	29
1	Introduction	29
2	Results and Discussion	30
2.1	Straight rising bubble	30
2.2	Zigzagging bubble	32
2.3	Spiralling bubble	39
3	Wake	46
4	Strength of the wake	48
5	Conclusions	49

5	Shape effects	51
1	Introduction	51
2	Bubble release	51
3	Shape effects on the flow pattern	54
6	Bubble-Wall Interaction	57
1	Introduction	57
2	Experimental setup	58
3	Experimental results	60
3.1	Path of bouncing bubbles	60
3.2	Flow visualisation of bouncing bubble	65
4	Model	71
4.1	Free rising and attraction to wall	74
4.2	Collision	74
4.3	After collision	75
4.4	Adaptions to the model: misalignment and lift	77
5	Vortex and bubble near wall	79
6	Discussion and conclusions	81
7	Pseudo-turbulence in Bubbly Flows	83
1	Introduction	83
2	Volume fraction of Hill's spherical vortices	84
3	Turbulent excess energy	85
4	Conclusions	90
8	Conclusions and Recommendations	91
	<i>References</i>	95
	<i>Summary</i>	99
	<i>Samenvatting</i>	101
	<i>Acknowledgements</i>	104
	<i>About the author</i>	106

INTRODUCTION



1 Motivation

An important topic in fluid dynamics is multiphase flows. Multiphase flows can be found in numerous fields in engineering, e.g. aerospace, biomedical, chemical, electrical, environmental, mechanical, nuclear and naval engineering. There is an enormous variation in applications, e.g. rocket engines, chemical reactors, contamination spreading, multiphase mixture transport, cavitation, sonoluminescence, ink-jet printing, particle transport in blood, crystallisation, multiphase cooling, fluidized beds, drying of gases, air entrainment in oceans/ivers and anti-icing fluids. The number of papers on multiphase flow in the field of fluid dynamics is enormous and still growing. The diversity of flow types makes a general description almost impossible. This makes fundamental research necessary. Especially, controlled experiments are needed for a better physical understanding and as test cases for numerical and theoretical work.

In the group of L. van Wijngaarden and A. Biesheuvel one of the main subjects is bubbly flows. The work performed in this group covers numerous topics in this field. For negligible velocity differences between the phases equations for one-dimensional flow were proposed by van Wijngaarden (e.g. 1968, 1972). More general two-phase flow equations for a dilute dispersion of gas bubbles in liquid were derived by Biesheuvel & van Wijngaarden (1984). However these equations did not contain bubble interaction terms. The hydrodynamic interactions between gas bubbles in liquid were studied by van Wijngaarden (1976) and the effects on the main rise velocity for pairwise interacting bubbles by van Wijngaarden (1993). Biesheuvel (1984) and van Wijngaarden & Kapteyn (1990) focussed on the effects of bubble interactions on the stability of concentration waves at low gas volume concentrations. Lammers & Biesheuvel (1996) examined the stability of bubbly flows and the propagation of void fraction waves. Numerically dilute bubble mixtures were studied by Bulthuis (1997). Duineveld (1994,1995) and Kok (1993a,b) performed experiments on single bubbles and bubble pairs in pure water and water contaminated with a well-defined amount of surfactants. The paths of the bubbles, observed in these

experiments, could not be explained and hence more research was necessary. Especially three dimensional information of the position and shape of the bubble and the configuration of the wake behind the bubble was lacking. Another recent research area in the group is bubbles in turbulence, e.g. Spelt & Biesheuvel (1997,1998) and Poorte (1998). Closely related is the modification of turbulence by bubbles, often called pseudo-turbulence (van Wijngaarden 1998).

From all previous research, the lack of knowledge about the relation between the dynamics of a single bubble and its wake became obvious. Although many papers have been published on this subject, the results contradict each other in many aspects. Perhaps because experimental data on bubble paths reported in literature (e.g. Saffman 1956, Lunde & Perkins 1995, Aybers & Tapucu 1969a,b, Mercier, Lyrio & Forslund 1973 and Ellingsen 1998) was gathered in contaminated water and/or with a repetitive bubble production mechanism in which bubble paths are influenced by the preceding bubbles. Indeed, even the release of the bubble from the needle was not smooth in most experiments, forcing the bubble's deformation at release.

Considering the fact that in contaminated water, bubbles behave as solid particles, the comparison of the wake of a bubble to that of a solid sphere seemed logical. Dye visualisations by Lunde & Perkins (1997), Laser Doppler Anemometry (LDA) measurements by Ellingsen & Risso (1998) and Particle Image Velocity (PIV) measurements by Brücker (1999) claimed to prove that the wakes of bubbles and solid spheres are similar. However, the experimental methods used indicate that these measurements were performed in contaminated liquids. As long as visualisations or measurements of the wake behind bubbles in pure water do not exist, the relevance of these results to the case of pure water remains questionable. Similarly, the analogy to the wake behind drops in liquids (Magarvey & Bishop 1961) is not obvious.

Numerical results of Blanco & Magnaudet (1995), Takagi, Matsumoto & Huang (1997) and Ryskin & Leal (1984) show the wakes behind bubbles for axisymmetric flows. Considering the fact that the standing eddy in the wake behind the bubbles observed in these simulations occurred first in a regime in which the path of the bubble observed in experiments was already unstable, the wake instability has to be of a different kind than for solids where the standing eddy becomes unstable. Numerical simulations of the flow around bubbles are highly demanding by the accuracy needed to resolve the shape of the bubble and the zero stress condition on the bubble's surface. The local curvature determines the pressure jump over the bubble interface and as a result a strong coupling between flow and shape exists. For numerical work this makes life complicated.

This thesis focuses on the dynamics of a single rising bubble in pure quiescent water. The main problems involved are the bubble production and release, the unknown shape of the bubble, the path instability, the wake configuration and dynamics, the purity of the water and the interactions with boundaries. To the best of our

knowledge no research has been performed on bubble motion in pure water where simultaneously the three dimensional path, shape and wake of a bubble are visualised. This study fills that gap. The production of pure water and of bubbles was the same as described in Duineveld (1994). The visualisation technique is a two-way Schlieren system using the refractive index differences between water and air and the temperature dependent refractive index of the water. Analysing both perpendicular views in time results in the three dimensional position, velocity and shape of the bubble.

2 Outline

In chapter 2 the results of previous experimental, theoretical and numerical research on bubble dynamics are summarised. The emphasis is on single bubbles. In chapter 3 the experimental Schlieren setup visualising both the bubble outline and wake is described. The results for free rising bubbles are presented in chapter 4. A tentative explanation for the zigzagging and spiralling of the bubbles is given which takes into account the observed structures of the wake. In chapter 5 some aspects concerning the shape of bubbles at release and free rising are discussed. Our numerical calculations show the influence of the deformability of the bubble's surface on the nature of the wake.

In chapters 6 and 7 the results obtained for the single, free rising bubble are used to explain a number of phenomena observed in multiphase flows. In chapter 6 experiments are reported for bubbles bouncing against a vertical wall. A model, based upon potential flow theory, is used to explain the bouncing phenomena observed in experiments. In chapter 7 a model for pseudo-turbulence is proposed based on the results found for bouncing and free rising bubbles. The effect of the vorticity produced by the bubbles, arranged in vortical regions, on the excess turbulent energy is calculated.

The main conclusions are summarised in chapter 8 and a number of recommendations for future work are given.

PREVIOUS WORK



In this chapter the results of the references frequently used in this thesis are summarised and put into perspective. A comparison between these references is given and the main questions remaining are addressed. For a more extensive review of previous work Clift et al. (1978) and Magnaudet & Eames (2000) form good starting points.

1 Dimensionless numbers

Consider a gas bubble rising in a liquid. Its behaviour, of course, will depend on the physical properties of the surrounding liquid. These are the density ρ , the kinematic viscosity ν and the surface tension coefficient σ . The bubble rises due to the buoyancy force which is related to the gravitational acceleration g and the volume of the bubble V ; with the latter an equivalent radius r_{eq} can be associated, which is defined by

$$r_{eq} = \left(\frac{3V}{4\pi} \right)^{1/3}, \quad (2.1)$$

i.e. the radius of a sphere with the same volume as the gas bubble.

It follows that the (mean) terminal rise velocity of the bubble U_T is a function of 5 variables,

$$U_T = U_T(r_{eq}, g, \rho, \nu, \sigma), \quad (2.2)$$

and dimensional analysis then shows that 3 dimensionless groups, 2 independent and 1 dependent, describe the phenomenon. As independent parameters the Morton number Mo and the Eötvös number Eo are usually chosen. These are defined as

$$\begin{aligned} Mo &= \frac{g\nu^4\rho^3}{\sigma^3} \\ Eo &= \frac{4\rho r_{eq}^2 g}{\sigma} \end{aligned} \quad (2.3)$$

The Morton number only contains physical properties of the fluid. Fluids can now be arranged in two separate groups, those with high Morton numbers ($Mo > 10^{-2}$) and those with low Morton numbers ($Mo < 10^{-6}$). Water has a Morton number of $1.1 \cdot 10^{-11}$, so in this thesis we will only be concerned with the behaviour of bubbles in low Morton number fluids.

The Eötvös number is basically a measure of the volume of the bubble, so that a functional relationship between a parameter and the Eötvös number describes how that parameter changes with the volume of the bubble.

The choice of the dependent parameter depends on what one is interested in. The most common ways of defining a dimensionless rise velocity are e.g. the Reynolds number

$$Re = \frac{2U_T r_{eq}}{\nu}; \quad (2.4)$$

the Weber number

$$We = \frac{2\rho U_T^2 r_{eq}}{\sigma}; \quad (2.5)$$

the Froude number

$$Fr = \frac{U_T^2}{2gr_{eq}}; \quad (2.6)$$

or the drag coefficient

$$C_D = \frac{8gr_{eq}}{3U_T^2}. \quad (2.7)$$

Of course, these numbers can be expressed in terms of the others:

$$\begin{aligned} Re &= We^{1/2}(Eo/Mo)^{1/4}; & We &= \frac{4}{3}Eo/C_D; \\ Fr &= We/Eo; & C_D &= \frac{4}{3Fr} = \frac{4MoRe^4}{3We^3}. \end{aligned} \quad (2.8)$$

2 Flow around a bubble

Our interest is mainly in bubbles that rise in low Morton number fluids, such as water, at high Reynolds numbers, between 200 and 900, say. In that case the bubbles have an approximately spherical shape at the lower bound of the Reynolds number range, while they rise in a rectilinear path. For the higher bound of the Reynolds number range, the bubble shape is that of an oblate ellipsoid and bubbles rise in an irregular, zigzagging or spiralling, fashion.

At these high Reynolds numbers, vorticity is confined to the thin boundary layers and wakes, and a good description for the flow field can be obtained from potential flow theory.

Levich (1962) calculated the viscous dissipation in the potential flow around a sphere to obtain a first approximation to the drag coefficient. This analysis was

extended by Moore (1963, 1965) who (partially) solved the appropriate equations in the rotational flow regions to obtain improved estimates for the drag coefficient of spheres and oblate ellipsoids. Moore's expansion reads

$$C_D = \frac{48}{Re} G(\chi) \left[1 + \frac{H(\chi)}{Re^{1/2}} + \mathcal{O}\left(\frac{1}{Re^{1/2}}\right) \right], \quad (2.9)$$

with χ the aspect ratio of the bubble, and $H(\chi)$ and $G(\chi)$ functions that are given in analytical or tabulated form in Moore's papers. For a spherical shape, $\chi = 1$, this leads to $C_D = 48/Re$.

Moore's analysis shows that the flow in the boundary layer of thickness $\mathcal{O}(Re^{-1/2})$ is described by a balance between convection along the streamlines of the primary potential flow and viscous diffusion across these streamlines of a quantity known as the 'circulation density' $\Omega = \omega/m$, i.e. the ratio between vorticity and distance from the symmetry axis. In the part of the boundary close to the rear stagnation point viscous effects become unimportant. The circulation density is then merely convected, while being stretched, into a narrow wake of thickness $\mathcal{O}(Re^{-1/4})$. For future reference we note that the vorticity in that part of the boundary layer around a spherical bubble is given by

$$\omega = -\frac{3mU}{a^2} \operatorname{erfc}\left(\frac{3ym/a^2}{4\sqrt{2}}\right) \quad (2.10)$$

where a is the radius of the sphere, m is the distance from the symmetry-axis and $y = (r - a)/a$, the dimensionless radial coordinate.

3 Path and shape instability

At low Reynolds numbers a bubble moves rectilinearly, while at higher Reynolds numbers oscillatory motions, as spiralling and zigzagging, are observed. Furthermore, the shape of the bubble is said to be stable for low Weber number and becomes oscillatory, or unstable, for larger Weber number ($\mathcal{O}(3)$). The onset of path instability and that of shape instability are, in general, and also for bubbles in pure water, occurring at different stages.

The spiralling (also called helical) motions of axisymmetric solid bodies in a perfect fluid are well understood and described by Lamb (1932). Solid bodies with angular inertia about their axis of symmetry have an infinite range of possible helical motions. Within a Hamiltonian description, a bubble in spiralling motion has to have a non-zero impulsive couple. With the use of a variational characterisation the path of bubbles can be determined within the Hamiltonian theory developed by Benjamin (1987). In this theory it is assumed that the ideal-fluid theory is applicable for the motion of bubbles including surface tension in liquids of small viscosity. In the region

in which the Weber number is decisive for stability, the ideal-fluid model has been proven to be a valid assumption by e.g. Saffman (1956), Hartunian & Sears (1957), Moore (1965) and Miksis *et al.* (1981).

After formulating the Hamiltonian, Benjamin (1987) describes several invariants, e.g. energy E , impulse I , impulsive couple L , volume V and virial W . When the shape of the bubble becomes oscillatory the shape is said to be unstable. For a steady motion the maximum Weber number for shape instability is found to be $We_{max} = 3.271$, with an aspect ratio of the bubble's axes of $\chi = 3.722$. This can be compared with the numerical results of Miksis *et al.* (1981) ($We_{max} = 3.23$ at $\chi = 3.85$). The expression for the Weber number of Benjamin (1987) is more accurate than the results of Moore (1965) who satisfied the boundary conditions at the poles and equator only. The maximum Weber number for shape instability is remarkably close to the experimentally determined critical Weber number ($We_{cr} = 3.17$) for path instability by Hartunian & Sears (1957). Benjamin (1987) conjectured that the maximum Weber is associated with a bifurcation from the class of axisymmetric conditional extrema into non-axisymmetric ones. However, it has to be noted that shape instability is not necessarily the trigger for path instability (Duineveld (1994)).

Moreover, Benjamin¹ (1987) showed that the helical path to leading order in s ($s = \sin(\sec^{-1}(\chi))$) is described by the translation velocity of the bubble, U , the spiral radius, R , the pitch, $2\pi U/\Omega_B$, and pitch angle, θ , as

$$\frac{R}{r_{eq}} = \frac{\sqrt{3}}{10}s^3 \sin 2\theta, \quad (2.11)$$

$$\frac{U}{\Omega_B r_{eq}} = \frac{2}{3\sqrt{3}}s. \quad (2.12)$$

The initial motion of a bubble is rectilinear, i.e. without impulsive couple. For larger bubbles this rectilinear motion becomes unstable resulting in a spiralling or zigzagging motion. Benjamin's Hamiltonian theory indicates that a spiralling motion can exist if, and only if, a non-zero impulsive couple exists. As the impulsive couple is an invariant there is a contradiction, which is addressed in chapter 4. Symmetry breaking of the wake of the bubble plays an important role.

The onset of path instability is generally believed to occur at a critical Weber number, We_{cr} , which depends on the fluid properties. Duineveld (1994), Tsuge & Hibino (1977) and Maxworthy *et al.* (1996) found a lower critical We for lower Mo number, which is also observed in our experiments (see Chapter 4). A useful relation is the increase of the critical Reynolds number for decreasing Morton number. Tsuge

¹For a spiralling motion Benjamin (1987) found that there has to be an angle between the short axis of the bubble and the direction in which the bubble is travelling. In experiments this angle has never been observed, however, it might be present as it will be very small and its value could be within measuring accuracy.

& Hibino (1977) determined these functions empirically as

$$We_{cr} = 21.5Re_{cr}^{-0.32}, \quad (2.13)$$

$$Re_{cr} = 9.0Mo^{-0.173}, \quad (2.14)$$

where Re_{cr} is the critical Reynolds number for the onset of path instability.

For low Morton numbers fluids like water, Maxworthy *et al.* (1996) showed that the smallest drag coefficient of a bubble can be described by $C_d = 11.1Re^{-0.71}$. For $Re < 60$ (small bubbles) the drag coefficient is comparable to that of a solid sphere with the same volume. Impurities may play an important role. For large Re (≈ 600) the bubble can also have a drag coefficient larger than that of a solid sphere because of deformation. So the drag coefficient can be influenced by impurities and shape effects. From this the claim is sometimes made that a sufficient check for the purity of the water would be the terminal rise velocity of the bubble. Although the drag coefficient might be correct, the motion of the bubble, the mobility of the bubble surface and the flow around the bubble might be influenced by a small amount of impurities (see § 4).

For increasing Reynolds number, the drag coefficient is decreasing up to the point where minimum drag coefficient is reached. This is followed by a constant We regime, which starts at approximately the maximum of Fr^2 and is associated with We_{cr} for path instability. This is not to be confused with the We_{max} for the shape instability.

Hartunian & Sears (1957) studied, both experimentally and theoretically, the path instability of small gas bubbles moving in various liquids and reported a stability curve. They determined two separate criteria for the onset of path instability in various liquids, $Re_{cr} = 202$ and $We_{cr} = 3.17$. The first criterion is for solid spheres, bubbles in contaminated fluids, and bubbles in viscous liquids, and the second criterion is for bubbles in clean liquids. Obviously this unique value of We_{cr} is not in agreement with the dependence of We_{cr} on Mo (Equation 2.13 and 2.14). Furthermore, they determined that in liquids for which $Mo > 10^{-4}$ the bubble path does not become unstable. As for solid spheres and bubbles in pure water, different dimensionless numbers appear to indicate the transition; it is most likely that different phenomena trigger this transition.

Saffman (1956) studied the path and the onset of path instability in detail and observed that for $r_{eq} < 0.7$ mm the path is straight, for larger radii up to $r_{eq} = 1.0$ mm only zigzagging bubbles were found. For bubble radii larger than 1.0 mm both spiralling and zigzagging were observed. Bubbles released rapidly after each other followed each other's path, however for $r_{eq} < 1.0$ mm zigzagging bubbles always zigzagged even when released in a spiralling bubble's wake. Saffman determined $Re_{cr} = 400$ for path instability. Furthermore, Saffman observed no difference in the rise velocity of spiralling and zigzagging bubbles of equal size. As a trigger of the

	Summary of observed path and transition criteria			Remarks
	straight	spiral	zigzag	
Haberman & Morton (1954)	$Re < 300$	$300 < Re < 3000$	$Re > 3000$	no zigzag but rocking
Hartunian & Sears (1957)	$Re < 202$ $We < 3.17$	$Re > 202$ $We > 3.17$	$Re > 202$ $We > 3.17$	solids/contaminated pure, $Mo < 10^{-4}$
Saffman (1956)	$r_{eq} < 0.7$ mm $Re < 400$	$r_{eq} > 1.0$ mm ?	$r_{eq} > 0.7$ mm $Re > 400$	
Aybers & Tapucu (1969a,b)	$r_{eq} < 0.67$ mm $Re < 565$	$0.67 < r_{eq} < 1.0$ mm $565 < Re < 880$	$r_{eq} = 1.00$ mm $880 < Re < 1350$	
Duineveld (1994,1995)	$r_{eq} < 0.91$ $We < 3.3$ $Re < 662$	- - -	$r_{eq} > 0.91$ $We > 3.3$ $Re > 662$	

TABLE 2.1: Summary of previous results for the onset of path instability and the regimes of the observations.

path instability Saffman proposed a shape instability at the front of the bubble. Later this shape instability has been observed in numerical simulations, but this was always claimed to be due to numerical instabilities.

Aybers & Tapucu (1969a,b) saw similar transition stadia as Saffman (1956); however, they observed only spiralling bubbles for $0.67 \text{ mm} < r_{eq} < 1.0 \text{ mm}$, instead of the zigzagging bubbles seen by Saffman. This certainly indicates something peculiar is happening in this range, which deserves more attention. Furthermore, the shape of the bubbles was found to be spherical up to $r_{eq} = 0.42 \text{ mm}$, ellipsoidal up to 1.0 mm , and for larger sizes shape oscillations were observed. The transition ranges for the path were also characterised in terms of the Reynolds number: $Re < 565$ rectilinear; $565 < Re < 880$ helical; $880 < Re < 1350$ first zigzag then helical; $1350 < Re < 1510$ zigzag and then rectilinear rocking motion. Shape oscillations started at $We = 3.7$ or $\chi = 2.0$.

More experimental work on bubble motion was performed by Haberman & Morton (1954). They observed rectilinear ($Re < 300$), helical and rocking motions. The helical path could be either clockwise or counterclockwise, depending on the conditions of generation. The major axis of the bubble is always directed perpendicular to the direction of motion. Contamination of the water would lead to a solid-sphere-like behaviour up to $Re = 300$. Minute particles are expected to concentrate on the bubble's surface immobilising it. The non-rectilinear motion was assumed to be caused by a periodic vortex shedding, as in the case of solid spheres. However, in Chapter 4 it will be shown that no vortex shedding is observed for spiralling or for zigzagging bubbles.

The simulations for axisymmetric flows of Ryskin & Leal (1984), using a boundary-fitted coordinate system, were performed in the regime of $Re < 200$ and $We < 20$, which means well outside the regime of path instability in water. They did observe a standing eddy - a recirculation zone behind the bubble - in parts of

	Observed shapes and onset of shape instability		
	spherical	ellipsoidal	instable
Aybers & Tapucu (1969a,b)	$r_{eq} < 0.42$ mm	$r_{eq} < 1.00$ mm	$r_{eq} > 1.00$ mm
			$\chi > 2$ $We > 3.7$
Haberman & Morton (1954)	$Re < 400$	$400 < Re < 5000$	
Miksis <i>et al.</i> (1981)			$We > 3.23$
			$\chi > 3.85$
Ryskin & Leal (1984a,b)	contaminated liquids		$Re > 200$
	pure liquids		$We > 3 - 4$
Duineveld (1994,1995)			$We > 4.2$
			$r_{eq} > 1.34$ mm
Benjamin (1987)			$We > 3.271$
			$\chi > 3.722$

TABLE 2.2: Summary of results from previous work for the shape of the bubble and the onset of shape oscillations.

the regime. The differences between solid spheres and bubbles were believed to be associated to the large differences in the moments of inertia. They determined $Re_{cr} = 200$ for contaminated liquids and solids and $We_{cr} = 3 - 4$ for pure liquids, which is in agreement with the experimental results of Hartunian & Sears (1957). They also argued that vortex shedding will only occur for a clean bubble when two conditions are fulfilled: $We > We_{cr}$ and a standing eddy is present.

Miksis *et al.* (1981) determined the deformation of an axisymmetric bubble or drop in a uniform flow of constant velocity and determined $We_{cr} = 3.23$ at $\chi = 3.85$ for shape instability. After We_{cr} is reached We starts decreasing and asymptotically approaches $We \approx 2.3$.

Lunde & Perkins (1995) proposed a method for analysing the path and shape of a bubble obtained from experimental data using Fourier transformation of the outline of the bubble. All necessary information of the bubble is directly available from the determined Fourier Descriptors. They observed a mode-2 shape oscillation in both perpendicular views separately and deduced a mode-2 shape oscillation for the bubble. Later in this thesis it will be argued that they were probably misled by the projection of the bubble in these views, and that a thorough analysis of the orientation of the bubble would result in the disappearance of this mode-2 shape oscillation. Time-resolved information on the path is necessary as it will be assumed that the major axis of the bubble is directed perpendicular to the direction of motion at all times. In addition to this, Lunde & Perkins (1997) visualised the bubble wake using a dye. They concluded that there is a strong relation between the structure of the wake and the observed path. The wake of spiralling bubbles was continuous while the wake of zigzagging and rocking bubbles was intermittent. More about the observations in the wakes of bubbles can be found in section 6. It has to be emphasised that, although for these large bubbles the influence of the contamination on the rise velocity is low,

the water is contaminated by the dye.

Duineveld (1994,1995) studied the path and shape of bubbles ($0.33 \text{ mm} < r < 1.00 \text{ mm}$) experimentally. He found agreement with the theoretical results of Moore (1963, 1965) for the functional relationship between the rise velocity and the equivalent radius, provided the overestimation of the deformation in the theory is compensated for. These studies reported a $We_{cr} = 3.3$ for path instability in clean water. It is also emphasised that the agreement for the critical Weber number for path and shape instability is a pure coincidence. The path instability sets in at $r_{eq} = 0.91 \text{ mm}$ and only zigzagging bubbles are observed in single-view recordings.

The results of several experimental, numerical and theoretical studies for the onset of path and shape instabilities are summarised in Tables 2.1 and 2.2.

4 Contamination

The behaviour of bubbles changes significantly as soon as fluids become contaminated with surfactants. This change is related to the fluid properties and the type and level of contamination. Haberman & Morton (1954) showed that for contaminated water the critical radius, where the first path instability sets in, decreases, as does the maximum rise velocity and Re_{cr} . Hartunian & Sears (1957) and Ryskin & Leal (1984a,b) showed that, for a contaminated system, the stability curve is not determined by a critical Weber number but by $Re_{cr} = 200$, as is observed for solid spheres. Bel Fdhila & Duineveld (1996) determined that the rise velocity of a bubble stays roughly equal to its value for pure fluid up to a critical surfactant concentration. Above this concentration the drag rapidly increases towards the solid sphere drag. They also observed the transition for the path instability at $Re = 203$ for contaminated bubbles.

McLaughlin (1996) adapted the numerical method of Ryskin & Leal (1984) to take into account contamination. For the pure water case comparison with Duineveld (1995) was made and no attached wake was observed for $Re=637$ and $We=3.17$. In none of the simulations for clean interfaces flow separation was observed. For contaminated water a standing eddy is already observed for $Re=110$, $We=0.166$ and flow separation is observed. This clearly shows the differences in the wake behind bubbles in pure and contaminated water.

Most of the experiments mentioned in section 3 were performed in water that was not perfectly clean. This is especially true for the experiments involving wake visualisation. A logical consequence is that many results were similar to phenomena observed for solid spheres. To clarify that for pure water totally different phenomena play a role, some observations of solid spheres and drops are also summarised in section 6.

5 Bubble-bubble and bubble-wall interactions

The interaction between two bubbles has been studied by Biesheuvel & Van Wijngaarden (1982), Kok (1993a,b) and Duineveld (1994). The last author determined a critical Weber number for the transition between coalescence and bouncing, which is $We_{cr} = 0.18$ based on the approach velocity. At a We_{cr} of 2.6, based on the rise velocity, there is a transition between bouncing and bouncing followed by separation. Duineveld observed coalescence, bouncing, and bouncing separation for different bubble sizes. The minimum bubble size for bouncing separation (0.86 mm) is close to the critical size for path instability (0.91 mm). He argued that this size could be slightly lower because the large distortion at the bounce triggers vortex shedding, which he assumed to be the cause of zigzag motion.

Van Wijngaarden (1993) performed potential flow calculations on a collection of small spherical air bubbles. For this thesis especially the analysis of the relative motion of two bubbles (Biesheuvel & Van Wijngaarden (1982)) is relevant. For two rising bubbles with their centres horizontally aligned the relative motion can be described by

$$\left(\frac{dR}{dt}\right)^2 = \frac{3}{16} \frac{r_{eq}^3 U_\infty^2}{R_m^3} \left[\left(\frac{R_m}{R}\right)^3 - 1 \right], \quad (2.15)$$

with $2R_m$ the initial distance of the bubbles, $2R$ the distance between the bubble centres and U_∞ the vertical velocity of a single bubble at $t = 0$. U_∞ can be chosen arbitrarily and determines the kinetic energy of the system. The maximum approach velocity of each bubble will be $\sqrt{3/16}U_\infty \approx 0.43U_\infty$. The general equations of motion of a pair of spheres are given by Kok (1993a, equations 28 and 29). These equations are also applicable for the motion of a single spherical bubble close to a wall (Chapter 6).

Experimental setups are necessarily bounded by walls. For bubbly flows there can be a large region in which bubbles interact with walls. Tsao & Koch (1997) studied the interaction of bubbles (0.5 – 0.7 mm) with a rigid wall. Bubbles were observed to bounce several times against a horizontal wall. Collision dynamics can be explained by the exchange of energy between the various forms, e.g. kinetic energy, surface energy and potential energy.

For an inclined wall (10 – 85° with respect to the horizontal direction) a critical angle of 55° was observed. For an angle larger than 55° a bubble bounced repeatedly with constant bounce amplitude. This critical angle corresponds to a critical Weber number based on the velocity parallel to the wall of 0.4. For smaller angles, or smaller Weber number, the bubbles were observed to slide along the wall. At each bounce typically 59% of the bubble's energy was dissipated. For the sliding motion a lift force, balancing buoyancy which pushes the bubble towards the wall, is expected. Furthermore the coalescence of a bubble rising towards a stationary bubble was ob-

served for $We < 1.6$. This critical Weber number based on the total velocity is not in agreement with the bouncing criterion ($We = 2.6$) for horizontally aligned bubbles determined by Duineveld (1994), though Duineveld concluded that this criterion might be lower for vertically aligned bubbles.

Very intriguing phenomena are observed for a bubble bouncing with a vertical wall. With increasing size, a bubble tends to slide along a wall, to bounce repeatedly, to bounce once and never return, or to start a repetitive bounce again. The bounce height can be larger than the initial separation. In this thesis experiments on this subject will be presented and a model explaining these motions will be posed (Chapter 6).

In many applications multiple bubbles are present. A free rising bubble swarm of ellipsoidal bubbles was studied by Stewart (1995) in which the wake was observed to be the driving force and the sole mechanism for binary bubble interactions. Bubbles approached each other in the wake and then the rear one overtook the front one. For multiple bubble interaction the bubbles were observed to form clusters or chimney like patterns. This latter may be the basic dynamics of flow regime transition and excess energy dissipation in bubbly two-phase flow (Chapter 7).

The excess turbulent energy production by bubbles in turbulent flows was measured by various authors. Theofanous & Sullivan (1982) did experiments in the centre of a horizontal pipe and Lance & Bataille (1991) in grid turbulence in a vertical pipe. In Chapter 7 the results concerning the excess turbulent for increasing void fraction are shown to be comparable. The modification of turbulence by bubbles is often called pseudo-turbulence. A first tentative explanation of this phenomenon was based on the rise of isolated non-spherical bubbles described by potential flow theory with the vorticity confined in thin boundary layers, and presented by van Wijngaarden (1998). In Chapter 7 this model was extended to take into account vorticity confined in the wake.

6 Wakes

Experimentally the study of bubble wakes has been mainly performed by dye visualisation (Lunde & Perkins 1997), LDA (Ellingsen & Risso 1998) or by PIV (Brücker 1999). In these studies, vortex shedding is observed for zigzagging bubbles, similar as is observed for solid spheres. For spiralling bubbles, Lunde & Perkins (1997) observed a double threaded wake and emphasised that this would consist of two counter-rotating vortex filaments. To resolve the wake with these techniques a large amount of particles/dye is needed. It is most likely that these techniques contaminate the water; the validity of these results for clean water is questionable. Contamination might explain the similarity of the wake structure for these zigzagging bubbles and that of solid spheres.

Numerically, especially the works of Ryskin & Leal (1984a,b), Takagi *et al.* (1997), and Blanco & Magnaudet (1995) are interesting, because they all report on the formation of an attached, or standing, eddy behind a strongly deformed bubble. Ryskin & Leal concluded that for vortex shedding to occur with clean bubbles two conditions have to be satisfied: i) a standing eddy behind the bubbles, and ii) $We > We_{cr}$. From the numerical work of Blanco & Magnaudet (1995) and McLaughlin (1996), however, it can be deduced that no standing eddy will exist behind a bubble in the regime in which, experimentally, path instability occurs in pure water. This leads to a contradiction since without a standing eddy, vortex shedding will not occur. The experiments reported in this thesis will show that indeed another mechanism is observed for zigzagging bubbles.

For a better understanding of the dynamics of wakes, and especially the behaviour of bubble wakes, the studies of wakes behind solid spheres and drops by Achenbach (1974), Magarvey & Bishop (1961), Natarajan & Acrivos (1993) and Johnson & Patel (1999) are very informative. However, one should be cautious in applying these results to bubble dynamics as will be explained below.

The drag coefficient of solid spheres and drops is generally larger than for bubbles; this behaviour is related to the amount of vorticity produced. For larger bubbles, though, the deformation might become so large that the drag coefficient will be larger than the drag coefficient of a solid sphere of the same volume. Furthermore, it is observed that the drag coefficient of light solid spheres differs from that of heavy solid spheres (Karamanev *et al.* 1996). In this work light particles are observed to spiral in a manner similar to some bubbles.

The experimental results of Magarvey & Bishop (1961) for the wake behind drops come closest to what is observed for wakes behind bubbles. At low Reynolds numbers, the wakes of drops and bubbles are very similar, consisting of a single thread. For slightly larger Reynolds numbers, both feature a double threaded wake. At very large Reynolds numbers, an intermittent wake is observed for both the drop and the bubble. However, for the intermediate regime, in which path instability sets in for bubbles in pure liquids, the observations of the wake behind bubbles, drops, and solids are very different.

Natarajan & Acrivos (1993) reported on the stability of the axisymmetric flow around solid spheres and disks obtained in numerical simulations. They concluded that two different instabilities can occur at two distinct critical Reynolds numbers. The first critical Reynolds number, observed for spheres and disks, was associated with the instability of the near wake. The second critical value of the Reynolds number indicated a periodic instability or waviness of the far wake. They emphasised that for different objects the second instability might be reached at a lower Reynolds number than the first instability, and so the mechanism for the observed instability, might change.

7 Aim of thesis

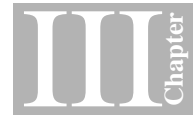
This summary of previous work is far from complete. Nevertheless, it is obvious that, even from this limited number of articles, many controversial results become evident (see tables 2.1 and 2.2). Especially, the type of motions observed after the first path instability has set in is remarkably different for all experiments. In this thesis the main focus is on clarifying this point.

It is most likely that many of the experimental results discussed have been obtained in contaminated liquids, especially when the wake is visualised. From these results vortex shedding was claimed to be the mechanism for a zigzagging path of the bubble, as is the case for solid spheres and drops. In this thesis a method is developed to visualise the wake of a bubble without affecting the purity of the water, and another mechanism for the zigzag motion is found.

The relation between the wake of a bubble and its motion needs to be studied. From this relation more information about the nature of the flow around the bubble can be deduced. This information can be applied in modelling the motion of bubbles in order for example to find the path of a single rising bubble, to study bouncing and pseudo-turbulence in bubbly flows.

On the basis of the experimental results of Duineveld (1994), it is expected that path instability sets in at a critical Weber number, while the shape of the bubble is still very close to a stable oblate ellipsoid. Both spiralling and zigzagging can commence immediately after the first instability sets in. The direction of the spiral can be clockwise or anti-clockwise. As soon as path instability sets in, the wake becomes non-axisymmetric. The path of the bubble is expected to be strongly related to the wake the bubble produces.

EXPERIMENTAL METHOD AND ANALYSIS TOOLS



In the experimental study of paths and wakes of bubbles in pure water numerous problems are encountered. Although most are trivial, it appears that in most experimental studies not all problems have been solved. Especially the visualisation of the wake of the bubble without endangering the purity of the water is a challenging problem, which has been solved in this chapter. A description of the experimental setup is given and the analysis method to determine the shape and path of the bubbles using a Fourier transform method of the outline of the projection is explained. The shape of the bubble is assumed to be ellipsoidal and the minor axis is approximately directed along the path.

1 Water tank and bubble generation

The experiments have been performed in a glass-walled water tank (15x15x50 cm, wall thickness 18 mm). Prior to the experiments the tank was intensively cleaned with soap, laboratory ethanol and rinsed with highly purified water. The latter was produced in a three-step purification system consisting of a decalcifier, Millipore RO 60 and a Millipore Q plus. This resulted in water with the highest possible electrical resistance (18.2 M Ω cm) and less than 10 ppb organic particles. Contamination of the water was avoided by the use of a closed system and by filling the tank from below. In this way air contact and so the absorption of gases, in particular CO₂, is minimised. In addition to all these precautions to ensure the purity of the water, prior to each experiment the rise velocity of some single bubbles at room temperature (20 \pm 1 °C) was determined to check the purity once more.

The bubbles were produced with a system similar to that described in Kok (1993) and Duineveld (1994). It consists of an injector (Valco N₄) and a switching valve (Valco N₆), syringe, pressurised clean air and a hyper clean water supply. A volume with pressurised air determines the size of the bubble. The bubble is pushed into a transparent silica tube (0.25 mm bore) with hyper-clean water. As a result pure water is in front of and behind the bubble and a second measurement of the bubble

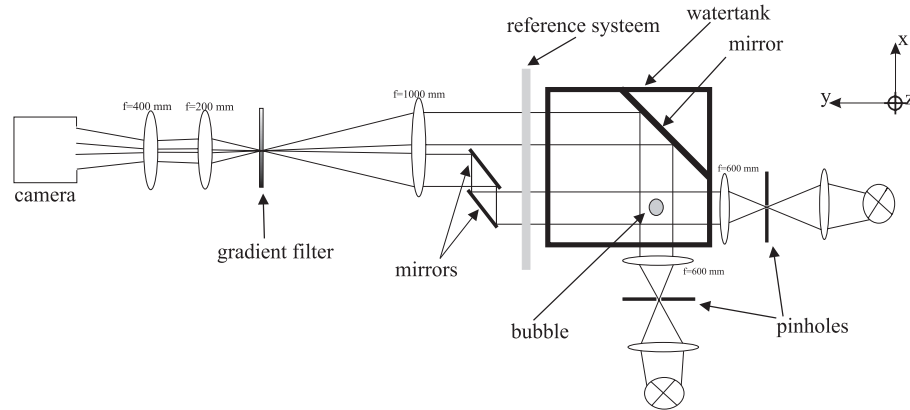


FIGURE 3.1: *The top-view of the experimental two-way schlieren setup. Both perpendicular views are recorded on a single NAC high speed video. The reference system is placed outside the water tank to avoid contamination of the water and interaction with the bubbles.*

volume can be made. Next the bubble was set on the top of the capillary and subsequently released from the needle by a sudden push of $0.1 \mu\text{l}$ of water. A third check of the volume was performed by the analysis program explained later in this chapter. The differences between the three determined equivalent radii resulted in an overall accuracy of 2%.

2 Visualisation method

Most experimental techniques in bubble dynamics use the differences in refractive index of water and air to visualise the bubble. In a back lighting technique the refraction of the light by bubbles is used, whereas in a side lighting technique the scattering of the light by bubbles is used. With these techniques bubble dynamics can be studied, but no information about the flow around the bubble can be obtained.

In previous studies dye or particles were added to the water to study the flow around bubbles. However, their use is undesirable as it contaminates the water and so changes the dynamics of the bubble, and the flow around it, significantly. With a view to this it remains questionable whether Particle Image Velocimetry (PIV) is applicable in studying the flow around bubbles in pure water. To overcome the problem of contamination and at the same time being able to visualise the flow around the bubble a schlieren technique is used.

Schlieren optics is a well known technique often used to visualise density gradients in compressible flows, e.g. shock waves. However, this technique is not visualising the density gradient, but the refractive index gradient. At constant ambient

pressure the refractive index of water is temperature dependent and temperature differences in water can be used to visualise water flows with schlieren. Fortunately the schlieren technique is very sensitive as the refractive index difference of water between 20°C and 30°C is less than 0.1%, which is required for the present application.

A technique similar to schlieren would be the shadowgraph technique. However, the schlieren technique visualises the temperature gradient while the shadowgraph visualises spatial gradient in the temperature profile. Although the shadowgraph system is much simpler as no gradient filter is needed, the main drawback is that there is no directional sensitivity. By the placement of the gradient filter two important features occur: schlieren visualises the horizontal temperature gradient and in the vertical direction the shadowgraph technique visualises the spatial gradients in the temperature profile.

In our application the water in the tank is heated from above by infrared light, which resulted in a constant stable temperature gradient (1.1°C/cm) in the region between 30 and 40 cm above the needle in the water. The colder water, dragged in the wake of the bubble, is visualised. In this way no contamination in the form of particles and/or dye is introduced. Apart from that, this visualisation method is able to capture the bubble's outline simultaneously as the refractive index of air and water is different. With help of a two-way schlieren setup the position, the wake and the orientation of an air bubble are determined simultaneously.

In Figure 3.1 a schematic overview of the two-way schlieren setup and the water tank is shown. The three mirrors make it possible to record two, mutually perpendicular, views on a single NAC high speed video recorder (500 frames/s). Reference points outside the water tank make it possible to determine the world-coordinates on each frame, which is necessary as the frames on the tape tend to be misaligned up to about 10 pixels. With the position of the reference points on each frame this misplacement can be compensated for.

The optical path lengths of both views of the bubble and the reference system were different, but a focal depth of more than 20 cm allows sharp recordings of bubble and reference system in both views. The different magnification factors of the reference system and of the bubble in each view is taken into account when analysing the images.

3 Temperature gradient effects

The effect of the temperature gradient on the terminal rise velocity can only be checked by a comparison to results in the absence of a temperature gradient. In the literature most experiments are performed at a temperature of about 20°C and so thus the present results of the bubble rise velocity in water of 20°C are compared with the results reported by Clift *et al.* (1978). Figure 3.2 is taken from Clift *et al.* (1978).

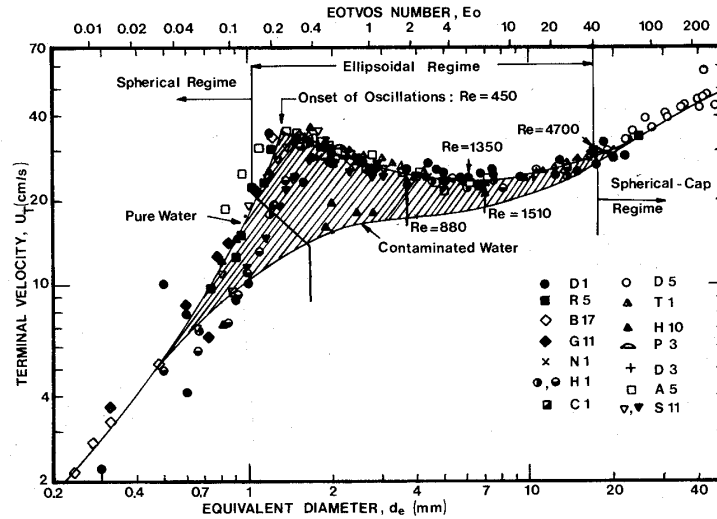


FIGURE 3.2: The rise velocity of a bubble vs diameter, taken from Clift et al. (1978) in water held at 20°C.

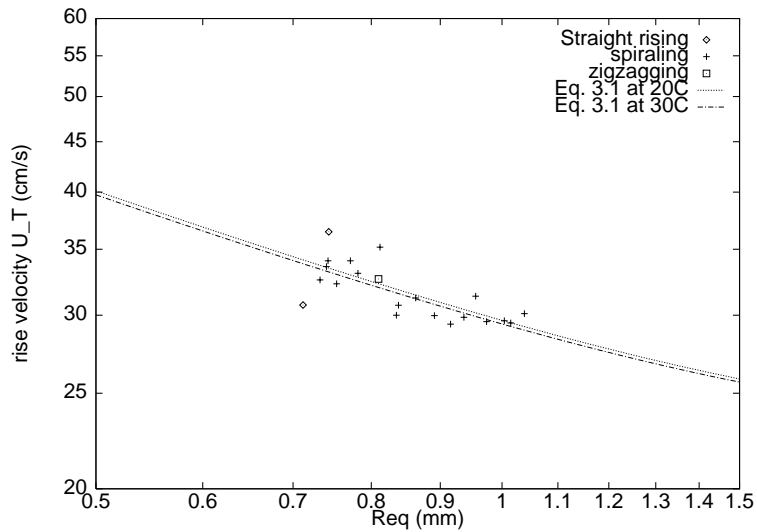


FIGURE 3.3: Experimental data for the rise velocity vs bubble radius in pure water held at 28°C. The 'lines' are empirically determined by Clift et al. (1978).

An empirical curve for bubbles in clean water (top line), determined from this data at 20°C, is

$$U_T = \sqrt{\frac{2.14\sigma}{2\rho r_{eq}} + 1.100gr_{eq}}, \quad \text{for } r_{eq} > 0.75 \text{ mm.} \quad (3.1)$$

Duineveld (1994), also using the present purification system, showed that in the present experiments the water can be considered clean based upon the terminal rise velocity of the bubbles. However, after heating the water the average temperature in the measuring volume becomes approximately 28°C, which does have an effect on the terminal rise velocity. Although Figure 3.2, taken from Clift *et al.* (1978), pretends to include only data in water held at 20°C, experimental data of Aybers & Tapucu (1969b, □) is included in water held at 28°C. The terminal velocity of Aybers & Tapucu is observed to be larger than that for clean water at 20°C, at least for small bubbles.

The main aim of this section is to test the effect of a temperature gradient on the rise velocity of the bubble. The temperature of the water in the centre of the measuring volume was approximately 28°C; with a constant temperature gradient of 1.1°C/cm. Experiments (Figure 3.4) clearly show an extra increase of the terminal rise velocity arising from this gradient. The viscosity is determined from the empirical relationship from Grigoriev & Meilikhov (1997)

$$\log\left(\frac{\eta_T}{\eta_{20}}\right) = \frac{1.3272(20 - T) - 0.001053(T - 20)^2}{T + 105}, \quad (3.2)$$

which indicates a difference of about 20% of the viscosity of water at 20°C and that at 28°C.

As a result the imposed temperature gradient, needed for the use of schlieren, has an undesired effect on the rise velocity of a bubble. The rise velocities, measured in the temperature gradient with a mean temperature of the surrounding liquid of 28°C, were above the rise velocities in water with a uniform temperature at 28°C (compare Figures 3.3 and 3.4). This can be explained by solving the equation of motion utilising a temperature-dependent viscosity in Levich's (1962) expression for the drag, i.e.

$$\frac{1}{2}m\frac{d^2z}{dt^2} + 12\pi\mu(T)r_{eq}\frac{dz}{dt} = gm \quad (3.3)$$

where z the height in the tank, g the acceleration of gravity and $m = 4\rho\pi r_{eq}^3/3$, twice the added mass of a bubble. The surface tension differs less than 1% between 28°C and 20°C and thus the Marangoni effect can be neglected. Equation (3.3) is solved numerically and the effect of the temperature dependent viscosity on the rise velocity of the bubble ($r_{eq} = 1.0$ mm) is shown in Figure 3.5. The initial conditions for the uniform temperature of 28°C are, $z = 0.30$ m, $dz/dt = 0.328$ m/s, $T = 28^\circ\text{C}$. For the gradient the initial conditions are $z = 0.30$ m, $dz/dt = 0.328$ m/s, $T =$

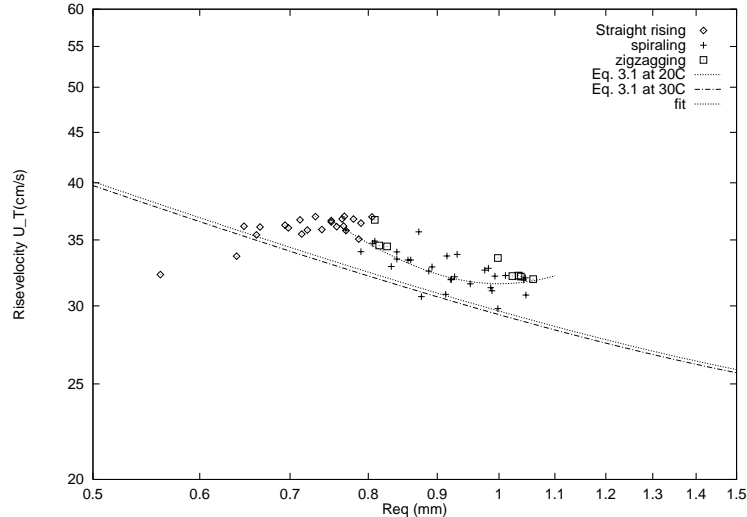


FIGURE 3.4: *The effect of a temperature gradient on the bubble rise velocity. The 'lines' are the same as in Figure 3.3 and the measurements are the rise velocities in a linear temperature field around 28°C. The velocity in the gradient is about 7% higher than without the gradient.*

20°C, $dT/dz = 1.1^\circ\text{C}/\text{cm}$. It shows a significant effect of the temperature gradient on the rise velocity of a bubble.

The horizontal solid line in Figure 3.5 shows the rise velocity of a bubble in water held at a uniform temperature of 28°C. The temperature is indicated with the horizontal dotted line. The rise velocity of a bubble in a temperature gradient of 1.1°C/cm is given by the dotted curve. The region of 28°C is reached at about 37.3 cm above the capillary. In this region the terminal rise velocity is already reached. The velocity in the gradient is increasing only slightly after reaching the point 32 cm above the release point, where the temperature is only about 22.2°C. As a result all measurements in the temperature gradient were performed for a bubble which already reached its 'final' velocity 5 cm lower, which is a good indication that the final state of bubble shape, path and wake was already obtained.

Although the rise velocity of a bubble has only a small dependence on the temperature, there is a large effect of a temperature gradient. The extra acceleration term for a bubble ($r_{eq} = 1.0\text{mm}$) moving in a temperature gradient resulted in a 6% higher rise velocity (Figure 3.4), which is in agreement with the 7% increase in velocity measured in experiments.

Another effect of the temperature gradient is the motion of the wake due to the

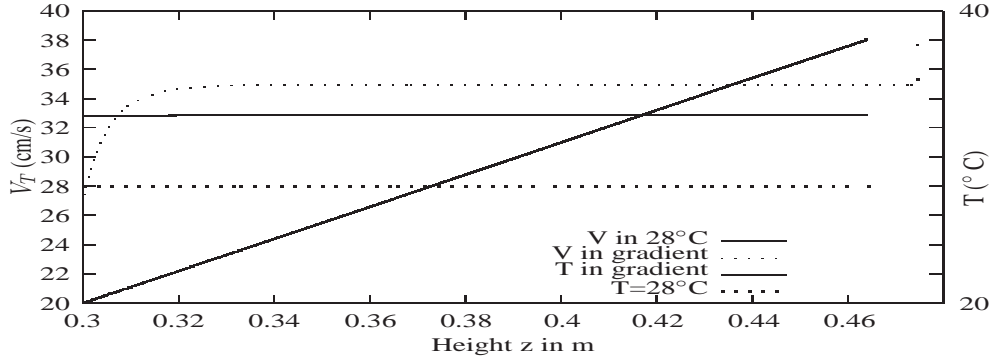


FIGURE 3.5: *The effect of a temperature gradient on the rise velocity of a bubble ($r_{eq} = 1.0$ mm), taking into account the Levich drag with temperature dependent viscosity of water. It can be seen that the bubble in a temperature gradient has a higher velocity at 28°C than in a uniform temperature of 28°C.*

density differences. This effect is negligible, provided that

$$\sqrt{\frac{\Delta\rho g r_{eq}}{\rho U_T^2}} \ll 1. \quad (3.4)$$

In our case this fraction is approximately 0.01 and thus the buoyancy effect on the wake due to the temperature gradient can be neglected with respect to the velocity of the rising bubble.

4 Image analysis

For the analysis of the images a Fourier transform method of the bubble outline was used as described in Lunde & Perkins (1995). The images were digitised and the mapping coefficients between world and pixel-coordinates were determined by the reference system. An intensity threshold, determined in each image, defined the bubble outline. Subsequently this outline was re-mapped to permit the use of Fast Fourier Transforms. Finally all parameters, such as position, shape (and so volume and equivalent radius) and velocity, together with the dimensionless numbers, were calculated assuming an ellipsoidal shape of the bubble with equivalent volume.

The experiments were recorded on an NAC high speed (500 frames/sec.) video recorder and then digitised using a Unix frame grabber. The digital videos collected in this way were checked on missing or double frames and errors due to conversion from NTSC to PAL, and subsequently the data was converted to Raw Pixel Gray Map (RPGM) format on which the analysis was performed.

A reference system outside the water tank is used to determine the world coordinates. It is essential that the reference system be recorded on each image as the position of the images on the tape tends to 'flutter' over several pixels on consecutive frames. The effects of this motion can be eliminated by determining the displacement of the reference points. The positions of the reference points are also used to adjust for the misalignment of both perpendicular views. The determination of the linear mapping coefficients between world and pixel coordinates can be described with

$$x_w = ax_p + by_p + c, \quad y_w = dx_p + ey_p + f. \quad (3.5)$$

The 6 coefficients ($a - f$) are determined by a least-squares method. For this a minimum 3 reference points in each view are needed, but we used up to 6 to be able to correct for translation, rotation and simple distortion of the image. Our reference points were little holes in accurate adjustable rulers. The position of each hole on the images was determined in a similar way as the centre of the bubble, which will be discussed later.

A problem with the determination of the world coordinates of the reference points and of the bubble is the difference in the optical magnification factor. This problem arises from the differences between the two object distances as the reference system is placed outside the water tank. The magnification factors can be determined by simple optics (Hecht, 1974). For each lens the following formula can be used:

$$\frac{1}{f} = \frac{1}{s_o} + \frac{1}{s_i} \quad (3.6)$$

$$M = -\frac{s_i}{s_o} \quad (3.7)$$

where s_o and s_i are the object and image distances, f the focal length of the lens and M the magnification factor. For the first lens the object distance is known and the image distance can be calculated. From this the object distance for the next lens can be calculated and so on. For all these lenses a magnification factor is determined and all together lead to the overall magnification factor. In these calculations the differences in optical path length of glass, water and air are taken into account.

A coordinate system X, Y, Z (see Figure 3.1) is defined, where Z is in the vertical direction. Four different magnification (reference points and bubble XZ-plane and YZ-plane) can be determined in this way. From these the images have been calibrated. The differences in magnification factor have been verified with measurements of solid spheres of known size. The difference in the magnification factor between reference system and bubble is 0.902 in the XZ-plane and 0.886 in the YZ-plane.

The image analysis is based on the method developed by Lunde & Perkins (1995), with some modest improvements and adjustments for the schlieren images. Numerical image analysis tools like edge detection filters, gradient filters or other

standard filters cannot distinguish between the wake and the bubble. A better method is to determine the intensity threshold of the bubble outline. An extra problem arises from the vertical intensity gradient in the images caused by the schlieren method. So successive images have different intensities near the bubble and need different thresholds for analysis. This problem has been solved by determining the threshold from a weighted average of the intensity in an area inside and an area around the bubble. The outline is then re-mapped so that the fast Fourier transformation can be used. The outline can be expressed as a complex function of its arc-length,

$$B(l) = x(l) + iy(l), 0 \leq l \leq L, \quad (3.8)$$

which is an L-periodic function. The Fourier representation of B is then

$$B(l) = x(l) + iy(l) = \sum_{n=-\infty}^{\infty} A_n e^{(-2\pi inl/L)}. \quad (3.9)$$

This will only work with an analytical expression, but not with a discrete representation of $B(l)$ and discrete Fourier transformation has to be used on the re-sampled discretised bubble outline for estimating the Fourier descriptors:

$$A_n = \frac{1}{K} \sum_{k=0}^K [x(k) + iy(k)] e^{(2\pi ink/K)}, \quad -\frac{K}{2} \leq n \leq \frac{K}{2}. \quad (3.10)$$

From the latter a continuous expression for the bubble outline can be determined

$$B(k) = x(k) + iy(k) = \sum_{n=-K/2}^{K/2} A_n e^{(-2\pi ink/K)}, \quad 0 \leq k \leq K, \quad (3.11)$$

where $x(k)$ and $y(k)$ are periodic functions

$$\begin{aligned} x(k) &= \sum_{n=-\infty}^{\infty} \left[a_n \cos\left(\frac{2\pi nk}{K}\right) + b_n \sin\left(\frac{2\pi nk}{K}\right) \right], \\ y(k) &= \sum_{n=-\infty}^{\infty} \left[b_n \cos\left(\frac{2\pi nk}{K}\right) - a_n \sin\left(\frac{2\pi nk}{K}\right) \right]. \end{aligned} \quad (3.12)$$

Under the assumption that the bubble is ellipsoidal, it can be shown that the centre of one projection outline gives two coordinates of the centre of the bubble. From the second projection the third one can be determined and the z-coordinate is double checked. The centre of the outline is the mean position of the outline and is consequently covered in the A_0 term of the Fourier descriptors. For example, in the XZ view: $x = \Re(A_0)$ and $y = \Im(A_0)$. From the $A_{\pm 1}$ a first approximation of the major

and minor axes and the direction can be determined. These quantities determine the primary ellipse of the bubble.

The orientation of the (primary) ellipse is given by the phase angles of $A_{\pm 1}$; the orientation of the major axis is $(\phi_1 + \phi_{-1})/2 \pm \pi$, where $\phi_n = \arctan(b_n/a_n)$. The minor axis is perpendicular to the major axis. The lengths of the major and minor axis of the primary ellipse are $2(|A_{-1}| + |A_1|)$ and $2(|A_{-1}| - |A_1|)$, respectively. For small bubbles these are equivalent with the exact major and minor axes. For larger bubbles the direction of the axis remain equivalent, but the length of the axis will change. These lengths are recalculated by determining the intersection of the axes, in the specified direction, with the outline of the projections.

Path analysis

From consecutive images the path of the bubble is determined. From the path the velocity could be derived by applying the technique of central differences. However, this would lead to large error bars on the velocity. A better estimate is found by curve fitting the path. In this way measuring errors are averaged, although systematic errors will remain. From the experiments it appeared that all the paths could be described with:

$$\begin{aligned} X(t) &= X_0 + C_x \cos(\omega_x t + \phi_x) \\ Y(t) &= Y_0 + C_y \cos(\omega_y t + \phi_y) \\ Z(t) &= Z_0 + C_z \cos(\omega_z t + \phi_z) + U_T t, \end{aligned} \quad (3.13)$$

where X_0 , Y_0 and Z_0 are constants, the frequencies are denoted by ω_x , ω_y and ω_z , and the phase shifts by ϕ_x , ϕ_y and ϕ_z . The amplitudes are C_x , C_y and C_z . From fitting these curves with the experimental data, the path and velocity of the bubble was accurately determined. Furthermore, this makes analysis of the observed paths easy. For example, the resulting top view (X,Y) can be classified as an ellipse. Assuming that $\omega_x = \omega_y = \omega$, which is a valid assumption as the observed top-views are ellipses, the top-view of (3.13) can be rewritten in the form of a quadratic equation:

$$\begin{aligned} X(t) - X_0 &= C_x \cos(\omega t + \phi_x) = C_x \cos(\omega t) \cos(\phi_x) - C_x \sin(\omega t) \sin(\phi_x) \\ Y(t) - Y_0 &= C_y \cos(\omega t + \phi_y) = C_y \cos(\omega t) \cos(\phi_y) - C_y \sin(\omega t) \sin(\phi_y), \end{aligned} \quad (3.14)$$

These equations can be rewritten in quadratic form by solving for $\cos(\omega t)$ and $\sin(\omega t)$ to find

$$\frac{1}{C_x^2 Q^2} \tilde{X}^2 - \frac{2 C_x C_y \cos(\phi_y - \phi_x)}{C_x^2 Q^2 C_y^2} \tilde{X} \tilde{Y} + \frac{1}{C_y^2 Q^2} \tilde{Y}^2 = 1, \quad (3.15)$$

with $Q = -\sin(\phi_y - \phi_x)$ and $\tilde{X} = X(t) - X_0$ and $\tilde{Y} = Y(t) - Y_0$. Although mathematically speaking it is possible that Q becomes zero ($\phi_y - \phi_x = n\pi$), physically this would mean that the motion is a zigzag and thus the top-view no longer a ellipse but a straight line. Equation 3.15 is a general quadratic curve of the form $ax^2 + 2bxy + cy^2 = 1$. Under rotation of the coordinate system

$$\begin{bmatrix} x' \\ y' \end{bmatrix} = \begin{bmatrix} \cos \theta & \sin \theta \\ -\sin \theta & \cos \theta \end{bmatrix} \begin{bmatrix} x \\ y \end{bmatrix}, \quad (3.16)$$

over such an angle (in anti-clockwise direction) that the axis of the ellipse coincide with the coordinate axis, the curve is rewritten in a simple form for analysis

$$t_1 x'^2 + t_2 y'^2 = 1 \quad (3.17)$$

This describes an ellipse with the lengths of the semi-axes are $1/\sqrt{t_1}$ and $1/\sqrt{t_2}$, so t_1 and t_2 must both be positive. The aspect ratio of the ellipse is

$$\zeta = \sqrt{\frac{t_1}{t_2}}. \quad (3.18)$$

Bubble shape

The shape of small bubbles is spherical. For slightly larger bubbles it can be shown that the shape is an ellipsoid. A further increase in size results in a loss of the fore-aft symmetry of the bubble as shown by Duineveld (1994). For the analysis an ellipsoidal shape is assumed. For the bubbles of the size used in the experiments this assumption is valid.

One of the properties of an ellipsoid is that the projections are ellipses. Furthermore, it can be shown that with three orthogonal projections the ellipsoid is uniquely defined. The shape of an ellipsoidal bubble cannot be determined immediately from only two projections. However, as the short axis is almost perfectly directed along the path, the orientation of an ellipsoidal bubble can be determined from the path. With two perpendicular views and the orientation, the ellipsoid is uniquely defined.

The general description of an ellipsoid is a quadratic equation

$$ax^2 + by^2 + cz^2 + 2dxy + 2exz + 2fyz = 1, \quad \text{or} \quad (3.19)$$

$$1 = (x \ y \ z) \begin{pmatrix} a & d & e \\ d & b & f \\ e & f & c \end{pmatrix} \begin{pmatrix} x \\ y \\ z \end{pmatrix} = \mathbf{r}^T \mathbf{M} \mathbf{r} \quad (3.20)$$

If the three eigenvalues of \mathbf{M} exist and are all positive the quadratic equation describes an ellipsoid. The axes are along the eigenvectors and the length is the square

root of the eigenvalue. Under these conditions, the projection onto a plane, in this example the XZ-plane, can then be found from solving

$$F(x, y, z) = \mathbf{r}^T \mathbf{M} \mathbf{r} - 1 \quad (3.21)$$

$$\frac{dF(x,y,z)}{dy} = 2by + 2dx + 2fz = 0. \quad (3.22)$$

Although there exist two solutions to equation 3.21, the outline, projected in the XZ-plane, is again a unique quadratic equation

$$\frac{a(-ax^2b + d^2 + 2dfz + f^2z^2 - cz^2b - 2exzb + b)}{e^2b - abc + af^2} = 0, \quad (3.23)$$

which can be shown to be an ellipse and the minor and major axis can be derived in a similar way as explained for the top view of the path. The solution $a = 0$ is not valid as in that case equation 3.19 no longer describes an ellipsoid.

The objective is not the axes in the projection, but the axes of the ellipsoid itself. From the two projections eight variables can be determined and from the assumption that the minor axis of the ellipsoid is, approximately, in the direction of motion, another variable can be determined. As a result the 9 parameters (three centre coordinates, the lengths of three axes and the direction of three axes; the six parameters a - f , and the three coordinates of the centre) necessary to uniquely describe an ellipsoid are determined. However, this inverse problem is based on the fitted shape of the projections. The errors made in these projections would lead to errors in the determined ellipsoid. An iteration procedure is necessary to determine the shape of the ellipsoid for which the error in the outline of the projections is minimised.

The projection of the ellipsoid in the YZ-plane can be determined in a similar way as shown above. Minimising the differences in contours of these projections and the contours of the projections obtained experimentally will give the best approximation of the ellipsoidal bubble. Fortunately, the shape in consecutive time steps is almost equal so that a small number of iterations is required.

FREE RISING BUBBLES IN QUIESCENT WATER



The path of a rising bubble in hyper-clean water is correlated with the wake behind the bubble. A double-threaded wake occurs for bubbles moving in a non-rectilinear path. The non-rectilinear path, both spiralling and zigzagging, is in our view maintained by a lift force and not by vortex shedding, as is observed for solid spheres and for bubbles in contaminated water. The strength of this lift force is indirectly determined. For the zigzag, the lift force changes sign in the mean position of the zigzag.

1 Introduction

Above a certain volume, bubbles rising in clean water perform unsteady irregular motions. For solid spheres a similar behaviour is observed, although at lower Reynolds numbers ($Re \approx 200$) than for bubbles ($Re \approx 600$). The main differences between bubbles and solid spheres are the conditions at the boundary: no-slip and rigid for solids, zero-tangential-stress and deformable for bubbles. These differences influence the vorticity production at the surface and the drag. Contamination of the water may result in solid-sphere like behaviour of the bubble.

Moore (1963, 1965) analysed the effects of shape and boundary layer on the rise velocity of bubbles in a liquid of low viscosity. Many researchers have studied the path of free rising bubbles experimentally, but Maxworthy *et al.* (1996) showed that none of these were performed in perfectly clean fluids. Consequently, in our opinion, the contamination of the fluids in most experiments is the reason for the differences in the parameters indicating the transition between the occurrence of straight-rising, spiralling and zigzagging path of bubbles.

The aim of this study is to simultaneously visualise, in a three dimensional way, the path and wake of a free rising air bubble in hyper clean water. Although the wake and the path of a rising air bubble are related, this relationship has hardly ever been studied. The main reason is that most visualising or measuring techniques contaminate the fluid. In recent work of Lunde & Perkins (1997) a salted dye solution

was used. Their conclusion was that vortex shedding is the mechanism for a bubble performing a zigzagging path in clean water. It is shown here that this conclusion is questionable.

In this chapter the experimental results for the three observed paths are presented: i) straight rising, ii) zigzagging and iii) spiralling. Based upon the experimental results a wake model is developed that explains the path of the bubble. In this model a lift force is employed. The magnitude of this lift force is indirectly determined in several ways.

2 Results and Discussion

Experiments for bubbles with equivalent radii of 0.4-1.1 mm showed a clear transition from a rectilinear path to a zigzag or spiral path. This transition occurred for bubbles with equivalent radii of 0.81 mm or Reynolds number $Re=740$. After the transition both zigzagging and spiralling bubbles were observed (cf. Saffman 1956). In the present study it was observed that the majority of the zigzagging bubbles were found to be of the size of 0.81-0.88 mm and 1.00-1.10 mm.

The angular motion of the spiral has no preferred direction; clockwise or anti-clockwise and the top view of the path is an ellipse and not necessarily a circle. A zigzag motion appears to be a special case of a spiral; one axis of the top view has zero length. Although a spiral and a zigzag path are fundamentally the same, both are separately mentioned to explain the differences in the development of the wake.

For a rectilinear path the wake consists of a single-threaded wake. After a path instability sets in, a double-threaded wake is observed (Figure 4.2 and 4.8). The initial disturbance of the wake determines the rate of growth of the instabilities in the wake (§ 3).

2.1 Straight rising bubble

It is well known that a small bubble rises along a rectilinear path. In our experiments this occurs for equivalent radii less than about 0.81 mm, $We_{cr} < 2.7$ and $Re < 740$, which is in agreement with the results of e.g. Tsuge & Hibino (1977) and Benjamin (1987), taking into account the temperature effects (Morton dependence of critical Weber and Reynolds number, equation 2.13 and 2.14). The schlieren visualisation of a straight rising bubble is presented in Figure 4.1. It shows the single-threaded wake behind the bubble in pure water; on the left the XZ view and on the right the YZ view as defined in Figure 3.1.

In Figure 4.1 the two perpendicular projections of the bubble and its wake are visible. It is obvious that this bubble is straight rising as in both views the path is straight. The black areas on the side of both projections belong to the reference system. The reference points are the lighter spots. The vertical distance between

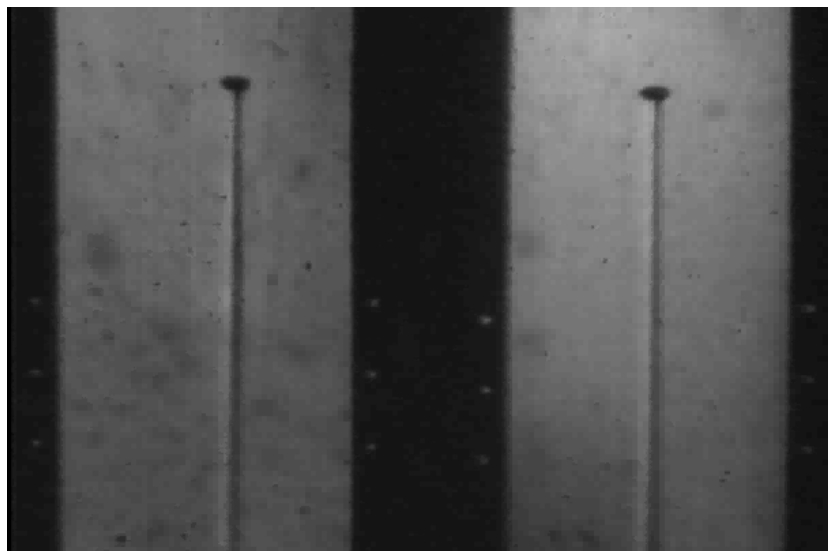


FIGURE 4.1: *The single-threaded wake behind a rectilinear rising bubble ($r_{eq} = 0.79$ mm). On the left the XZ view and on the right the YZ view. The black areas are part of the reference system outside the water tank. The walls of the tank and the mirror inside the tank are over 20 bubble radii away from the bubble.*

these points is 0.5 cm. It can be seen in Figure 4.1 that the reference points between the two perpendicular views are displaced vertically, which indicates that both views are not perfectly aligned. This misalignment is compensated for in the analysis. The reference system is placed outside the water tank and therefore will not influence the motion of the bubble. The walls of the water tank and the mirror placed inside the tank are over 50 bubble radii away from the bubble. As a consequence the motion is not influenced by wall effects.

Although it is not (clearly) visible in the images, there exists a vertical temperature gradient in the water column. The bubble drags some colder water in its wake. For reference purposes, denote the direction from left to right in both projections as positive. In a horizontal plane the temperature changes with position in both projections: i.e., from left to right, in the plane outside the wake warm, inside the wake colder and outside the wake again warmer. A negative temperature gradient in horizontal direction, or in other words a positive gradient in refractive index, is visualised with a positive gradient in the intensity (a lighter area). A positive gradient in the temperature results in a darker area. As a consequence the single-threaded wake is visible as a lighter and a darker streak. The relation between grey scale and temperature gradient is connected to the orientation of the schlieren gradient filter. The schlieren images clearly show the stable single-threaded wake.

In the vertical direction hardly any change in brightness is observed. This clearly indicates that the present schlieren setup is only visualising the horizontal temperature gradient. It has to be noted, however, that in the vertical direction the measurement technique only detects the curvature of the temperature profile. This implies that the imposed temperature gradient is indeed constant.

Furthermore, it can be observed that the shape of the bubble is not spherical. In fact it is nearly ellipsoidal, with the short axis aligned along the direction of motion. In all experimental work for bubbles of the sizes studied in this thesis, this alignment of the bubble, within measuring accuracy, is observed. So also for spiralling and zigzagging bubbles. This fact is used to determine the orientation of the bubble from the information on the path.

The configuration of the wake behind drops was extensively studied by Magarvey & Bishop (1961) and for small drops they also observed a single-threaded wake. The transition towards a double-threaded wake occurs already at $Re = 210$, which is comparable to the critical Reynolds number for solid spheres. However, for both drops and solid falling spheres no path instability has been observed. This is probably caused by the difference in the moments of inertia (Ryskin & Leal 1984). The rotation of the wake of a solid light sphere (Achenbach 1974) eventually induces the sphere to follow a spiralling path and to reduce the terminal rise velocity (Karamanev *et al.* 1996).

Similarly for bubbles the local maximum of the terminal rise velocity (Figure 3.4) determines the transition between the rectilinear and the oscillatory motions. In the present case this transition occurs for: $U_T = 36.5$ cm/s; $r_{eq} = 0.81$ mm; or equivalently $Re = 740$ or $We = 2.7$, where the fluid properties of water at $T = 28^\circ\text{C}$ are taken ($\rho = 996$ kg/m³, $\nu = 0.8 \times 10^{-6}$ m²/s and $\sigma = 0.071$ N/m). The large difference in the critical Reynolds number for drops/solid spheres on one hand and bubbles on the other hand is a strong indication that different mechanisms might determine the onset of path instability.

2.2 Zigzagging bubble

As a path instability sets in, a bubble can either zigzag or spiral. For both cases a double-threaded wake is observed. It is illustrative to analyse the zigzagging bubble as a separate case. As the motion is in one plane a two dimensional flow analysis is possible. The results this analysis will also explain the apparent differences between the wake of a spiralling bubble and the wake of a zigzagging bubble.

In Figure 4.2 the two perpendicular views of a zigzagging bubble ($r_{eq} = 1.00$ mm) can be seen. The motion of the bubble is in a single plane (two dimensional); by coincidence this plane coincides with one of the projection planes in this experiment. The sequence of images of the zigzag motion can be seen in Figures 4.4 and 4.5. Clearly the path in the right view looks like a straight line and that in the left view sinusoidal. Unfortunately, during a large part of the recording the bubble was behind

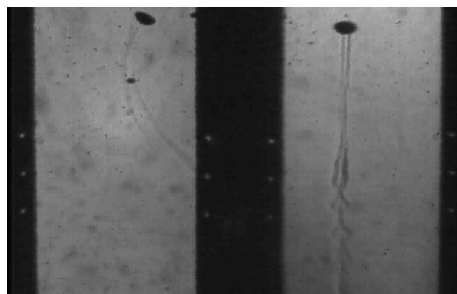


FIGURE 4.2: *The double-threaded wake behind a zigzagging bubble ($r_{eq} = 1.00$ mm). By coincidence the plane of the zigzag coincides with one of the views.*



FIGURE 4.3: *An enlargement and enhancement of the wake behind the zigzagging bubble in Figure 4.2. Especially the twist and the interaction of the filaments further downstream can be observed.*

the reference system. However, this was the only recording in which the plane of motion coincided with one of the projection planes, clearly showing the zigzagging motion in a plane.

The shape of the bubble appears to change significantly in the right view (compare $t = 12$ with $t = 56$ ms). This is not necessarily a shape oscillation as from the other view it is clear that the bubble can be moving towards or away from the observer, which for a flattened ellipsoid results in a change of the projection. In the left image the shape of the bubble is also changing (compare $t = 52$ with $t = 68$ ms). This cannot be a result of the projection. It is concluded that there is a shape oscillation for zigzagging bubbles. In the experiments this shape oscillation appeared to have the same frequency as that of the path. It is conjectured that the shape is related to the orientation and the nature, single- or double-thread, of the wake.

Especially the wake shows very interesting phenomena. Just behind the bubble a double-threaded wake is visible in the YZ view of Figure 4.2 (enlarged in Figure 4.3). The left view of Figure 4.2 only shows a single thread, caused by the projection; one thread blocks the view of the other thread. This is the general picture behind a zigzagging bubble: a double-threaded wake. However, when the bubble passes its 'mean' position ($t=28$ ms in Figure 4.4), or in other words, when the curvature of the path becomes zero, in both views only a single thread is observed. It is observed that the double-threaded wake only exists when the curvature of the path is nonzero. This is in agreement with the single-threaded wake observed for straight rising bubbles.

The patterns observed in the wake, several bubble diameters behind the bubble, are a result of the instability of the double-threaded wake. This is not vortex shedding, as was assumed by other researchers, e.g. Lunde & Perkins (1997) and Brücker (1999). For the bubbles in the present regime of interest, vortex shedding is not observed. In § 4 it is shown that the instability of the double threaded wake (two

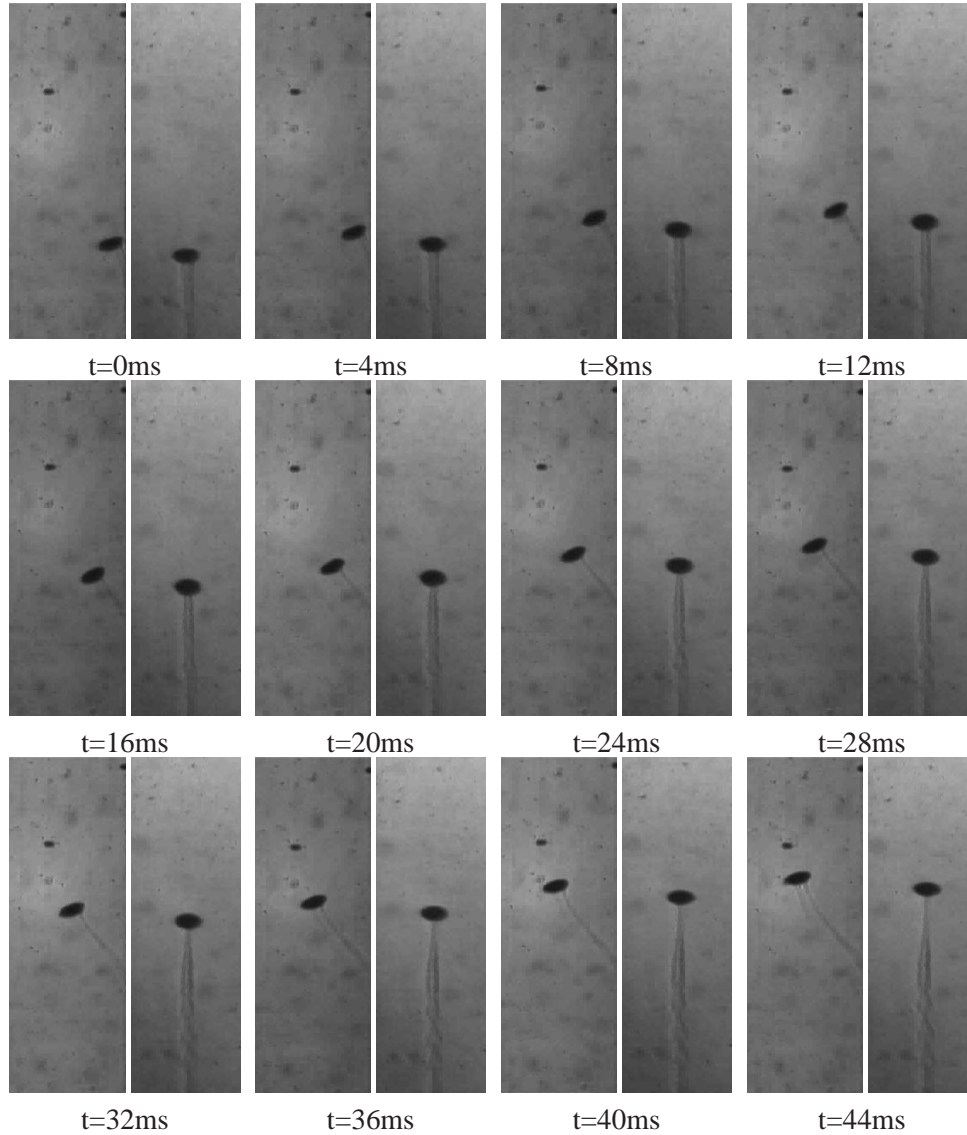


FIGURE 4.4: Successive schlieren images of a bubble ($r_{eq} = 1.00$ mm) in zigzagging motion. Each pair of images contains the XZ and YZ view, respectively. Note that in the YZ-view the path is straight while it is sinusoidal in the XZ-plane. Furthermore, the wake of the bubble is a double-threaded wake, unless the curvature of the path is zero (starts at $t \approx 24$ ms) in the mean position of the zigzag. The wake reconnects and in the following the occurrence of an instability is observed in the wake. It is clear that the zigzag is NOT maintained by vortex shedding at the maximum of the sinus in the XZ-plane ($t \approx 64$ ms).

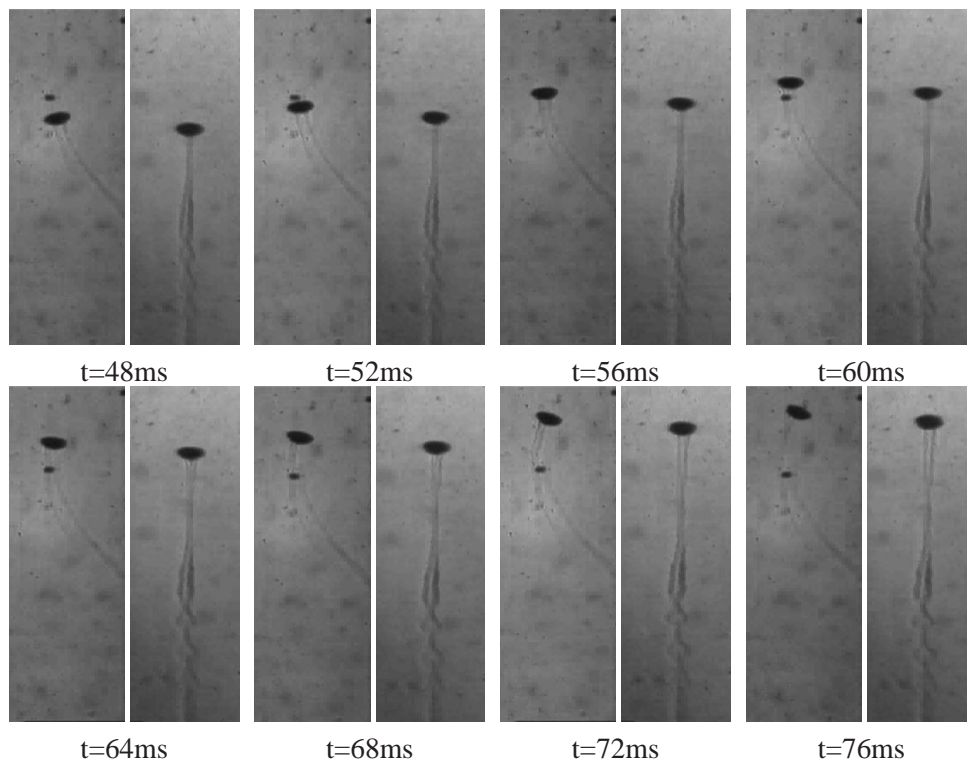


FIGURE 4.5: Continuation of schlieren images of a zigzagging bubble

counter rotating vortex filaments) is in fact the Crow instability (Crow 1970). In general this instability corresponds with the instability of the trailing vortices behind airplanes.

Modelling the zigzag motion

In this section the zigzag motion is analysed by applying momentum conservation principles. Furthermore, an explanation for the appearance and disappearance of the double-threaded wake is given.

Denote a reference system moving with the bubble. As long as the bubble rises rectilinearly, the fluid far from the bubble has a velocity $\mathbf{U}_f = -U_T \mathbf{k}$ in vertical direction. A straight rising bubble carries bound vorticity with only an azimuthal component, which is confined to the boundary layer of the bubble and the wake. The horizontal component of the momentum is zero.

Suppose that the bubble, without changing shape or orientation, has a horizontal velocity as well. Because of the no-tangential-stress condition at the bubble's surface, there is now a meridional vorticity component ω_θ . Since vorticity is conserved, the vorticity lines leaving the bubble, now have a vertical vorticity as well. This vertical

component of the vorticity will form a double-threaded wake. As a bubble is unable to change its shape or orientation instantaneously, for these bubble sizes a double threaded wake will occur for all curved paths.

If for some reason (e.g. instability in wake, surface instability) the bubble starts to move to the right, there has to be an opposite rate of change of fluid impulse in the wake of the bubble. Let the added mass of the bubble be a tensor \mathbf{M} , which for an ellipsoidal bubble only has diagonal components. The component M_{11} then is associated with the added mass in the direction of the minor axis and M_{22} along both major axes. The velocity of the bubble is $U_T \mathbf{k} + \mathbf{U}_b$, where \mathbf{U}_b is the horizontal velocity component.

For a control volume of fluid enclosing both the bubble and the wake, the resultant force is the external force, in the present case this is the buoyancy force. The buoyancy force acts only in the vertical direction. Therefore the rate of change of the fluid impulse due to the horizontal deflection, $d(M_{22} \mathbf{U}_b)/dt$, must be equal and opposite to the rate of change of momentum of the wake in horizontal direction.

The change of the momentum of the wake is accomplished by the formation of the double threaded wake, or in other words the trailing vortex filaments (Figure 4.6). The normal to the plane through the filaments close to the bubble is aligned along $\mathbf{ds} \times \mathbf{l}$. In a cross section of the wake the $\mathbf{ds} \times \mathbf{l}$ -component of the momentum I of infinitely long, straight, counter rotating vortex filaments of strength Γ is, see for example Saffman (1992), p. 102,

$$I = \rho \Gamma l \quad (4.1)$$

Per unit time the length of the wake grows with $U_T \mathbf{k} + \mathbf{U}_b$ m. The change of momentum per unit time in the wake is $\rho \Gamma (U_T \mathbf{k} + \mathbf{U}_b) \times \mathbf{l}$. The change of fluid momentum (I_f) per unit time is, adding the added mass term and the wake term,

$$\frac{d\mathbf{I}_f}{dt} = \frac{d(\mathbf{M} \cdot (U_T \mathbf{k} + \mathbf{U}_b))}{dt} + \rho \Gamma (U_T \mathbf{k} + \mathbf{U}_b) \times \mathbf{l} \quad (4.2)$$

The change of the horizontal fluid momentum component should be balanced by a change of the horizontal bubble momentum component of opposite sign. The change of bubble momentum per unit time, or in other words the force on the bubble, thus becomes

$$\frac{d\mathbf{I}}{dt} = - \frac{d(\mathbf{M} \cdot (U_T \mathbf{k} + \mathbf{U}_b))}{dt} - \rho \Gamma (U_T \mathbf{k} + \mathbf{U}_b) \times \mathbf{l} \quad (4.3)$$

Furthermore, the drag force \mathbf{D} and the buoyancy force $\mathbf{B} = -\rho \mathbf{g}V$ act on the bubble. The force balance on the bubble becomes

$$- \frac{d(\mathbf{M} \cdot (U_T \mathbf{k} + \mathbf{U}_b))}{dt} - \rho \Gamma (U_T \mathbf{k} + \mathbf{U}_b) \times \mathbf{l} - \rho \mathbf{g}V + \mathbf{D} = 0. \quad (4.4)$$

From (4.4) it follows that the bubble acquires a velocity in the horizontal plane and the velocity vector inclines towards this plane. In other words, from momentum conservation an opposite rate of change of momentum on the bubble to that of the wake, will force the bubble in a curved path.

At this point it is worthwhile to review the inviscid spiralling of bubbles as described by Benjamin (1987). In the spiralling motion, in which both linear and angular impulse are conserved, it is essential that there is a small angle (η in Benjamin's paper) between the velocity vector of the bubble and the minor axis of the ellipsoid, which is a good approximation of the instantaneous shape of the bubble.

In work on bubbles it is reported by various authors (e.g. Ellingsen 1998, Duineveld 1994 and Lunde & Perkins 1997) that the shape of the bubble can be described as an ellipsoid, however with the velocity vector directed along the minor axis. It is quite possible that the small angle η is within the experimental measuring accuracy.

On the basis of this analysis, it is plausible that either this misalignment exists or a non axisymmetric shape is present. This point is certainly a good subject for future research. In inviscid spiralling the bubble spins about the major axis. Whether such spinning motion is present experimentally, can not be concluded on the basis of the present experiments, although the orientation is definitely changing. On the basis of the present experiments no conclusive argument can be given for either, although there is a strong indication that the shape is no longer axisymmetric for zigzagging bubbles (Figures 4.4- 4.7).

The second term on the left hand side of (4.4) is a lift force on the bubble related to the wake. As long as $\mathbf{U}_b = 0$, there is no Γ either. Just before the onset of path instability, the acceleration of the bubble is negligible and buoyancy and drag balance each other. Since $\mathbf{g} = -g\mathbf{k}$ the drag then is $\mathbf{D} = -\rho gV$. At the first instant after path instability has set in, (4.4) becomes

$$\frac{d(M_{22}\mathbf{U}_b)}{dt} = -\rho\Gamma U_T \mathbf{k} \times \mathbf{l}, \quad (4.5)$$

Which implies an acceleration of the bubble in the horizontal direction, as soon as a double threaded wake is formed. Subsequent production of vorticity on the bubble's surface will maintain the strength of the vortex filaments and so the magnitude of the lift force. When U_b increases, and the force includes the contribution of this lateral motion, the lift force remains normal to the trajectory of the bubble. The bubble's trajectory is bent more and more. However, when the path is no longer along \mathbf{k} , buoyancy will decrease the effect of the lift force and the curvature of the path decreases. This is clearly visible in the figures of Figure 4.4, where the curvature of the path is decreasing towards the horizontal mean position. Ultimately, at $t \approx 28$ ms, the effect of the lift force on the deflection will be balanced with the component of buoyancy perpendicular to the path and the motion becomes rectilinear again. However, this rectilinear motion is not aligned with \mathbf{k} .

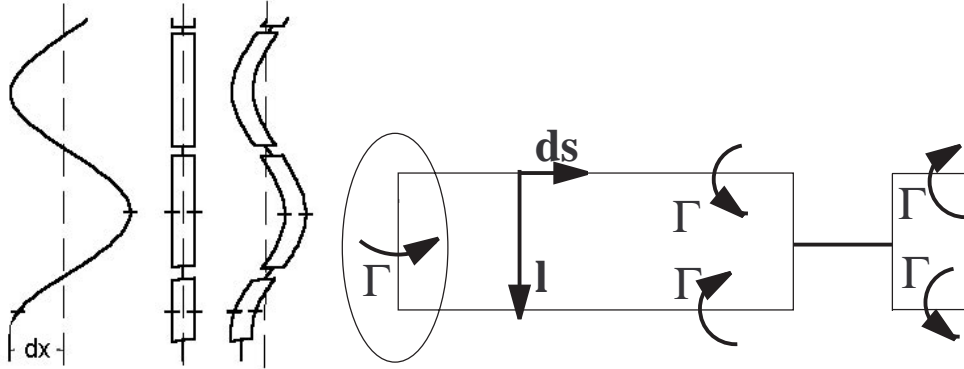


FIGURE 4.6: The left three images are the XZ, YZ and 3D view of path and related wake. The lowest part is the straight rising part, approximately 4 cm exactly above the capillary. Note the intermittent wake behind the zigzagging bubble. The most right image is the model of the bubble and wake as a lifting line with trailing vortices.

As a result the vorticity production on the bubble's surface becomes purely azimuthal again and a single-threaded wake is formed; the two counter-rotating vortex filaments have reconnected. Now the lift force becomes negligible. Buoyancy will deflect the bubble towards k . This deflection causes that the vorticity on the bubble is no longer azimuthal with the new direction of motion and a double-threaded wake is formed. The whole process starts again, now with an opposite sign of the lift force (Figure 4.7). Clearly this leads to a zigzagging motion.

It is easy to show that the whole argument is similar when not an initial horizontal displacement, but the formation of the double-threaded wake is assumed as the first onset of the instability. The nature of the instability is arbitrary as long as it can be associated with a change in the horizontal component of the momentum of the bubble and an opposite sign in that of the fluid.

The general picture of the bubble wake and the nature of the lift force is sketched in Figure 4.6. Vortex lines are closed and hence there is a circulation around the bubble. In this sketch this is modelled as a line vortex crossing the bubble generating the described circulation. This makes a comparison to a lifting line theory possible.

It has to be stated, that the motion that arises from this model has obtained a mean horizontal displacement dx of the bubble, Figure 4.6. In other words, the mean horizontal position of the zigzagging bubbles is not straight above the capillary. This needs to be verified experimentally. In the present setup the position of the capillary relative to the reference system could not be determined accurately as the measurements were performed approximately 30 cm above the capillary. If this horizontal displacement is the case, however, it can explain the lack of reproducibility of the experiments as the direction of this displacement is arbitrary. Often, as shown in the

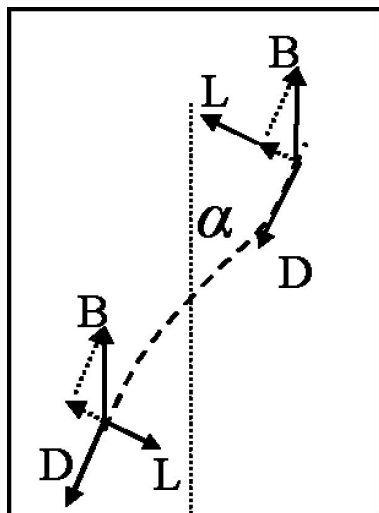


FIGURE 4.7: *The direction of the forces, the added mass force not included, on a zigzagging bubble near the equilibrium position. The wake-induced lift force L is perpendicular to the path and of constant strength as long as the curvature is non-zero. Buoyancy, B , is always directed upwards and the Drag, D , is always along the path. When buoyancy balances the lift force the curvature becomes zero. For a zero curvature the lift force is zero. Buoyancy deflects the path and the lift force changes sign.*

experimental results presented in Figure 4.2, parts of the path are behind the reference system, although a previous, similar-sized, bubble stayed in between of the two sides of the reference system. This is a strong indication that indeed the mean horizontal displacement is present.

In fact, we expect that any experimental setup studying bubble dynamics in this regime and giving reproducible measurements has to be a poor experiment in the sense that a preferred direction of the initial displacement is posed. A very probable cause for these imperfections is the bubble production and release (Chapter 5). In the present experiments care was taken to manufacture accurate capillaries. Using a microscope the capillary edge was checked for imperfections due to cutting and polishing.

In summary the zigzagging path is maintained by a lift force directed perpendicular to the path of the bubble and is related to the double-threaded wake. This wake is fed by the vorticity production on the bubble's surface as soon as the curvature of the path is non-zero. A good approximation is a constant strength of the wake and thus the lift force, except for the equilibrium region. In this region a single-threaded wake is observed. In the model this point on the path is assumed to be a singular point at which the lift force changes sign abruptly.

This wake-induced lift force should not be confused with the shear-induced lift force observed for bubbles. As in the present experiments the liquid is quiescent there is no shear-induced lift force.

2.3 Spiralling bubble

The path of a spiralling bubble is hardly ever a perfect spiral. Observed from above the perfect spiral path would be a circle. Otherwise ellipses are observed (Figure 4.12.

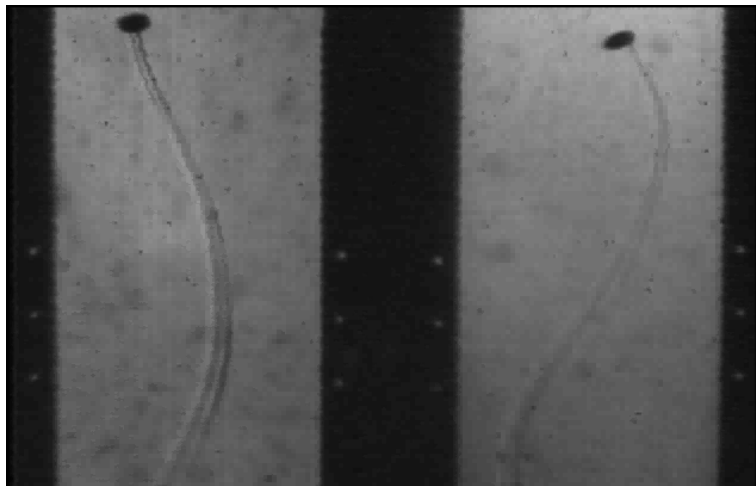


FIGURE 4.8: *The two perpendicular views, XZ and YZ, of a double-threaded wake behind a nearly perfectly spiralling bubble ($r_{eq} = 1.01$ mm).*

For every spiralling bubble a double-threaded wake was observed (Figure 4.8). When spiralling bubbles are small or close to perfectly spiralling this is a stable wake. For large bubbles and ellipsoidal top views of large aspect ratio (tendency towards zigzag), this wake is unstable close to the bubble. Although even for the perfectly spiralling bubble the wake becomes unstable a long time after the bubble has left the frame of view, we will call this wake stable.

For a stable bubble wake in both views it might appear that the filaments are twisting but this is a result of the projection. Care has to be taken in identifying spiralling or zigzagging from just one side view. Two views are needed, because often in one view a motion might look like a spiral, but appears to be a perfect zigzag.

From the separate views (Figure 4.9) a mode-2 axisymmetric shape oscillation appears to be present. However, after the bubble shape and orientation is recalculated with the analysis program, no shape oscillations of the bubble is found. For zigzagging bubbles (§ 2.2) a mode-2 oscillation has been observed and has been related to the orientation and the nature of the wake. Contrary to zigzagging bubbles, the wake consists of a double-threaded wake at all times. For a spiralling bubble the orientation of the filaments is not changing relative to the orientation of the bubble. The bubble has a fixed shape, but the orientation changes in such a way that the minor axis is directed along the path.

The apparent mode-2 oscillation appears to be caused by the projection of the outline of the bubble in a single view. Lunde & Perkins (1995) did mention this mode-2 shape oscillation, however they observed this in each view separately and did not analyse the shape and orientation in detail. Probably, they were misled by the

projection of the bubble. Ellingsen (1998) noted this projection effect and concluded that no mode-2 shape oscillation was present for spiralling bubbles. Even for a solid ellipsoid in a spiralling path, with the minor axis directed along the path, the periodic change in angle of view will show this apparent mode-2 oscillation in a single view. Obviously, there is no shape oscillation for a solid ellipsoid.

In Figures 4.9- 4.11 it can be seen that the wake is positioned asymmetrically behind the bubble. At $t = 72$ ms the wake in the XZ view is positioned on the right side of the bubble. As a consequence the shape of the bubble is no longer perfectly ellipsoidal, but we believe that this has limited influence on the observed motion. Furthermore it might appear that the views, XZ and YZ, were not taken at the same time as the height of the bubble appears to differ in both views. In fact this is a misalignment of both projections. From the recordings of the reference system (see also Figure 4.8) this misalignment is compensated for in the analysis.

The most plausible explanation of the horizontal motion is the force on the bubble resulting from the wake, as was hypothesised for the zigzagging motion. From the successive images it is observed that the wake consists of two counter rotating vortex filaments. Similar to the zigzagging motion, see §2.2, this is related to a lift force on the bubble. This wake-induced lift force is directed towards the central position of the spiral perpendicular to the path. Thus maintaining the spiralling motion.

However, the question of the onset of the spiralling motion from the rectilinear path is still unanswered. One possible explanation is that an impulsive wrench in vertical direction occur as a first instability. Such an impulsive wrench is hard to imagine for the most likely instabilities. However, according to Benjamin's (1987) theory an impulsive wrench has to be present for a spiralling motion.

Another way to explain the spiralling motion is that a second instability of the zigzagging path occurs. After the first instability a zigzagging motion occurs and then an instability on the zigzagging path takes place. A type of instability that might occur is a rotation of the plane through the filaments relative to the bubble, or a similar instability as observed for the transition from rectilinear to zigzag path. If the initial displacement is not in the same plane as the zigzag, a helical motion is most likely to take place. This can be deduced from similar arguments used to explain the zigzag motion. Furthermore the direction a second instability can explain the appearance of both clockwise and anti-clockwise helical motions, depending on the direction of rotation of the plane through the filaments of the threads relative to the bubble, or the direction of the second displacement.

For this it is necessary that the orientation of the wake changes gradually. This reorientating wake can be associated with the appearance of an impulsive wrench, which is in agreement with the Hamiltonian theory for a spiralling bubble by Benjamin (1987). The wake-induced lift force remains perpendicular to the path and gradually a perfectly spiralling motion is formed. In the intermediate regime

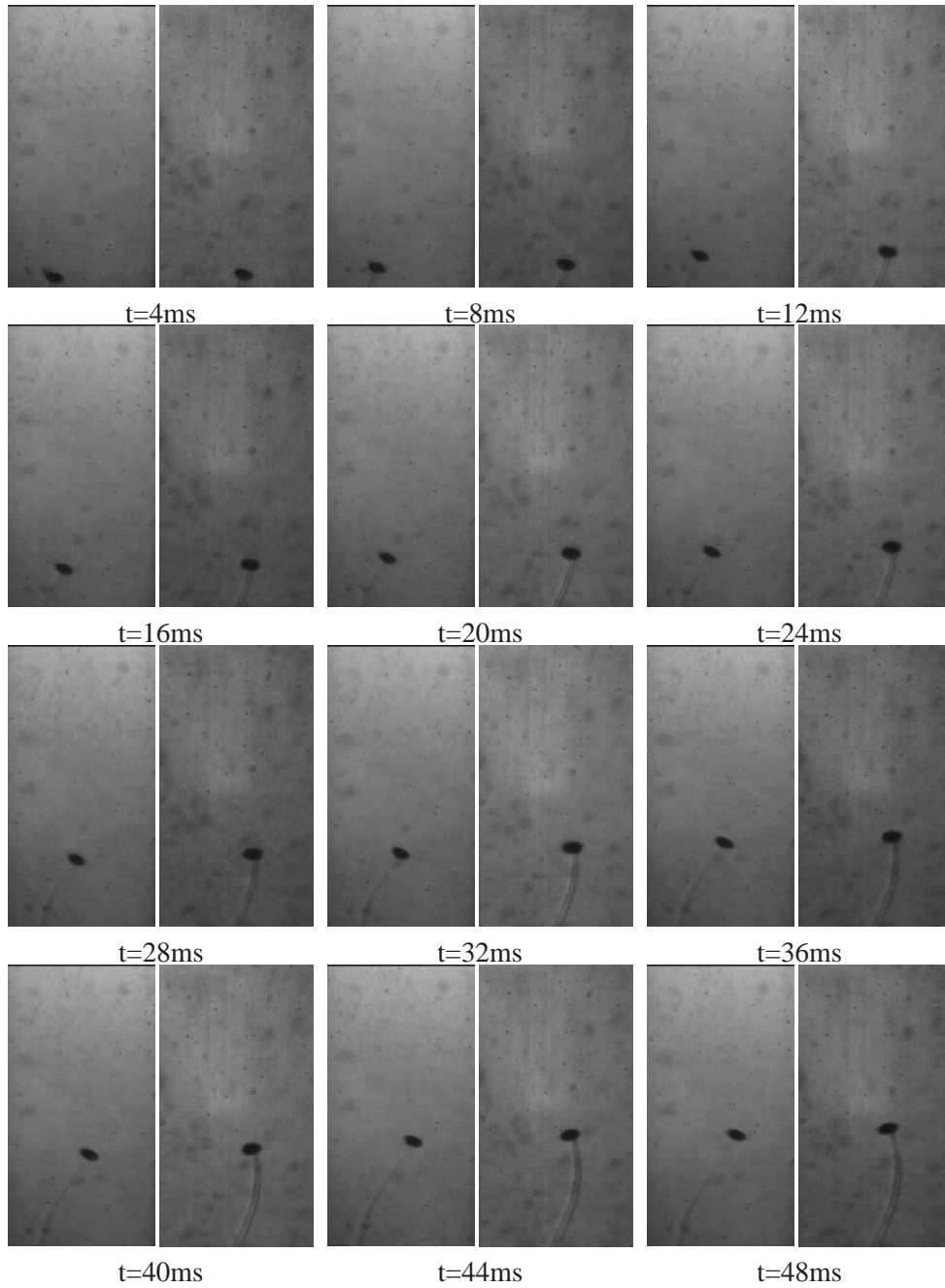


FIGURE 4.9: *Successive images, XZ and YZ views, of a bubble ($r = 1.01$ mm) in spiralling motion. The wake consist of a double-threaded wake, which becomes unstable far behind the bubble (not visible).*

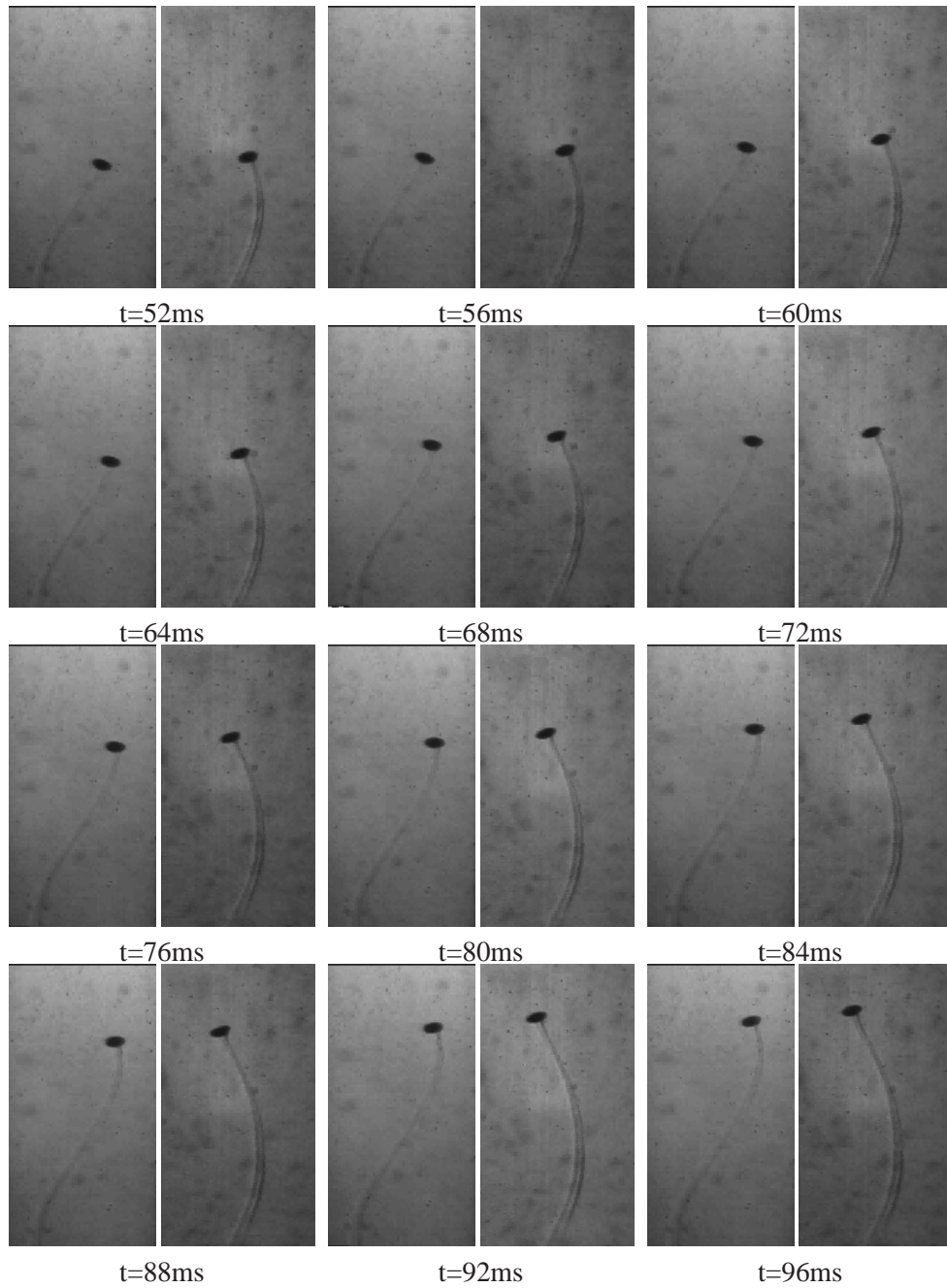


FIGURE 4.10: Successive images of spiralling motion $r_{eq} = 1.01$ mm (continued).

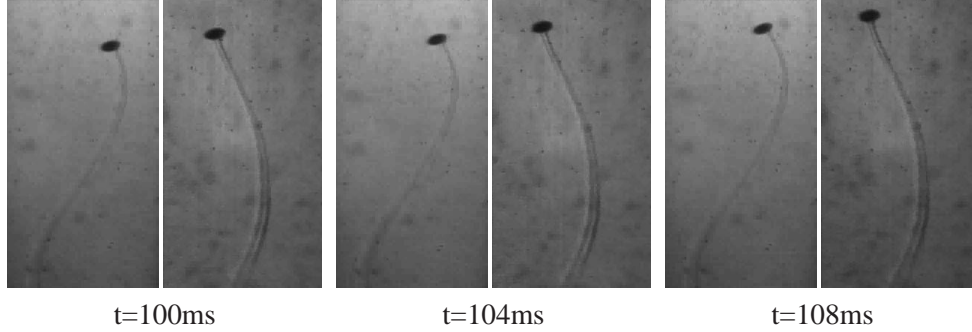


FIGURE 4.11: Successive images of spiralling bubbles $r_{eq} = 1.01$ mm (continued)

non-perfectly spiralling motions will exist, which explains the often observed non-perfectly spiralling motions (top view ellipses, Figure 4.12).

The appearance of a second instability indicates that the height above the release point is essential. Close to the release point mainly zigzagging and very flattened helical motions will be expected. High above the release mainly perfectly spiralling motions are expected. Also the previously mentioned perfectly zigzagging bubbles are expected to follow a perfectly spiralling path high above the capillary. Experiments by Ellingsen (1998) do show these trends.

The typical horizontal ($u = \dot{x}$, $v = \dot{y}$) and vertical ($w = \dot{z}$) velocity components for an almost perfectly spiralling bubble can be seen in Figure 4.13. The velocity components are calculated from the path description found from the best fit to the experimental data,

$$\begin{aligned} x(t) &= 3.39 + 0.42 \sin(33.0t - 1.07), \\ y(t) &= 3.86 + 0.32 \sin(32.5t + 0.62), \\ z(t) &= -0.32 + 0.02 \sin(54.2t + 1.44) + 31.3t, \end{aligned} \quad (4.6)$$

where x , y and z are the Cartesian coordinates and all distances are in cm. From this it can be concluded that the velocity magnitude, $U_{tot} = \sqrt{u^2 + v^2 + w^2}$, and the vertical velocity are not exactly constant. It appears that this results from the small deviation from a perfectly spiralling motion; the amplitudes of the horizontal displacements are not equal. In this case the mean terminal rise velocity was $U_T = 31.3$ cm/s. It is expected that both the vertical velocity component and the velocity magnitude become constant as soon as the bubble was in a perfectly spiralling motion; top view of path is a circle.

The path of all spiralling and zigzagging bubble can be described by:

$$\begin{aligned} x(t) &= X_0 + A \sin(\omega_x t + \phi_x) \\ y(t) &= Y_0 + B \sin(\omega_y t + \phi_y) \\ z(t) &= Z_0 + C \sin(\omega_z t + \phi_z) + U_T t, \end{aligned} \quad (4.7)$$

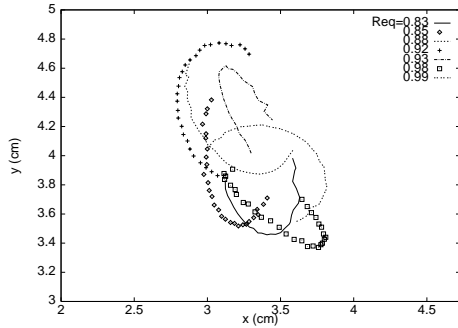


FIGURE 4.12: Top views of several spiralling bubble path. The top view is not necessarily a circle, but in general it is an ellipse. Also the direction of the axes of the ellipse is arbitrary.

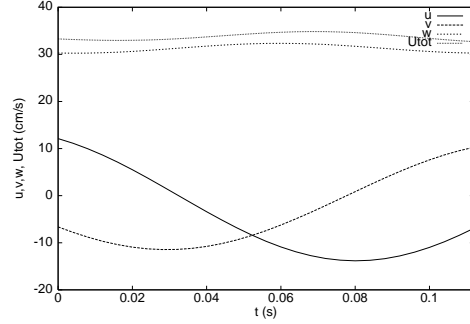


FIGURE 4.13: The velocity components of the spiralling bubble, $r_{eq} = 1.01$ mm; horizontal components u and v , the vertical component w and the velocity magnitude U_{tot} . Note that U_{tot} and w are not constant.

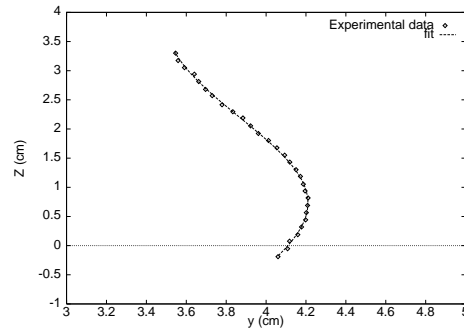
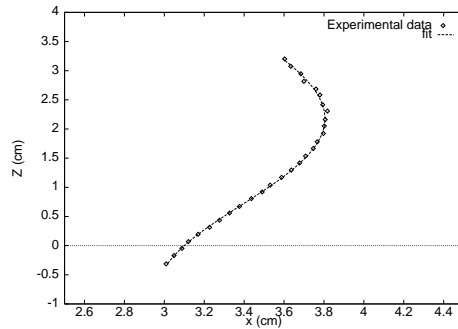


FIGURE 4.14: XZ and YZ views of experimentally observed path and the fitted path (equations 4.5) for the spiralling bubble of Figures 4.8-4.10.

where U_T is the mean terminal rise velocity. As was already seen in (4.6) in general $A \neq B$ and $C \ll A, B$. ϕ_x and ϕ_y are the phase angles; $|\phi_x - \phi_y| = \pi/2$ for a perfectly spiralling path. The frequencies, ω_x and ω_y , are not necessarily equal, resulting in rotating ellipsoidal top views. Unfortunately, no detailed information of this rotation could be gathered as the length of the observation view were limited. However this rotation has been observed by Ellingsen (1998). That $A \neq B$ results in non perfectly spiralling motion. This can also be concluded from the fact that there is an oscillation on the vertical velocity, $C \neq 0$.

Note that the path of spiralling bubbles observed in the present experiments cannot be described by the predictions of the Hamiltonian theory of Benjamin (1987)

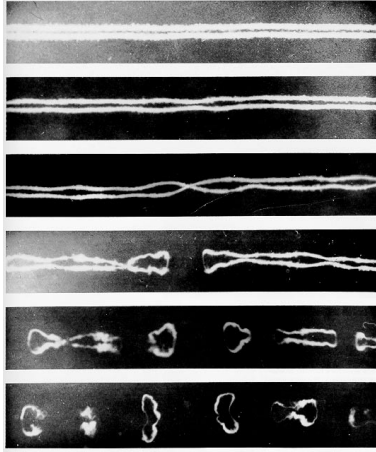


FIGURE 4.15: *The Crow instability of the trailing vortices in the wake of a B-74 at cruising speed and altitude. (Taken from Smith & Beesmer, 1959)*

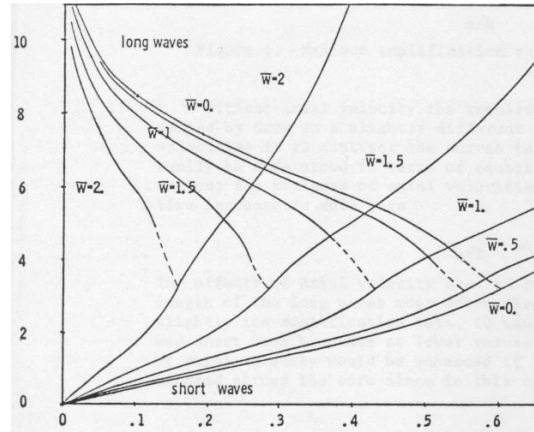


FIGURE 4.16: *The most unstable wavelength versus vortex core size. On the horizontal the core size over the initial core distance is plotted. \bar{w} is the ratio of axial and swirl velocity. Taken from Widnall *et al.* (1971).*

(Equation 2.11). According to these equations the radius of the spiral will be smaller than can $\sqrt{3}/10 \approx 0.17$ times the equivalent radius of the bubble. In the present experiments a typical factor of the radius is 4 times the equivalent bubble radius is obtained.

For the zigzagging bubble we described a model based on the equation of motion 4.4. This equation is also valid for spiralling bubbles and the lift force can be associated with the path described by the bubble. This will be eluded on in §4.

3 Wake

Close to the bubble the spiralling and zigzagging wake (Figures 4.8 and 4.2) are in general similar, although they show great differences in their subsequent behaviour. The wake of zigzagging bubbles is unstable on a short time-scale, whereas the instability of the wake of a spiralling bubble sets approximately 2s later. The instability in the wake can be explained by the tendency of the counter-rotating vortex filaments to become unstable. In case the structure of the bubble wake is comparable with the wake of an airplane, the wake of the bubble is susceptible to the Crow instability. In Crow (1970) pictures of the pair of counter rotating trailing vortices of an airplane in cruise (Figure 4.15) are shown. In these pictures the instabilities are clearly observable.

Extensive research (e.g. Widnall *et al.* 1971) showed that an initial small pertur-

bation is the onset of this instability. For a zigzagging bubble the initial perturbation, the reconnection of the vortex filaments, is larger than for a spiralling bubble with a regular wake. Therefore the instability develops much quicker and is already visible close to the bubble. For the spiralling bubble this instability occurs about 2s after the the vortex pair was generated on the bubble. This is equivalent to about 300 bubble diameters behind the bubble. Similarly for airplanes this instability would set in several hundreds of wing-spans behind the airplane.

The present observations of the zigzagging wake do not agree with the observations of other researchers, e.g. Lunde & Perkins (1997) and Brücker (1999). These authors observed vortex shedding and they related this to the mechanism for maintaining the zigzag motion. This vortex shedding would occur at the maximum amplitude of the zigzag, whereas we observed a stable double-threaded wake at this point. In the present experiments the reconnection of the wake for zigzagging bubbles takes place at the point where the bubble passes through the equilibrium position. Certainly both mechanism are very different. The vortex shedding is probably related to the dyes and/or particles added to the water. These contaminations were necessary for the visualisation techniques employed by Lunde & Perkins (1997) and Brücker (1999).

Extensive research by Ellingsen & Risso (1998) shows interesting phenomena far (40 bubble radii) behind a zigzagging bubble ($r_{eq} = 1.25$ mm). For a horizontal distance of 8 bubble radii from the point at which the bubble passes through the measuring volume the vertical liquid velocity component peaks at about 5.0 cm/s (15% of U_T). We believe that this velocity peak is associated with the vortical regions formed by the Crow instability of the trailing vortex filaments. For these vortical regions we determined a mean displacement velocity of about 10-20% of U_T .

Admittedly, a striking difference between the instability of the wake behind an aircraft and a bubble is the observed wavelength. For an airplane Crow concluded that the wavelength is 8.6 times the initial distance of the vortex cores, b . In the wake of a (zigzagging) bubble this wavelength is approximately $5b$ (Figure 4.3). This difference can be explained by adding an axial velocity component in the vortex filaments. This was studied by Widnall *et al.* (1971) and the wavelength depends on the ratio of the maximum axial and the maximum swirl velocity components, \overline{W} (Figure 4.16).

The observed wavelength for the instability, $5b$, is much shorter than the wavelength of the zigzag, which is approximately $60b$. As a result the instabilities seen in the wake of a zigzagging bubble can not explain the periodic motion of the bubble. Furthermore, the frequency found in the wake is not coupled with any frequencies of shape oscillations of the bubble, but is in fact the wavelength of the Crow instability with axial velocity.

4 Strength of the wake

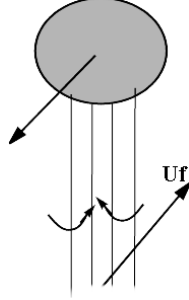


FIGURE 4.17: *The wake configuration of two counter-rotating filaments. The self-induced horizontal velocity is U_f and distance between the threads is l*

From the wake visualisations only the streaks can be made visible. The strength of the vortex filaments forming the wake can not be determined directly. In the following possible methods are given to indirectly determine the strength of the wake. One method is based on the self-induced motion of the wake. Another method is related to the force balance on a bubble. Further methods are related with the measured path.

In the experiments of zigzagging or spiralling bubbles the horizontal motion of the wake is determined. Since the wake of nearly perfectly spiralling bubble path is more stable, it gives the best reliable results. As the wake consists of two counter-rotating vortex filaments, the self-induced motion is related to the strength of vortices in the wake (Figure 4.17). The self-induced velocity, U_f of the filaments, and the distance l between them, can be determined. The self-induced velocity is determined in a single projection near the maximum amplitude of the path. The circulation Γ of a vortex filament can now be estimated from

$$\Gamma = 2\pi U_f l. \quad (4.8)$$

As already describe in the derivation of (4.5) it follows that the horizontal component of the lift force is estimated by

$$L = \rho \Gamma U_T = 2\pi \rho U_f l^2 U_T. \quad (4.9)$$

For a typical experiment the following values were found:

$$\begin{aligned} U_f &\approx 3.0 \text{ cm/s}, \\ l = b &\approx 0.6 r_{eq} \approx 0.6 \text{ mm}, \\ U_T &\approx 31.6 \text{ cm/s}, \\ r_{eq} &= 1.0 \text{ mm}. \end{aligned} \quad (4.10)$$

This results in a horizontal component of the lift force $L_{xy} = 2.1 \cdot 10^{-5}$ N. Note that the bubble path and thus the wake are at an angle to the horizontal. The total lift force can be determined from this pitch angle α with the horizontal of the spiral. For the spiralling bubble described in § 2.3 this angle is 29° . The total wake-induced lift force then becomes $L = 2.5 \cdot 10^{-5}$ N.

A second method of estimating the lift force on the bubble can be obtained from the balance of the buoyancy force component perpendicular to the path and the lift force as soon as the curvature of a zigzagging bubble becomes zero (Figure 4.4 $t = 28$ ms) as explained in the proposed model (§ 2.2). It appears that the angle which the path makes with the vertical is about 36° . Taking $\rho = 1000$ kg/m³, $g = 9.81$ m/s² and $V = \frac{4}{3}\pi r_{eq}^3$, the buoyancy force component balancing the lift force is $F_{g_n} = |\rho g V \sin(36)| = 2.4 \cdot 10^{-5}$ N. This is in remarkable agreement with the lift force determined directly from the wake.

Since the velocity magnitude of a spiralling and zigzagging bubble of the same size are about equal and the shape is similar, it can be deduced that the amount of vorticity produced by the bubble is about equal. And thus the lift force should have a comparable value. The lift force needed to maintain the spiralling motion is determined, for example for a 1.0 mm bubble as described in § 2.3. Now equation (4.4) needs to be solved for the determined spiralling path. The pitch angle of the spiralling motion can be determined from the experiments, $\alpha_p = 29^\circ$. From this a vertical component of the lift force can be determined, $L_z = F_g \sin \alpha_p = 2.0 \cdot 10^{-5}$ N. The total wake-induced lift force is $L = F_g \tan \alpha_p = 2.3 \cdot 10^{-5}$ N.

The horizontal component of the bubble velocity is $U_h = 0.17$ m/s. The spiral radius $R = 3.7$ mm and the added mass M or M_{22} is $2.2 \cdot 10^{-6}$ kg, when a spherical shape is assumed. Now the centripetal force F_c on the bubble can be calculated which should be balanced by the horizontal component of the lift force.

$$L_{xy} = F_c = MU_h^2/R = 1.7 \cdot 10^{-5} \text{ N} \quad (4.11)$$

and thus $L = L_{xy}/\cos(29^\circ) = 2.0 \cdot 10^{-5}$ N. This is slightly lower than the values determined in other ways as described above. The reason for this is that the added mass is underestimated by the assumption of a spherical shape instead of an ellipsoidal shape.

5 Conclusions

A path and wake visualisation method has been developed that does not affect the purity of the water. It was found that the wake of spiralling and zigzagging bubbles consists of two counter-rotating vortex filaments. Both motions are in many aspects similar and can occur for roughly the same experimental conditions.

The differences seen in the configuration of the wake far behind the bubbles can be explained by an instability of the system of the two counter-rotating vortex filaments. As the initial disturbance of the wake for a zigzagging bubble is larger than for a perfectly spiralling bubble, this instability is observed closer to the bubble. The wavelength of this instability is much smaller than the wavelength of the bubble's motion. Consequently, this instability cannot be the explanation for the zigzag motion of a bubble in pure water.

As soon as the curvature of the path becomes non zero the wake consists of a double-thread vortex system. This double-thread is shown to be associated with a lift force on the bubble. The perfect two dimensional motion for a zigzag can be explained by taking the lift force into account. The lift force is always directed perpendicular to the path.

The wake of zigzagging bubbles consists of a double-threaded wake as long as the curvature is non zero. When the curvature becomes zero the vortex filaments reconnect and successively a double-threaded wake of consisting of two counter-rotating vortex filaments of opposite sign is formed.

A lift force can be associated with the double-threaded wake. The strength of this lift force can be obtained from the self-induced motion of the wake, the force needed to maintain the spiralling motion, or from a balance between buoyancy and lift force as soon as the curvature of the path becomes zero for a zigzagging bubble.

Since all experiments reported by other authors concluded that vortex shedding (similar to the case of solid spheres) is the mechanism for the zigzag motion, the purity of the water used in their experiments is questionable. Yet, in many cases the water was still considered clean, based on measurements of the rise velocity of the bubble. Consequently a better indicator for the purity of the water should be used. A temperature gradient has an effect on the rise velocity of the bubble, nonetheless it does not affect the purity of the water.

Furthermore, shape oscillations have not been observed for spiralling bubbles. The mode-2 shape oscillation claimed by other researchers, is in fact, a result of the limited information on the bubble's shape when considering only a single projection. A more detailed analysis employing two projections shows no shape oscillations. For zigzagging bubbles a shape oscillation is observed and is related with the disappearance and reappearance of the double-threaded wake.

The way a bubble is produced can be very important for its subsequent behaviour. Especially bubble shape oscillations at the moment of release of bubbles should be avoided. Furthermore, small deviations of the exact shape can have a tremendous effect on the flow around the bubble.

1 Introduction

For the study of path stability it is desirable to eliminate as many sources of disturbances as possible. Possible source of disturbances are volume and shape oscillations triggered at the production and release of the bubble. These can be eliminated. The bubble production apparatus used in the present experiments is developed for accurate, reproducible bubble sizes in a large range of sizes, and it has the advantage that initial bubble shape oscillations are not observed. In our experiments the needles (capillaries) are small and well polished, which has a positive effect on the smoothness of the release.

Duineveld (1995) showed that for bubbles larger than $r_{eq} = 0.6$ mm, the bubble no longer has fore-aft symmetry. In spite of this the bubble is assumed to be ellipsoidal in many parts of this thesis. These assumptions have to be discussed.

The shape and the orientation of the bubble can have significant effects on the flow around the bubble. Numerically it will be shown that a small deviation of the bubble's ellipsoidal shape delays the formation of a standing eddy. Furthermore these numerical simulations indicate that at the onset of path instability in experiments, a standing eddy does not exist behind a bubble.

2 Bubble release

For the study of path instability of a free rising bubble, external factors influencing the stability should be eliminated. One very important factor is the bubble formation and its release. This should be as smooth as possible. Ideally the aim is to release

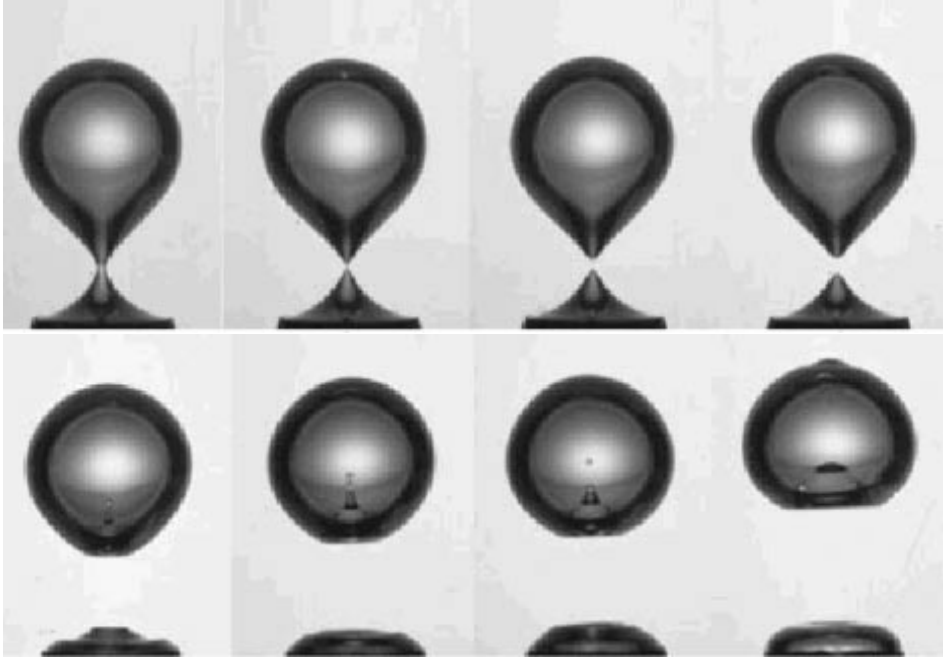


FIGURE 5.1: *Neck-breaking process of a bubble produced in a conventional way. Taken from Manasseh et al. (1998). Subsequently large shape oscillations are observed for the accelerating bubble.*

a single exactly spherical bubble, without any shape oscillations, in totally quiescent pure water.

Unfortunately, the most widely used method for bubble formation is a continuous airflow through a needle, which does not fulfil this criterion. The main drawback of this method is the neck-breaking process when the bubble detaches (see figure 5.1). The formation of the neck is associated with the surface tension between water and air (Longuet-Higgins *et al.* 1991). Just after neck-breaking the rear of the bubble features a cusp. After detachment this tip of the bubble is rapidly retracted and forms a jet inside the bubble. Occasionally even a water droplet is formed inside the bubble (Manasseh *et al.* 1998). Obviously undesirable large shape oscillations will appear.

A typical damping time scale, τ_s for shape oscillations, applied to the case of spherical bubbles, can be obtained from art. 355 in Lamb (1932),

$$\tau_s = \frac{1}{(n+2)(2n+1)} \frac{r_{eq}^2}{\nu}, \quad (5.1)$$

with n the mode number of the oscillation. The least damped mode is the $n = 2$

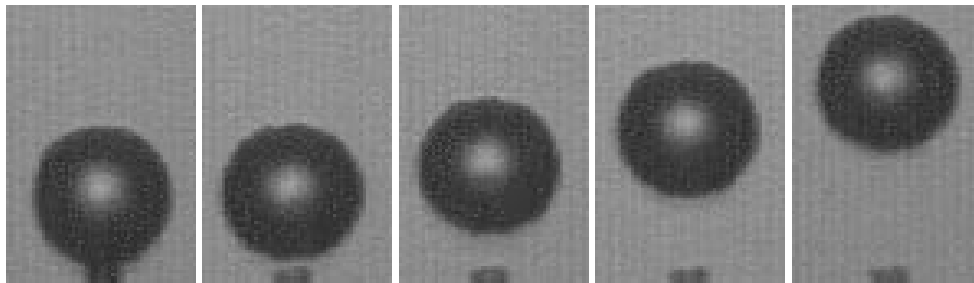


FIGURE 5.2: *Spherical release of bubbles produced in the experiments. Subsequently the bubble accelerates and adapts its shape smoothly.*

mode, leading to

$$\tau_s = \frac{r_{eq}^2}{20\nu}. \quad (5.2)$$

The typical time scale for a spherical bubble to reach the point at which path instability sets in is comparable to the relaxation time of the bubble. It is approximately

$$\tau_p = \frac{r_{eq}^2}{18\nu}. \quad (5.3)$$

Both time scales are of the same order. Therefore shape deformations and oscillation caused by the formation and release of bubbles are not completely damped at the point of the onset of path instability. These shape deformations might affect the instability. Hence the formation and release of bubbles should be as smooth as possible.

Another problem encountered in the ‘old fashioned’ bubble formation process is the continuous production of bubbles. This will result in an influence of the wake of the preceding bubble on the following bubble. As it is generally observed that bubbles will follow the path of a preceding bubble, clearly the observed path instability is influenced. This certainly will lead to reproducible measurements of consecutively produced bubbles. But it is doubted that path instability, especially the initial deflection direction, of a single free rising bubble in quiescent water is reproducible (see chapter 4).

The bubble production mechanism used in the present experiments does not have these drawbacks. An adjustable volume of air determines the size of the bubble. As soon as the bubble is on the top of the capillary, it is almost completely surrounded by liquid. Even within the capillary water is present. For that reason the bubble is always released spherically. Furthermore, the time difference between successive bubble releases can be chosen arbitrarily large. In fact, only one bubble is produced in an experiment. Thus there is no effect of the wake of a preceding bubble.

The nice spherical shape of the bubble at release can be seen in figure 5.2. A trivial consequence of the spherical bubble release without shape and volume oscil-

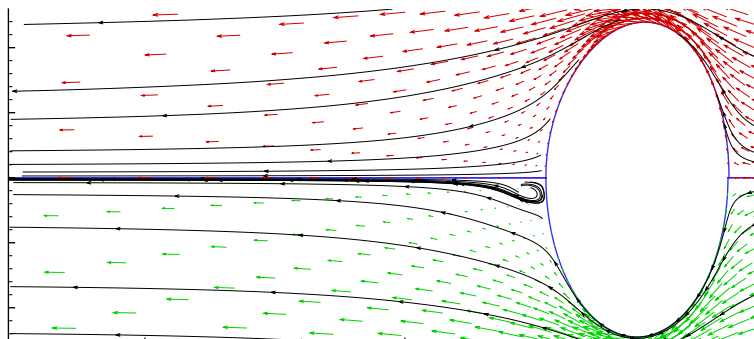


FIGURE 5.3: *The effect of deformability on the configuration of the wake for a bubble of $Re=166$ and aspect ratio of 1.75. In the upper half of the image the computed velocity profile (arrows) and the stream lines for a fully deformable axisymmetric bubble show no attached wake. Contrary to this, a similar calculation for a fixed, ellipsoidal shape with an identical aspect ratio does show an attached wake (lower half).*

lations is the absence of an acoustic signal. In many methods the Minnaert frequency (Minnaert 1933) associated with volume oscillations is used to determine the bubble size. In the author's opinion it is more logical to associate this frequency with a poorly produced bubble. If one is able to determine the size of a bubble from the Minnaert frequency, then these bubbles are not suitable to study the fundamental nature of path instability.

3 Shape effects on the flow pattern

The consequences of the shape deformation on the flow around the bubble can be considerable. In the present study numerical simulations, using the code of Takagi *et al.* (1994), have been performed. The simulations are grid independent. In Figure 5.3 two results are presented. Both calculations, with equally sized bubbles, are performed taking into account a zero tangential stress condition at the bubble surface. In the upper half the bubble shape is fully adjustable and in the lower half the bubble shape remains an ellipsoid. The differences in both shapes are so small that they are not discernible in Figure 5.3. Nevertheless the effects on the flow around the bubble are large. For the fully adjustable, axisymmetric shape no recirculation zone is observed, whereas for the fixed ellipsoidal shape such a zone is clearly visible. It is concluded that calculations assuming a fixed, ellipsoidal shape do not lead to physically correct velocity fields.

A comparison of the present numerical results with those by Blanco & Magnaudet (1995), for the parameter range in which the standing eddy can occur, is

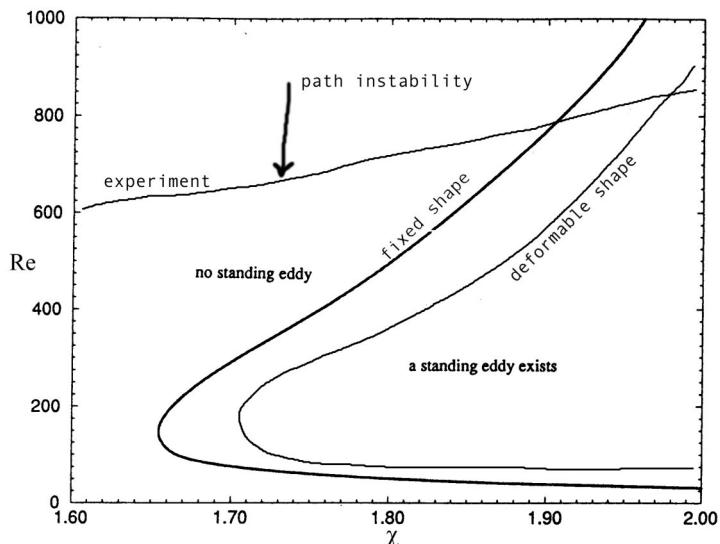


FIGURE 5.4: Plot of Reynolds number versus aspect ratio of the bubble with regimes in which a standing eddy is observed and the point at which path instability sets in. Note that the Reynolds number is based on the major axis instead of the equivalent radius. The curves are the numerical results for fixed and free bubble shapes, respectively. To the right of the curves a standing eddy is observed in the numerical results. Clearly path instability occurs in a regime for which a standing eddy is not observed.

presented in figure 5.4. The present results agree well for a fixed shape (this line is for both Blanco & Magnaudet (1995) and the present calculations). For a bubble that is free to adapt its shape, the formation of the standing eddy, while keeping the Reynolds number fixed, occurs at a larger value of the aspect ratio of the bubble.

It is observed that, indeed, experimentally path instability for bubbles in pure water occurs in a regime in which a standing eddy is not observed behind a bubble. Care has to be taken in comparing wake instabilities observed behind solid spheres with those observed behind bubbles. It is generally accepted that for solid spheres a standing eddy is formed which becomes unstable at a certain Reynolds number. Consequently the origin of the wake instability has to be of another type than that observed behind solid spheres.

Obviously, after the formation of the double-threaded wake the shape of the bubble can no longer be ellipsoidal. In the present simulations it is shown that a minor change of the shape can give a dramatic change of flow pattern. As the change of shape is only minor, the assumption of an ellipsoidal shape of the bubble to determine the position, orientation, drag, etcetera as used in the image analysis program is still valid. Numerically, however, any calculation based upon either fixed or axisymmetric shape may not lead to physically correct velocity fields.

BUBBLE-WALL INTERACTION



Bubbles bouncing against vertical walls have been studied experimentally. Many experiments reported in this chapter are performed in water of 20°C, and thus only the path of the bubbles is recorded. Furthermore, experiments with a temperature gradient are reported to indicate the observations in the wake and during bouncing. Based on the experimental results a model is proposed to explain the variety of observed bubble paths. Crucial for this model are the bouncing criteria and for larger bubbles wake effects similar as the ones discussed in the previous chapter.

1 Introduction

The motion of two interacting bubbles has been studied extensively by Kok (1989, 1993*a,b*) and Duineveld (1994). Two bubbles tend to align horizontally and attract each other. At close approach there are various possibilities: i) coalescence, ii) repeated bouncing followed by coalescence or iii) bouncing followed by separation. The observed motions depend on the fluid properties, the initial distance and the size of the bubbles. Duineveld (1994) determined experimentally the critical Weber number for the transition from one type to the other. The motion of the bubble pair after bouncing could not be explained satisfactorily.

In inviscid flow theory, the effect of a wall on a bubble can be modelled by mirror-imaging the bubble in the wall, i.e. leading to a bubble pair. Coalescence does not occur for a bubble bouncing against a vertical wall. Also the boundary layer, built up during bouncing, is different from the situation for a bubble pair. However, experimentally a bubble-wall interaction is more convenient because the 'bubbles' are necessarily identical and aligned horizontally. In potential flow theory the attraction is captured, but the remarkable bouncing phenomena observed in experiments are not predicted.

Depending on the size of the bubble and the initial distance to the wall, the bubble may slide along the wall, perform multiple rebounds or rebound once without returning to the wall. Often the rebound amplitude is larger than the initial distance

to the wall. Although energy is dissipated by drag, the amplitude of the rebounds will not damp for multiple bounds.

One of the few studies on bubbles interacting with walls was performed by Tsao & Koch (1997). They focussed on surface energy and the effect of deformation of a bubble rising underneath an inclined or horizontal plate. They claim that at the collision immediately up to 95% of the energy contained in the initial kinetic and surface energy is converted in surface deformation. After the rebound a significant fraction (up to 59%) of the bubble's energy is lost and most of this loss occurred just after the collision. They proposed two mechanisms: acoustic radiation and, just after the collision, separation of the boundary layer at the wall.

In this chapter it is suggested that the vorticity built up in the wake of the bubble plays an important role. To study this a similar setup and visualisation technique as described in chapter 3 is used and a model is proposed to explain the motion of the bouncing bubble. The global path of the bubble is experimentally studied with a diffusive side lighting technique.

2 Experimental setup

The experimental setup to study bubble bouncing with a vertical glass wall is comparable with the setup used for the free rising bubbles. A wall (Figure 6.1) is placed in the middle of the water tank with the lower edge at 10 cm above the bottom of the tank. This lower edge was at least 4 cm above the capillary to ensure that the bubble reaches its terminal rise velocity before the lower edge is reached. Note that the horizontal and vertical direction are x and y , respectively. The velocity components are u and v , respectively. The horizontal and vertical distance of the capillary to the bottom of the wall is adjustable.

Although detailed information on the flow around the bubble at bouncing is necessary to understand the motion, many experiments reported in this chapter have been performed without a temperature gradient in the water. This was necessary because a larger viewing area than possible with the schlieren technique is essential to study the path after bouncing. For this purpose a diffusive side lighting technique is used. The bubbles appear as white dots. Using stroboscopic lighting, the position of the bubble at consecutive times are recorded on a single photograph and are then analysed. This results in figures as presented in Figure 6.2.

With such a large viewing area the spatial resolution was too low to determine the shape and wake of the bubble. Furthermore, this large area made it impossible to use of the schlieren setup as the intensity of light was too low, and the viewing area was limited by the size of the lenses (10 cm) to produce a parallel beam.

While the strength of the diffusive side lighting technique is in visualising the global path of the bubble, the schlieren technique is useful in visualising the flow

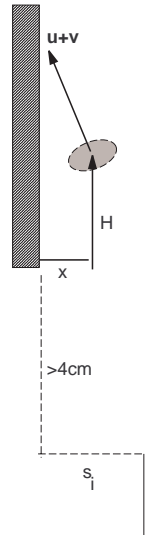


FIGURE 6.1: *Experimental bounce setup. The vertical distance of the lower edge of the vertical wall is at least 4cm above the capillary. The horizontal distance of the capillary and the wall, s_i , is adjustable. The horizontal and vertical coordinates are x and y , respectively. The associated velocity components are u and v .*

locally. For this reason both experimental techniques are used to study the path and wake of bouncing bubbles.

In the diffusive side lighting technique the illumination is from the side through a diffusive screen. As a result the background is black and the bubble reflects some light into the camera and the position of the bubble can be determined. However, flow visualisation is not possible with the side lighting technique. Schlieren is used to visualise the flow around the bubble just before, at and after bouncing.

A problem arises in the schlieren visualisation of the flow very close to the wall. This is due to the the mirror being placed inside the tank (Figure 3.1) and the wall stretches over the width of the tank. In this way it can not be avoided that a small gap exists between the mirror and the wall and the parts very close to the wall can not be visualised. This problem can be avoided by placing the mirror outside the water tank (or only recording a single view).

Another option is the use of a narrower wall, which allows space for the mirror to be placed next to the wall. This might be pursued in the future. From two perpendicular views it has been observed that the motion is in a single plane perpendicular to the vertical wall and as a result a single view is sufficient.

The wall is aligned with a plumb line outside the water tank and checked after refilling and cleaning of the tank. Over a length of 25 cm the distance from this plumb line and the wall was determined with a camera, accurate to 3 pixels overall. This implies that the maximum error of misplacement of the wall was 0.2 mm or 0.2° . Even this small error in the angle can have a large effect on the experimental results, as will be shown in § 4. The distance of the capillary to the wall was measured as the distance to the plumb line. Next to this the size of the bubble is determined as

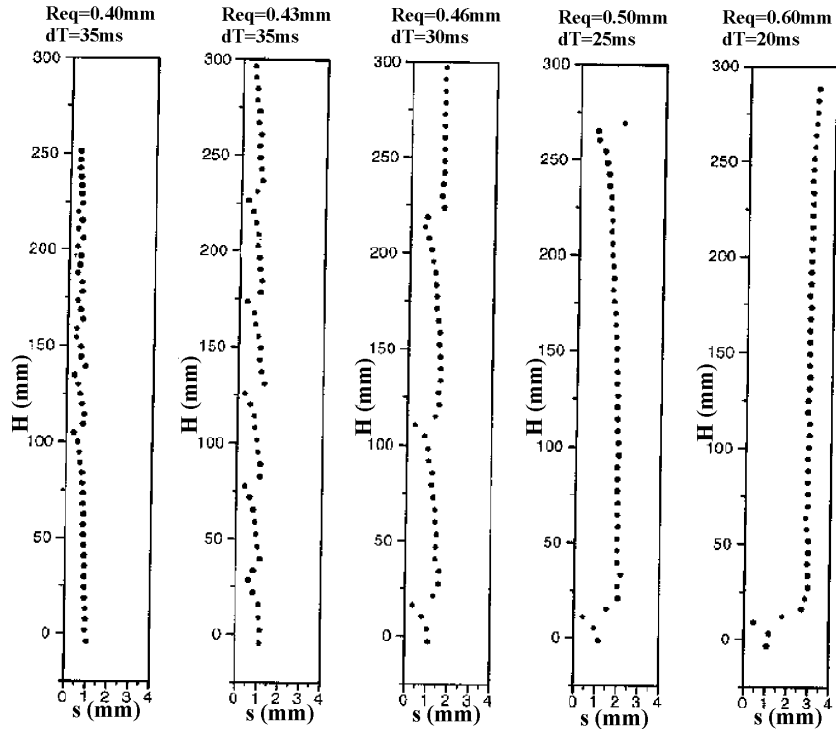


FIGURE 6.2: Bubbles of different size bouncing against a vertical wall at an initial distance $s_i = 1.16\text{ mm}$. dT is the time interval in milliseconds between recordings of the bubble. On the left sliding bubbles, in the middle bouncing bubbles and on the right bouncing followed by separation is observed

described in chapter 3. The same precautions and checks as mentioned in chapter 3 on the purity of the water and the accuracy of the capillary are taken.

3 Experimental results

3.1 Path of bouncing bubbles

The behaviour of bubbles bouncing against a vertical wall observed in pure water of homogeneous temperature is remarkable. Depending on the initial distance (s_i) to the wall and the bubble size (r_{eq}), bubbles are observed either to slide along the wall, to rebound repeatedly, to rebound once and separate from the wall, or to rebound repeatedly at very large amplitudes (up to 3 times s_i). For several s_i the bubble size is varied to check which parameter dominates the transition from one type of bouncing to the other.

In Figure 6.2 $s_i = 1.16\text{ mm}$ and the bubble radius increases from left to right.

The vertical axis denotes the distance, H , from the lower edge of the vertical wall and the horizontal axis is the distance to the wall. Note that the axes have different scales. The smallest bubble, $r_{eq} = 0.40$ mm, rebounds several times and then slides along the wall. This bubble appears to perform an elastic collision, meaning that the vertical velocity is maintained and the horizontal velocity changes sign. The amplitude of the bounds is reduced after each bounce and after a number of bounces the bubble slides along the wall.

Increasing the bubble size only slightly to $r_{eq} = 0.43$ mm changes the behaviour significantly. The bubble continues to bounce at a constant amplitude. For a bubble with $r_{eq} = 0.46$ mm a similar behaviour is observed, but now the amplitude of the bounds is larger than the initial distance to the wall and a much larger bound length in vertical direction. Furthermore, it is noticed that for both bubbles the collision is no longer perfectly elastic. The vertical velocity is reduced significantly to about 10% of U_T .

The parameter distinguishing these two motions, sliding and multiple bouncing, appears to be the Weber number, We_{cr} , based on twice the bubble horizontal velocity component (approach velocity of the line of centres of bubble and image bubble). This approach velocity is taken to be twice the horizontal velocity to enable comparison with We_{cr} found for a bubble pair, distinguishing coalescence and bouncing. Duineveld (1994) empirically determined $We_{cr} = \frac{2\rho r_{eq} u^2}{\sigma} = 0.18$ above which bubbles bounce, with u the approach velocity.

Determining the approach velocity from the results presented in Figure 6.2 is not recommendable because the time interval between the recordings of the bubbles is too large, 20-35 ms. Because of this the bubble closest to the wall can be the last bubble just before bouncing or the first after bouncing and the estimates of the approach velocities are not accurate. The average velocity over a time interval of 20-35 ms is not a good indication for the horizontal velocity at bouncing. However, high-speed recordings of the bubbles bouncing with a vertical wall provided good estimates of the approach velocity, ≈ 0.12 m/s. The transition from sliding to multiple bouncing is observed for bubbles of $r_{eq} \approx 0.42$ mm and $We_{cr} = 0.165$. It is remarkable that a more or less equal bouncing criterion for a pair of bubbles and a single bubble bouncing against a wall is found. This certainly is a strong indication for the analogy of both systems.

It has to be kept in mind that Duineveld (1994) proposed a model for coalescence based on the rate of film thinning between two bubbles. From the above results it appears that the present sliding case is comparable to the coalescence case. For a bubble approaching a wall similar arguments of film thinning can be used and therefore one may expect comparable results.

Finally for $r_{eq} = 0.60$ mm the bubble bounces only once and separates from the wall. The attraction force quickly decreases with increasing distance to the wall, but

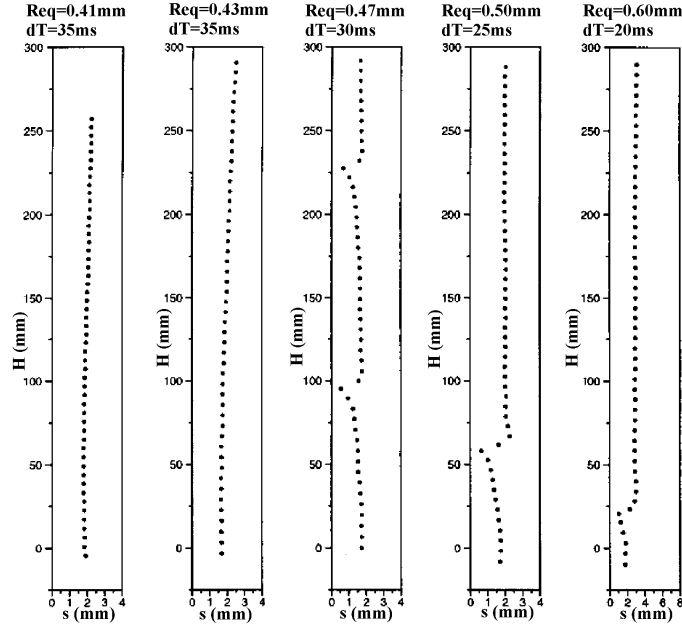


FIGURE 6.3: Bubbles of different size bouncing with a vertical wall at an initial distance $s_i = 1.57\text{ mm}$. No sliding bubbles are observed.

never becomes zero. Therefore a repulsive force is expected, which will be shown to be a component of gravity.

For an initial distance $s_i = 1.57\text{ mm}$, Figure 6.3 shows a very similar behaviour, except for the very small and very large bubble sizes. Small bubbles do not bounce against the vertical wall, but move away from the wall. Since in potential flow the only force in the horizontal direction is an attraction force something strange is happening here. From the results of the model (see section 4) a possible explanation for this bouncing-separation is a slightly tilted wall. Even a tilt within the experimental accuracy of 0.2 degrees appears to be sufficient to explain these motions. For a straight rising bubble such a tilt in the wall will result in an increasing distance to the wall. Or in other words, there will be a component of gravity perpendicular to the wall compensating for the attraction force or even driving the bubble away from the wall.

This effect also explains the bouncing-separation seen for example in Figure 6.3 for $r_{eq} = 0.50$ and 0.60 mm and Figure 6.2 for $r_{eq} = 0.50\text{ mm}$. As the bubble bounce amplitude is large, the attraction force becomes small. In some cases this force is equal or smaller than the component of gravity driving the bubble away from the wall. As a result the bubble is observed to bounce only once.

Presumably bubbles bouncing only once and then moving almost parallel to the

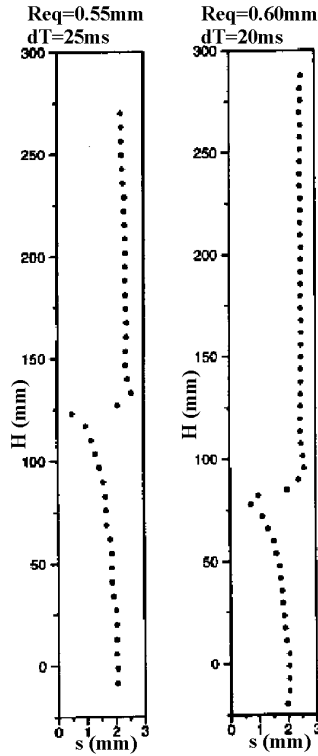


FIGURE 6.4: *Small bubbles at a large initial distance $s_i = 2.17$ mm.*

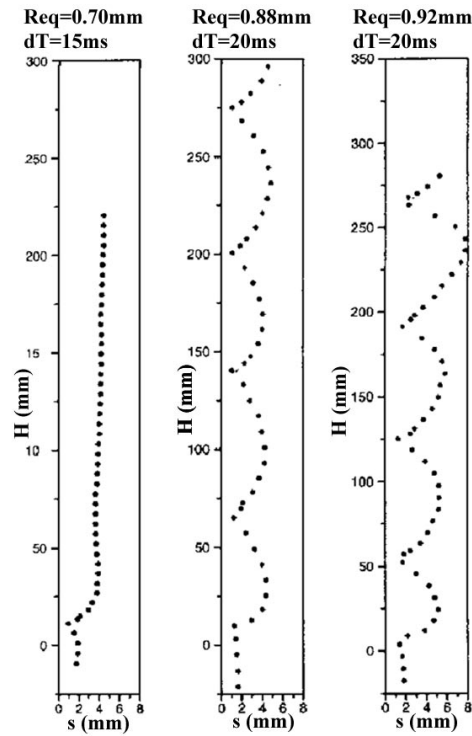


FIGURE 6.5: *Large bubble at an initial distance $s_i = 1.57$ mm. For very large bubbles the multiple bounces reappear. These bounces have very large amplitudes compared to their initial distance to the wall.*

wall, is a result of a small misalignment of the wall. Unfortunately this misalignment is within the accuracy of the alignment procedure. On purpose misalignment of the wall resulted, as expected, in either never bouncing bubbles or always multiple bounces depending on the direction of the misalignment.

In Figure 6.4 the distance $s_i = 2.17$ mm is even larger, confirming the previous observations, and no new phenomena are observed. However, when the bubble size is increased further, for a fixed $s_i = 1.57$ mm, than already seen in Figure 6.3, a new phenomenon is observed. In Figure 6.5 the smallest bubble bounces only once, which phenomenon is already explained. However, for the larger bubbles multiple, very large bounds are observed. The bounds lengths and amplitudes are no longer constant, but can even grow for consecutive bounds: for example the bound after the

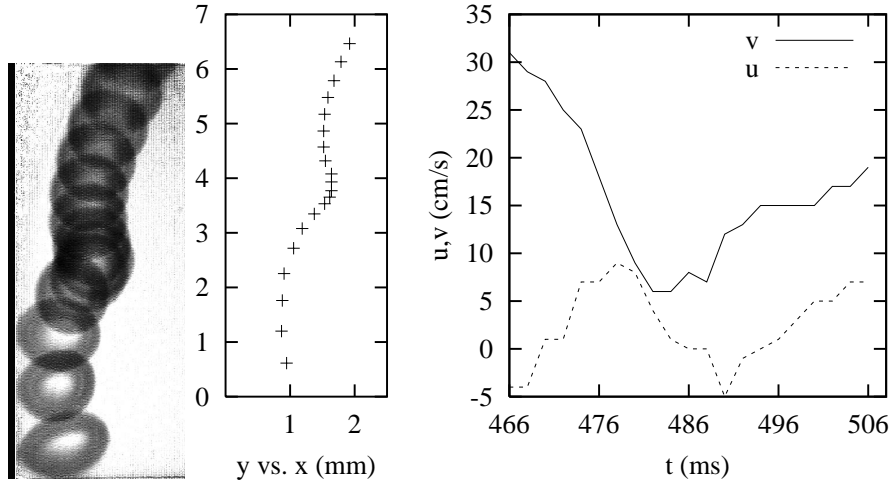


FIGURE 6.6: *The first bounce for a bubble ($r_{eq} = 0.84$ mm and $s_i = 1.5$ mm) with a vertical wall. The bubbles are obtained from separate frames with 4 ms time difference. The bubble shapes can be seen on the left, on the right are plots of the position and velocity of the bubble's centre, respectively.*

fourth bounce for $r_{eq} = 0.92$ mm.

The reappearance of the multiple bounds can not be explained by any obliqueness of the wall. This reappearance occurs for bubble sizes at which a free rising bubble, see Chapter 4, would perform a zigzagging or spiralling motion. With help of flow visualisations it will be shown that for these large bouncing bubbles, as for the spiralling and zigzagging bubbles, a double-threaded wake plays an important role in the motion of the bubble. This remarkable bouncing for large bubbles is not seen for small initial distances as the critical approach Weber number is not reached at the first bounce and the bubbles will slide along the wall. For a large bubble with a small initial distance, the distance of the bubble surface to the wall is very small. Consequently there is only a short time to build up horizontal velocity and the approach velocity is too low to reach the bouncing regime.

Zooming in on the region of the first bounce gives more details of the shape and the path of the bubble. In Figure 6.6 the bubble behaviour is displayed by placing bubbles from frames with 4 ms time differences in one figure. The first bubble (lowest, $t = 466$ ms) shows the shape of the bubble just before hitting the wall. This bubble has a strongly deformed stable shape and a large velocity. The shape is an oblate ellipsoid. Experiments show that the minor axis coincides with the direction of motion of the bubble. Without any calculations this already indicates the large ratio of the vertical and horizontal velocity components at bouncing. Calculating

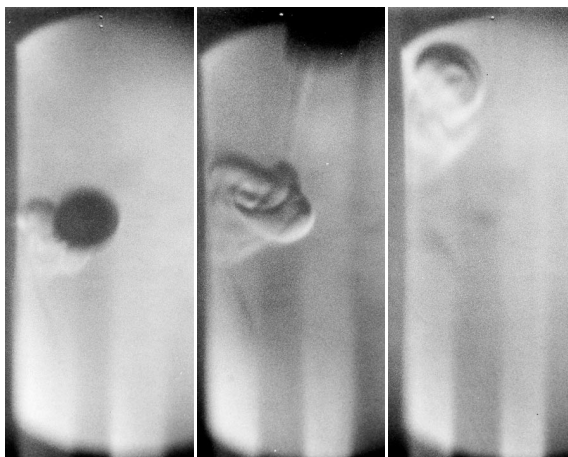


FIGURE 6.7: *Formation of a vortical region for a bouncing bubble ($r_{eq} = 0.85$ mm). The time intervals between the pictures are 26 ms and 60 ms, respectively. Clearly visible the vertical motion of the vortical region.*

the velocity of the bubble by numerically differentiation of the path gives a vertical velocity of 32 cm/s and a horizontal velocity of -6 cm/s just before bouncing.

Only 4 ms later, the bubble's shape has changed significantly and has become nearly spherical. In this stage the bubble appears to be sliding along the wall and the vertical velocity component is decreasing. However, the lowest vertical velocity component occurs after the bubble has bounced.

Just after bouncing ($t=474$ ms), the bubble quickly increases the distance to the wall and the vertical velocity component drops from 23 cm/s to about 6 cm/s. At $t \approx 482$ ms the bubble motion becomes vertical. Then the bubble's distance to the wall is decreasing slightly and the vertical velocity is still small. Subsequently, the rising bubble accelerates more and moves away from the wall.

The errors made in the numerical determination of the velocity components (Figure 6.6) is estimated to be 10%. All other experiments for medium sized and large bubbles confirmed the trends reported here. From the plots the drop in the vertical velocity is striking. This drop in vertical velocity occurs after the bubble has left the wall and as such can not be a direct wall effect. It is as if the bubble reaches a down-flow area, as discussed in § 3.2.

3.2 Flow visualisation of bouncing bubble

For the flow visualisation the previously mentioned schlieren technique, with linear temperature gradient, is used. From the results reported in the previous section it is clear that something remarkable happens at bouncing of medium sized bubbles. Since for an initial distance of $s_i = 1.57$ mm all phenomena occur, depending on the

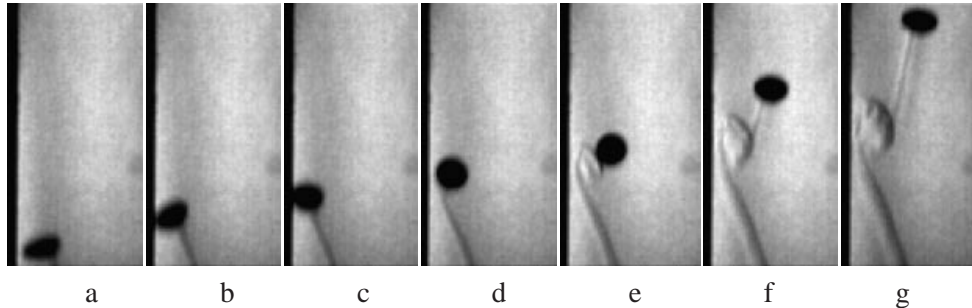


FIGURE 6.8: *Formation of a vortical region for a bouncing bubble ($r_{eq} = 0.90$ mm) and $s_i = 1.57$ mm. The time intervals are not identical, the total time from left to right is 80 ms.*

bubble size, the schlieren images were performed for $s_i = 1.57$ mm and the results presented here can be related to Figures 6.3 and 6.5.

The schlieren images in Figure 6.7 show the formation of a vortical region, which is observed for medium and large bubbles. This vortical region appears to consist of the vorticity accumulated at the rear of the bubble, which is shed as the bubble bounces, and the vorticity in the wake impinging on the wall. This vortical region is expected to affect the motion of the bubble. Furthermore, as the bubble approaches a boundary layer is formed along the wall. This may influence the bouncing.

After the bubble has bounced, the vortical region still further develops and forms a spherical blob. The blob then moves upwards with an initially increasing velocity. From this it can be expected that the motion of this vortical blob is self-induced. The final rise velocity of this vortical blob is about $0.2U_T$, where U_T the terminal rise velocity of the bubble.

Although the exact configuration of the vortical blob is unknown, it hypothesised here that this spherical vortical blob, together with its image, is a Hill's spherical vortex. In the model to be discussed the vortical region is modelled as such. As the size of the blob is comparable with the size of the bubble the strength of the Hill's spherical vortex can be determined (see section 5). In the real situation the configuration of the vortical blob is probably not exactly a Hill's spherical vortex, however this will not lead to large differences in the results of the model.

The flow visualisation of the first bounce in Figure 6.8 is related to the case of multiple bouncing in Figure 6.5. In Figure 6.8 a double-threaded wake can be observed, especially in image g. Before the bubble bounces with the wall the plane of the two threads is parallel to the wall (only one is visible). The two threads have been observed in experiments visualisations in the perpendicular direction. After bouncing the double-threaded wake has disappeared for some time, and the attached vorticity was shed at bouncing. Like for a free rising bubble, the attached vorticity is built

up again, before any vorticity is transported into the wake. Then again the double-threaded wake is formed which initially lies in the view plane (Figure 6.9). Quickly the wake reorientates to the orientation it had before bouncing (Figure 6.10). This final orientation of the vortex filaments is associated with a lift force perpendicular to the wall.

From the momentum conservation principles as discussed in Chapter 4 the direction of the lift force can be deduced. Note that for the bubble sizes $r_{eq} > 0.80$ mm a double-threaded wake is observed, and free rising bubbles perform a zigzagging or spiralling motion. The bubble sizes used in this section are related to zigzagging and spiralling motions, and thus a double-threaded wake is expected.

Just after bouncing no double-threaded wake is observed, but soon a double-threaded wake evolves. The initial orientation just after bouncing is arbitrary, but in most experiments it is observed that the plane of the filaments is perpendicular to the wall. However, as the initial motion is horizontal and the bubble is accelerated due to buoyancy, there is a deflection of the path upwards. It is this curvature of the path towards the wall which reorientates the double-threaded wake. This orientation is associated with a lift force directed towards the wall (Chapter 4.2.2).

The previous analysis of the orientation of the double-threaded wake is given between two consecutive bounces. The reason for this is that the trajectory of a path-unstable bubble before the first bounce cannot be predicted beforehand. From the experiments of a free rising bubble (Chapter 4) it is clear that the path of the bubble is not reproducible. Especially the direction of the first deflection is arbitrary. Thus the mean position of the zigzag is not directly above the capillary. The capillary is placed at a horizontal distance from the wall. Then two extreme cases can occur for a zigzagging bubble: i) an initial displacement of about 2 mm towards the wall, ii) an initial displacement of about 2 mm away from the wall.

In the first case for all bouncing experiments reported in this thesis the central position falls within or behind the wall. Depending on the phase of the zigzag the bubble may bounce against the back of the wall, against the lower edge of the wall or against the front side of the wall. Only the last case is used for the present analysis. The orientation of the wake just before bouncing results in a lift force directed towards the wall.

The second case would lead to a zigzagging bubble relatively far from the wall. At the point at which the bubble is 'closest' to the wall, maximum of the zigzag, the lift force associated with the zigzagging motion is directed away from the wall. As long as this repelling lift force is larger than the attraction force of the wall, the bubble will maintain its zigzagging motion. However, the attraction force of the wall is responsible for the fact that the mean position of the zigzag comes close to the wall.

In due time the distance from the wall reduces up to the moment that the max-

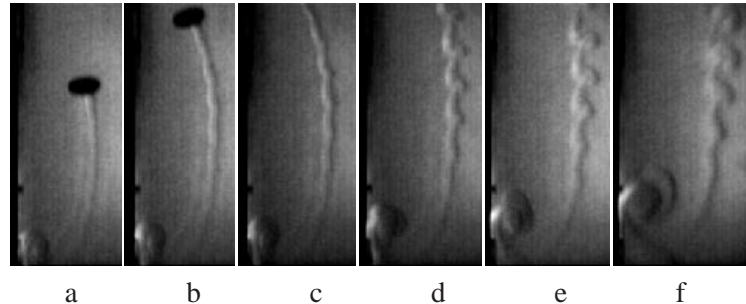


FIGURE 6.9: *The path and wake of a bubble $r_{eq} = 0.97$ mm and $s_i = 1.57$ mm just after the first bounce. Clearly visible the instability of the wake and the vertical motion of the vortical region formed at bouncing.*

imum attraction force, is larger than the lift force originating from the wake. Then the curvature of the path will change and the lift force on the bubble will become directed towards the wall. Although bubbles will bounce much later against the wall, the wake has a similar orientation as in the first case and results in a lift force directed towards the wall. Both cases indicate that before every bounce the plane through the filaments is approximately parallel to the wall.

Furthermore, the previously observed small velocity reduction as the bubble slides along the wall (Figure 6.6, $t = 466 - 474$ ms), and the subsequent horizontal displacement, can be caused by the inertia of the wake of the bubble. Although one would expect that the vertical velocity of the bubble would drop significantly at the time the bubble slides along the wall, the largest reduction in the vertical component of the velocity occurs after this sliding region. The wake is observed to first push the bubble forward sliding along the wall, and after the bounce the wake moves in between the wall and the bubble, thereby displacing it horizontally. This is clearly seen in Figure 6.8 (e-g), where the vortical region is formed and moves upwards. This vortical region pulls the bubble, which causes the drop in vertical velocity.

The subsequent negative horizontal velocity ($t = 486$ ms) can be explained by the nature of the development of the vortical blob near the wall. This vortical region has an effect on the motion of the bubble. This effect is comparable to the reduction of the vertical velocity component for a bubble in a horizontally aligned, rising bubble pair.

As in chapter 4, a double-threaded wake is observed to become unstable (Figures 6.9 and 6.10). In Figure 6.9 the wake instability is shown just after the first bounce. The wake clearly reorientates and the two threads align to a plane perpendicular to the viewing plane, thus parallel to the wall. In this way only one thread is observed. Starting from image c the instability is developing and clearly showing similar patterns as observed for the free rising zigzagging bubble as in Figure 4.3.

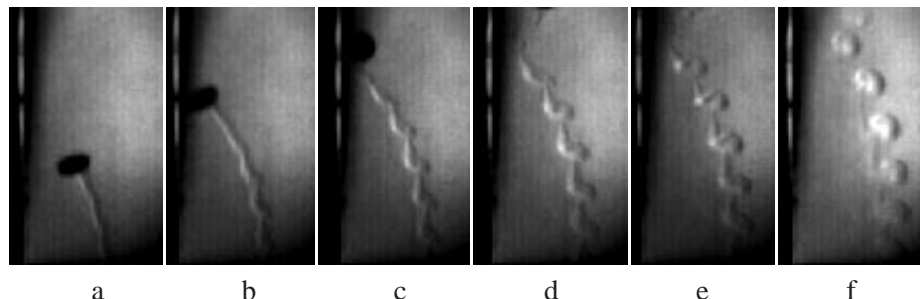


FIGURE 6.10: *The path and wake of a bubble $r_{eq} = 0.98$ mm just before the second bounce. Clearly visible the reorientation of the wake into vortical regions.*

Especially in the last image the reorientation of the double threads is seen to form dipole, or ring vortex, like structures.

The time scale for the appearance of the instability of the double-threaded wake differs from the time scale observed for spiralling bubbles (Figure 4.11). In the latter the Crow instability has not appeared yet. If we compare the time scale in the present case with that observed for zigzagging bubbles a good agreement is found. For zigzagging this short time scale was due to the large disturbance of the filaments by reconnection followed by reappearance of the double-threaded wake with opposite sign. This would indicate that there is also a large disturbance in the bouncing case.

One disturbance is the vortical region formed at bouncing. The development of this vortex blob at the wall can be observed. The final image shows a spherical shape of this vortical blob as well as the onset of the self induced motion of this vortical blob. This is exactly as seen in Figure 6.7.

Another disturbance can be seen in Figure 6.8 image f. Just after bouncing the double-threaded wake has disappeared. In the successive image, g, the double-threaded wake is formed again. This is very comparable to the disturbances observed for zigzagging bubbles; a double-threaded wake forms out of a single thread.

Note that for two bouncing bubbles ($r_{eq} > 0.86$), close to the critical size, $r_{eq} = 0.91$ mm, for path instability of a free rising bubble, Duineveld (1994) observed bouncing followed by separation for a bubble pair. Duineveld suggested that the bounce would trigger the instability of the wake and the shedding of vortices. In the present experiments vortex shedding has not been observed. Although in the present experiments bubbles with a size slightly smaller than the critical size for path instability show bouncing separation, for bubbles larger than this critical size the reappearance of multiple bounces is observed. The question now remains, why these multiple bounces have not been observed for a bubble pair.

In Figure 6.10 bubble path and wake between first and second bounce are shown. The curvature of the path is larger than observed in Figure 6.9. The instability in the

wake is observed to occur even closer to the bubble. It appears that the time scale of instability reduces for increasing curvature of the path. Still the observed instabilities are similar to those observed just after bouncing. Especially the last image really shows the dipole-shaped vortices. The frequency of the formation of these dipoles is comparable to that observed far behind zigzagging bubbles. These structures are indeed related to the Crow instability.

These dipole-shaped vortices will have a large effect on the motion in the water behind the bubble. Contrary to the present production method, a continuous bubble injector system based on a constant air flux through a needle will produce a bubble at least every 5 seconds. As soon as bubbles are continuously produced these vortices will influence the motion of the next bubbles. As the lifetime of these vortices is in the order of seconds, they can not be neglected. As a result the motion of the bubble will be influenced by the previous bubble and the development of the wake will change.

Furthermore, it is expected that similar vortex structures will be formed by bubbles in turbulent bubbly flows. This is a possible explanation for the modification of turbulence by bubbles. Some of the aspects involved will be discussed in Chapter 7.

In Figure 6.11 the shape deformations of a bouncing bubble are clearly visible. Just before bouncing the bubble is ellipsoidal and just after the bounce shape oscillations are observed. In the last image of Figure 6.8 the shape of the bubble is ellipsoidal again. In this regime the bubble is still accelerating, but near its maximum vertical velocity resulting in an ellipsoidal shape.

In Figure 6.12 the image a and b show a stable wake. The first bubble ($r_{eq} = 0.78$ mm) is just below the size for which a free rising bubble would perform zigzagging or spiralling motion and a stable wake is expected. Although the curvature of the path, and the herewith related production of vorticity, could have triggered the formation of a double-threaded wake for a smaller bubble, this is never observed. Note that the angle at which this bubble hits the wall is small.

In image b a probably path unstable bubble ($r_{eq} = 0.84$ mm) is shown, but still with a stable wake on the short time scale is observed. After the bounce no double-threaded wake is observed. Observation for equal sized bubbles on the perpendicular view show the double-threads. Also later images show the onset of the wake instability. From those observation a double-threaded wake is expected.

An important question is whether the information of a double-threaded wake can be obtained from image b itself? The answer is yes. A bubble with a double-threaded wake bouncing against a wall has a lift force added to the attraction force of the wake. From a larger attraction force a larger horizontal velocity is expected at bouncing. This larger horizontal velocity is visible. The angle between the wake and the wall just before bouncing, for both image a and b, is larger than observed for bubbles with a single-threaded wake (image a). So images a and b should have, and

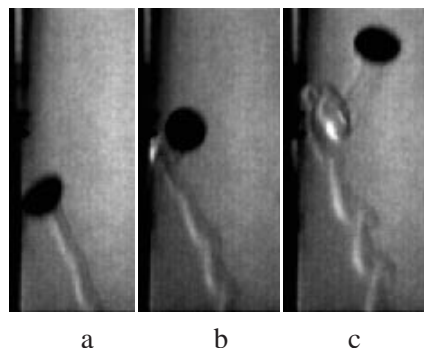


FIGURE 6.11: *Close up of the path and wake in the bouncing regime ($r_{eq} = 0.99$ mm).*

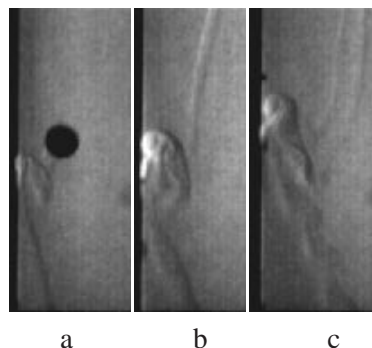


FIGURE 6.12: *Differences in the development of the wake for different sizes of bubbles. a) Stable wake $r_{eq} = 0.78$ mm, b) stable wake $r_{eq} = 0.84$ mm, and c) unstable wake $r_{eq} = 0.93$ mm.*

have, double-threaded wakes.

In image b the plane through the filaments after bouncing is aligned parallel to the wall, whereas the vortex filaments in image c are in the view plane. Another difference between image b and c, except the size, is the time scale at which the wake instability sets in. The bubble of the last image is larger and so the strength of the vortex filaments is larger. This is a possible explanation for the time scale at which the instability sets in.

This larger strength of the vortex filaments is visible in another difference in the images. The angle between the wake and the wall of the bounce in image c is slightly larger, although a smaller angle was expected, as there is less time for a larger bubble to develop its horizontal velocity. Another example of a short time scale stable double-threaded wake can be seen in Figure 6.8 a-g. Again observe the larger angle of the bounce. In this image the double-threaded wake is visible after bouncing.

In conclusion the rate at which instabilities of a double-threaded wake develops is dependent on the strength of the vortex filaments, the disturbance on these filaments and the curvature of the path. The behaviour of bubbles of different size seen in these experiments are distinguished by the bouncing criterion based on the approach Weber number, the vertical alignment of the wall and the configuration and strength of the wake. In the following section these aspects will be captured in a model.

4 Model

Small bubbles, up to 0.60 mm in radius, have been observed to remain spherical. In the experiments with these small bubbles remarkable bouncing was observed. A gen-

eral description, using Lagrange's formalism, of the equation of motion of bubbles in a low viscosity liquid is given by Kok (1993a). The drag forces are derived from the rate of viscous dissipation and the effect of hydrodynamical interaction is taken into account. These general equations of motion can be adapted to calculate the bouncing behaviour of two rising spherical bubbles, with the line of centres in a horizontal plane. The picture is comparable with a bubble bouncing with a vertical wall. This model could accurately reproduce the attraction to the wall. However, the peculiar bouncing phenomena cannot be described with this model. Equations (28) and (29) in Kok (1993a) are the general equations of motion of a pair of spheres, or spherical bubbles. In the case of a bubble bouncing with a vertical wall, these equations reduce to

$$\begin{aligned}\rho V \frac{dM_y \dot{y}}{dt} &= F_y, \\ \rho V \frac{dM_x \dot{x}}{dt} &= \frac{1}{2} \rho V \left[\dot{y}^2 \frac{dM_y}{dx} + \dot{x}^2 \frac{dM_x}{dx} \right] + F_x,\end{aligned}\quad (6.1)$$

where x is the distance from the wall, y is the vertical height above the lower edge of the wall, V is the volume of the sphere, M_x and M_y the added mass coefficients and F_x and F_y the external forces acting on the pair of spheres. Furthermore, the horizontal and vertical velocity components are u and v , respectively. In the first instance the external forces are buoyancy and drag \mathbf{D} acting on the bubble pair. From Kok (1993a), taking only the contributions of dipoles into account,

$$M_x = 1 + \frac{3}{8} \left(\frac{r_{eq}}{x} \right)^3, \quad (6.2)$$

$$M_y = 1 + \frac{3}{16} \left(\frac{r_{eq}}{x} \right)^3, \quad (6.3)$$

$$F_x = -D_x, \quad (6.4)$$

$$F_y = 2\rho gV - D_y, \quad (6.5)$$

$$D_x = -24\pi\nu r_{eq} \dot{x} \left(1 + \frac{1}{4} \left(\frac{r_{eq}}{x} \right)^3 \right), \quad (6.6)$$

$$D_y = -24\pi\nu r_{eq} \dot{y} \left(1 + \frac{1}{8} \left(\frac{r_{eq}}{x} \right)^3 \right). \quad (6.7)$$

The above equations are for spherical bubbles, which simplifies the calculation and allows to obtain a qualitative picture of what happens, also for ellipsoidal bubbles.

In particular this model gives qualitatively the correct behaviour for small bubbles, which end up sliding along the wall. However, the bouncing phenomenon could

not be captured in this very simple model. From the present experiments it can be concluded that for bouncing bubbles the velocity component tangential to the wall (v) becomes very small or even vanishes (e.g. Figure 6.6). The transition between the regimes of sliding along the wall and bouncing is determined by the critical Weber number based on the approach velocity.

The Weber number obtained from the model for a $r_{eq} = 0.42$ mm bubble at an $s_i = 1.16$ mm is $We = 0.165$. Experimentally this bubble size was observed to be the first bouncing bubble. The Weber number is in excellent agreement with the value $We = 0.163$ found in experiments (Figure 6.6) and in good agreement with the critical Weber number $We_{cr} = 0.18$ for the bouncing of a bubble pair determined by Duineveld (1994) (see also § 3.1). $We_{cr} = 0.165$ is used as transition parameter for all calculations with this model.

In the present experiments the drop in tangential velocity was observed over the first 20 ms after the collision (see Figure 6.6 $t=466-486$ ms). This velocity drop is related with the vortical blob seen in the experiments (e.g. Figure 6.2). To catch this vortical region in any calculations the full Navier-Stokes equations for a deformable bubble bouncing with a vertical wall should be solved. This is far beyond the numerical possibilities. However, in the model the interest is in the qualitative behaviour of bouncing only. In the model this velocity drop is assumed to occur instantaneously at the time of collision.

In case of bouncing, $We \geq We_{cr} = 0.165$, the bounce is modelled as an elastic collision in the perpendicular direction. A no-slip condition holds in tangential direction ($u \rightarrow -u, v \rightarrow 0$). It can be shown that this results in up to 97% kinetic energy loss at bouncing. For the bouncing bubble presented in Figure 6.6 the kinetic energy just after bouncing would reduce to $u^2/(u^2 + v^2) \approx 4\%$ of the value just before bouncing. In case of sliding, $We < We_{cr} = 0.165$, the bounce is modelled as an elastic collision in both direction ($u \rightarrow -u, v \rightarrow v$). The bounce amplitude is quickly damped by dissipation and $u \rightarrow 0$.

The attractive force of the mirror bubble, is proportional to the velocity of the bubbles, squared, and becomes therefore smaller when the velocity is reduced at bouncing. In the present experiments it is observed that the velocity tangential to the wall becomes very small or even vanishes and the component perpendicular to the wall changes sign for bouncing bubbles. However the magnitude of the horizontal velocity is unchanged and with a smaller force to slow down the bubble upon separation a larger bounce amplitude can be made plausible. In principle this mechanism explains how, remarkably, a loss of kinetic energy can explain a larger bounce amplitude.

In the present calculations several phases have to be described: free rising and attraction to wall, collision and after collision. These will be discussed separately.

4.1 Free rising and attraction to wall

The bubble is released in a quiescent liquid with zero velocity. The forces acting on the bubble are buoyancy and drag. As soon as the acceleration of the bubble becomes negligible a vertical wall is placed with the lower edge in $x = 0$, $y = 0$, with the bubble in $x=s_i, y=0$. Then this system is similar to a bubble pair at an initial distance of $2s_i$ and the equations of motion for a bubble pair (6.1) can be used.

Physically speaking the mirror image of the bubble will induce a velocity in the bubble resulting in an attraction of the bubble towards the wall. The acceleration of the bubble is now determined by buoyancy, drag and this attraction force. The latter is in the equations of motions captured in the terms with the gradients of the added mass coefficient.

4.2 Collision

In the experiments the vertical velocity drop for bouncing bubbles is observed to occur in a few milliseconds. In the model this drop is assumed to occur instantaneously.

As soon as the bubble hits the wall ($x \leq r_{eq}$) the Weber number based on the approach velocity is calculated, which determines the type of bounce: for $We < We_{cr}$ sliding along wall ($u \rightarrow -u, v \rightarrow v$), for $We \geq We_{cr}$, bouncing ($u \rightarrow -u, v \rightarrow 0$). In the first case the potential flow solution, including drag, of a bouncing bubble is applicable; soon the bounce amplitude is damped by dissipation. In the bouncing case, the vertical velocity component becomes very small (in the model zero) which immediately decreases the bubble attraction force, which is proportional to the velocity squared. In general $v \gg u$ just before bouncing.

The bouncing case may be interpreted as a mass-spring system consisting of many equivalent springs. Initially the springs are stretched and the velocity of the mass is zero. Subsequently the mass accelerates till the springs reach their rest length. At that moment the mass is moving with a velocity of u and bounces elastically with a wall. The velocity becomes $-u$. At that time the springs are cut all but one. This results in a lower spring constant and enables a larger stretch of the spring than the initial one. After a while all the springs are reconnected to the mass and thus the spring constant is increasing. The rest length has not changed. The bubble returns towards the rest length and at that moment the same bounce occurs again. Without drag the velocity at this time is larger than u and the consecutive stretching is increased again and again. With drag the maximum stretch length is bounded as is the bounce amplitude of a bubble bouncing with a vertical wall. For the bouncing bubble the attraction force is changing in a similar way as the force for the different springs. Admittedly the springs are very peculiar as the force each spring exerts on the mass is decreasing as the spring is further stretched.

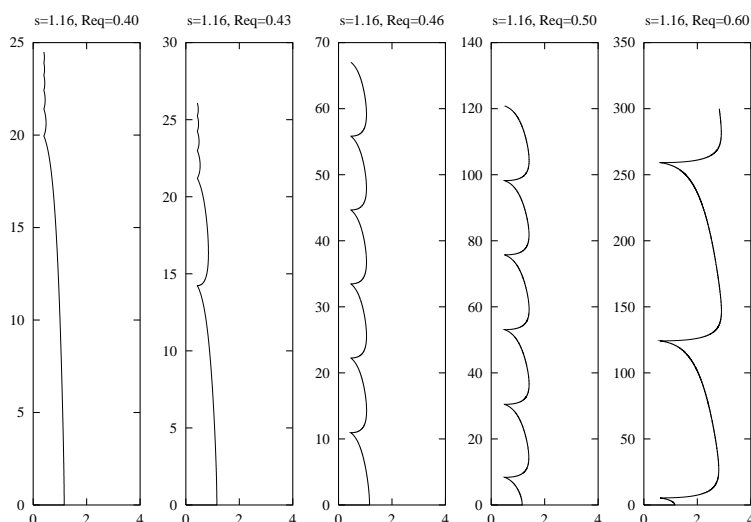


FIGURE 6.13: *The results of the model for several sizes of bubbles for $s_i = 1.16$ mm. Note the different scaling of the axes. The transition between sliding and bouncing is qualitatively comparable to the experiments, but for larger bubbles bouncing separation was not observed.*

4.3 After collision

After the bounce the motion of the bubble can again be described by the equations of motion (6.1). In case of sliding the bounce height will become zero almost instantaneously. For a bouncing bubble the vertical velocity is reduced significantly and thus the attraction force becomes negligible. The bubble bounces away from the wall and gravity will accelerate the bubble again towards its terminal velocity. The attraction force is increased and the bubble will experience another bounce. The maximum distance to the wall can be larger than the initial distance to the wall.

Results obtained with this model are shown in figure 6.13 for various bubble sizes and an initial distance to the 'wall' (half the distance between the two bubbles) of 1.16 mm. The approach velocity at bouncing is predicted accurately; experiments for a $r_{eq} = 0.84$ mm bubble (Figure 6.6) give $u = 6$ cm/s, the model predicts $u = 6.1$ cm/s. The critical Weber number based on the approach velocity is chosen in such a way that the transition between sliding and bouncing occurs for bubbles of 0.42 mm, as observed in experiments. It was shown that a value of $W_{e_{cr}} = 0.165$ is appropriate. The sliding motion of small bubbles ($r_{eq} < 0.42$ mm) is predicted accurately.

The motion of the slightly larger bubbles does show the multiple bounces, but the amplitude of the bounces is lower than observed experimentally (Figure 6.2) and the bounce length is of by a factor 10 (model: ≈ 10 mm, experiment: ≈ 100 mm).

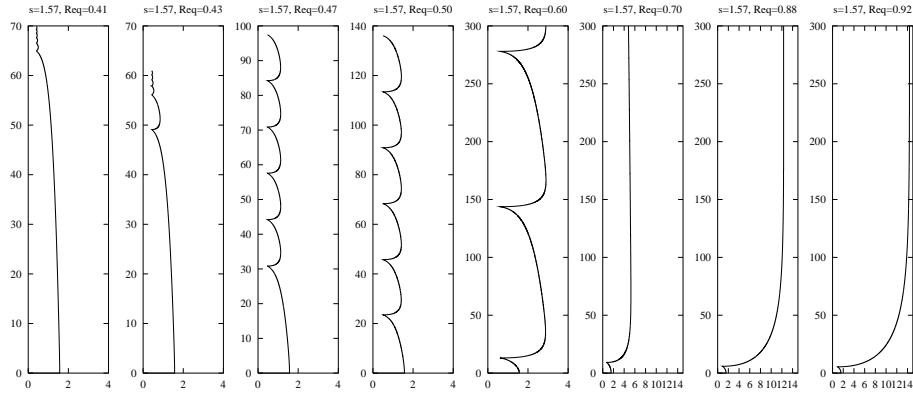


FIGURE 6.14: Results of the model for several bubble sizes for $s_i = 1.57$ mm. The multiple bounces for the medium sized bubbles is found. But unlike the experiments small bubbles appear to slip and reappearance of multiple bounces has not been observed.

For the bubbles of 0.6 mm the amplitude is accurately predicted, but the model always shows multiple bounces with large bounds lengths, whereas the experiments show bouncing followed by separation. The long bounds length do indicate that there is a tendency towards separation. However, in the model, the attraction force might become very small for large separations, but will never become zero. Physically, this attraction force cannot vanish in the model and thus multiple bounces are to be expected. It will be shown below that a possible explanation for these differences is the misalignment of the wall.

In Figure 6.14 the initial distance is increased to $s_i = 1.57$ mm, the distance at which most experiments have been performed. Note the qualitatively good agreement between the results of the model and the experimental results presented in Figures 6.3 and 6.5. The same critical Weber number $We_{cr} = 0.165$ as was determined for the previous initial distance ($s_i = 1.16$ mm) was used.

The behaviour of the smallest bubbles (0.41 and 0.43 mm) is very different from what was observed experimentally. Experimentally the bubble did not collide against the wall and in the model the bubble collides and subsequently slides along the wall. Again, a small misalignment of the wall can explain these discrepancies (see § 4.4).

For the slightly larger bubbles the bouncing behaviour is reproduced, but again the amplitude and the bounce length are underestimated. The bouncing separation behaviour for $r_{eq} = 0.50 - 0.70$ mm is not reproduced, but can be shown to occur when a misalignment of the wall is included. The reappearance of the multiple bounces in the experiments for $r_{eq} > 0.80$ mm is not predicted by the model. However, from the experiments it is known that the wake consists of a double-threaded wake. It is also shown that the threads are aligned corresponding to a lift force that is

an attraction force. This is not included in the model.

On the basis of simple mechanics the most logical shape of the bounces would be symmetrical. However, in the experiments an almost horizontal separation after bouncing and a curved approach just before bouncing is observed; the shape of the bounds looks like a profile of a nose. Note that, in spite of some shortcomings of the model, there is a similarity between these 'nose-like' shapes of the rebounds in the model and that of the experiments. The model does predict several features, e.g. the transition between sliding and bouncing motion, the increase of bounce amplitude and the shape of the bounds. But the model is not able to predict the bouncing separation, the bounds amplitude and length, and the reappearance of multiple bounces with short bound length for very large bubbles. In the following, these features are addressed and the model is adapted.

4.4 Adaptions to the model: misalignment and lift

The model including the bouncing criterion can explain several aspects of the bouncing. Here we adapt it further to take into account the vertical misalignment of the wall and the effect of the lift force on the bubble.

First we will introduce the misalignment of the wall. In the model this can be included by setting the direction of gravity at an angle α with the wall. Now there is a component of the buoyancy force along the wall and a component perpendicular to the wall. The latter will act as a repulsion force on the bubble. The external forces F_x and F_y in the equations of motion (6.1) now become

$$F_y = 2\rho gV \cos \alpha - D_y, \quad (6.8)$$

$$F_x = 2\rho gV \sin \alpha - D_x. \quad (6.9)$$

The experimental accuracy of the alignment of the wall is $\pm 0.2^\circ$. For an angle of $\alpha = 0.1$ degrees the results of the model for the initial separation of $s_i = 1.57$ mm are shown in figure 6.15. Especially for the small and medium sized bubbles (0.40-0.80mm) the effect is qualitatively in a closer agreement with the experimentally observed bouncing behaviour (Figure 6.3). The bound amplitudes are reproduced very well, but the bound lengths are not. The bouncing separation is reproduced, but for the experiments this already occurs for a bubble $r_{eq} = 0.50$ mm, whereas in the model a bubble of this size is found to perform multiple bounces. Next to the bouncing separation also the behaviour for $r_{eq} = 0.41$ and 0.43 mm is captured. The bubbles of these sizes were observed never to bounce against the wall. However, for larger bubbles the reappearance of the multiple bounces is not captured. This is not remarkable as we expect these to be related to the lift force.

This lift force needs to be taken into account only for bubbles which perform spiralling and zigzagging motions when free rising. For pure water held at 20° C this means that the lift force plays a role for bubbles with an equivalent radius larger than

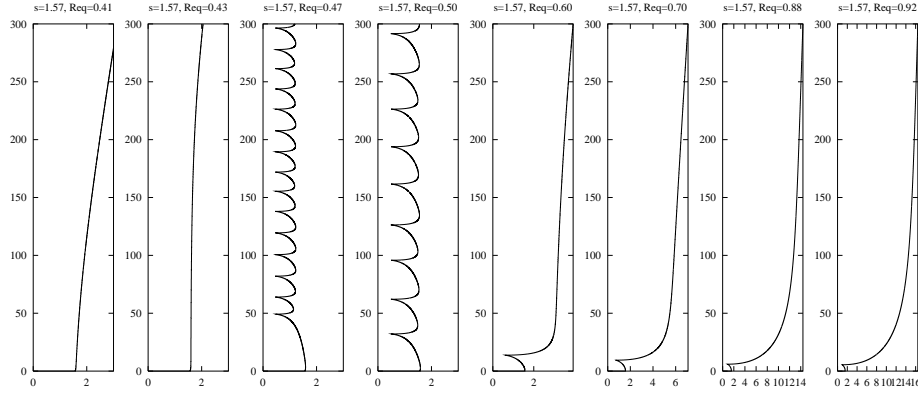


FIGURE 6.15: Results of model for $s_i = 1.57$ mm and an angle 0.1 degree of the wall with respect to the vertical. Up to about 0.80 mm the behaviour of the bubbles is qualitatively in agreement with the experiments. For larger bubbles the reappearance of multiple bounces, as observed in the experiments, was not captured.

0.80 mm. For these bubbles the lift force should be included in the external forces, which components then become:

$$F_y = 2\rho gV \cos \alpha + 2L \cos \beta - D_y, \quad (6.10)$$

$$F_x = 2\rho gV \sin \alpha - 2L \sin \beta - D_x, \quad (6.11)$$

where β is the angle of the path with the horizontal. The factors two arise from the fact that the forces act on the bubble pair. The lift force is estimated by $L \approx \pi\rho U_T^2 r_{eq}^2 / 13$ (see equation (4.9), with $U_f \approx 0.1U_T$ and $l \approx 0.6r_{eq}$). The results for the model taking into account the bouncing criterion, the misalignment of the wall ($\alpha = 0.1$ degrees) and the lift force are given in Figure 6.16 for $s_i = 1.57$ mm. These results should be compared with the experimental results presented in Figure 6.5. Qualitatively the results are in agreement. The reappearance of the multiple bounces and the bounce height are predicted, however the bounce lengths cannot be reproduced accurately.

One other aspect neglected in this model which might play a very important role for large bubbles is the shape. This will change the drag and the added mass significantly. It can be shown that the drag will increase and thus the velocity magnitude will decrease. The lift force is proportional to the square of the velocity magnitude and will decrease. As a result the bounce height and length are expected to be larger when shape effects are taken into account.

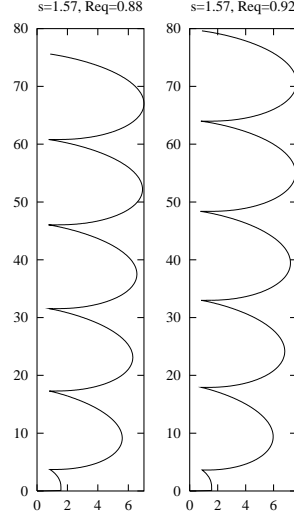


FIGURE 6.16: Results of model for large bubbles with a wake induced lift force at $s_i = 1.57$ mm and an angle=0.1 degrees. The reappearance of multiple bounces is captured.

5 Vortex and bubble near wall

Before the bounce, there is accumulation of vorticity in the wake of the rising bubble. Due to the encounter with another bubble, or in this case, the wall, vorticity from the wake is released (Figure 6.7). The effect of this vorticity on the motion of the bubble is checked below. However this force will only be important just after bouncing.

The amount of vorticity that is being left behind can be estimated by calculating,

$$\int \int \int_{\theta=\frac{\pi}{2}}^{\pi} \omega dV \quad (6.12)$$

over the boundary layer of thickness $\mathcal{O}(Re^{-1/2})$ at the rear part of the bubble. We take ω as the vorticity (see 2.10) at the rear of the bubble,

$$\omega = -\frac{3U_T \sin \theta}{r_{eq}} \operatorname{erfc} \left(\frac{3y \sin \theta}{4\sqrt{2}} \right). \quad (6.13)$$

Using this we obtain

$$\int \int \int \omega dV = 4\sqrt{2}\pi^2 \sqrt{\frac{1}{Re}} r_{eq}^2 U_T. \quad (6.14)$$

Now we assume that this amount of vorticity is shed instantaneously and comprised in a vortex blob represented as a Hill's Spherical Vortex (HSV) with radius r_{eq} . This

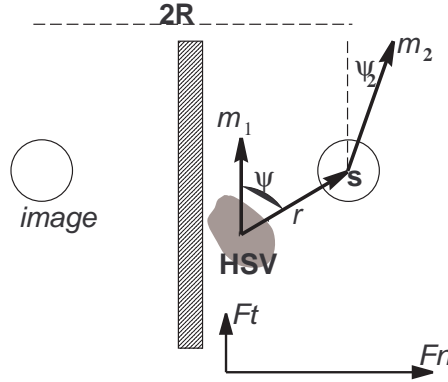


FIGURE 6.17: Coordinate system bubble and vortical blob

vortex is (Saffman 1992) characterised by

$$\begin{aligned}\omega_\theta &= \omega = 0, & \text{outside HSV, } r > r_{eq}, \\ \omega &= Ar, & \text{inside HSV, } r \leq r_{eq}.\end{aligned}\quad (6.15)$$

The coefficient A is determined in such a way that the total amount of vorticity inside the HSV equals the amount of vorticity shed by the bubble

$$\int_{\text{HSV}} A r d v = 4\sqrt{2}\pi^2 \sqrt{\frac{1}{Re}} r_{eq}^2 U_T. \quad (6.16)$$

The result for A is

$$A = 16\sqrt{\frac{2\nu U_T}{r_{eq}^5}}. \quad (6.17)$$

The flow outside the HSV can be modelled as a potential flow due to a sphere moving with velocity U_H ,

$$U_H = \frac{2r_{eq}^2 A}{15}. \quad (6.18)$$

For the vortical region formed at bouncing of a $r_{eq} = 0.85$ mm bubble (Figure 6.7) this would result in a velocity $U_H \approx 5.7$ cm/s. From the measurements $U_H \approx 6$ cm/s is retrieved, which is in good agreement.

The system of bubble and HSV can be described by a system of two dipoles, with strength \mathbf{m}_2 and \mathbf{m}_1 , respectively. The potential Φ of the HSV induces a velocity on the bubble. The resultant force is dependent on both the angle (ψ) and distance (s) of the bubble to the HSV and the angle (ψ_2) of the direction of the motion of the bubble. The force on the bubble by the HSV is,

$$\mathbf{F} = -4\pi\nabla\mathbf{m}_2 \cdot \nabla\Phi \quad (6.19)$$

$$\text{with} \quad \mathbf{m}_2 \cdot \nabla\Phi = -\frac{\mathbf{m}_1 \cdot \mathbf{m}_2}{r^3} + 3\frac{(\mathbf{m}_1 \cdot \mathbf{r})(\mathbf{m}_2 \cdot \mathbf{r})}{r^5} \quad (6.20)$$

The component normal to the wall of this force, the attraction force, and the tangential component for a bubble in s become

$$F_n = \frac{12\pi m_1 m_2}{r^4} \left(-\sin \psi \cos \psi_2 + 4 \sin \psi \cos \psi \cos(-\psi + \psi_2) - \cos^2 \psi \sin(-\psi + \psi_2) \right), \quad (6.21)$$

$$F_t = \frac{12\pi m_1 m_2}{r^4} \left(\cos(-\psi + \psi_2) + 2 \cos^2 \psi \cos(-\psi + \psi_2) - \sin \psi \cos \psi \sin(-\psi + \psi_2) - \cos \psi \cos \psi_2 \right), \quad (6.22)$$

respectively. The vertical velocity of the bubble will quickly increase the distance between the bubble and the HSV. Therefore the force is negligible except just after bouncing. From the experiments (Figure 6.8e) it looks as if at that moment $\psi = 90^\circ$ and $\psi_2 = 0^\circ$. Although the vortical blob is not fully developed, the attraction force will be of the same order of magnitude. At that time the total force is attractive with a negligible vertical component. The magnitude of the attraction force, associated with the vortical blob, is comparable to the maximum of the attraction force of the image bubble. This can explain the reduction of horizontal velocity or even the negative horizontal velocity as for example observed in Figure 6.6. However, the subsequent increase of the horizontal distance to the wall cannot be explained.

The exact values of the force on the bubble due to the vortical blob cannot be given. This force only has significant values as long as the distance between the bubble and the vortical blob is very small. During this time the vortical blob is still developing. Assuming the vortical blob is instantaneously formed the magnitude of this force is up to 20 times the attraction force by the mirror bubble.

However, we did not take this force into account in the model as the influence of this force is limited to the first milliseconds after bouncing. It might even be that this force is the reason for the velocity drop in the vertical direction at bouncing. Then this force is already included in the assumed instantaneous drop in velocity.

6 Discussion and conclusions

Bouncing phenomena can be approximately described by a model based upon potential flow, taking into account bouncing criteria and wake effects. The larger bounce amplitude than the initial distance to the wall can be explained with this model. The attraction force of a bouncing bubble reduces significantly as the bubble vertical velocity component drops. At bouncing the horizontal momentum is conserved. The combination of both makes a larger bounce possible or can compensate for the energy loss by dissipation.

One of the questions still remaining is the slowing down of the bubble after bouncing. At present it is assumed that the wake of the bubble and its vorticity, first pushes itself in between the wall and the bubble. The further development of the wake shows a down-flow region near the bubble, which is probably causing the bubble to slow down. Furthermore, the vortical blob formed will have an attraction force, being able to hold the bubble near the wall. This force quickly drops to zero as the distance between the bubble and vortical blob increases. But the subsequent increase in horizontal distance to the wall cannot be explained.

It is observed that as soon as ellipsoidal bubbles hit the wall they immediately become spherical. More research is needed to estimate the effects of deformation on the bouncing phenomena, especially for the large bubbles. Although the lift force related to the wake can explain the rebounds and the amplitude of the bounce, the path of the bouncing bubble can not be reproduced accurately for the large bubbles.

PSEUDO-TURBULENCE IN BUBBLY FLOWS



Bubbles rising in turbulent flows will affect this flow and introduce velocity fluctuations. This phenomenon is called “pseudo-turbulence”. Following the first tentative explanation of van Wijngaarden (1998) based on potential flow theory around non-spherical bubbles with thin boundary layers, we model Hill’s Spherical Vortices as an extra source of turbulence. These vortices are assumed to be shed from the rising bubbles ‘hitting’ turbulent regions in a similar way as observed in our experiments on a bubble bouncing against a vertical wall. A significant contribution of these vortices is observed. Furthermore this model is extended to take into account the effects of the rearrangement of vorticity in the wake of the bubble.

1 Introduction

In bubbly flows there is a two-way coupling between bubbles and turbulence. Turbulence affects the trajectories of the bubbles and bubble motion introduces velocity fluctuations, and therefore Reynolds stresses, in the liquid. This process is called pseudo-turbulence. The term turbulence refers to the fluctuating character of the flow, the term “pseudo” indicates that the origin of the turbulence is an induced motion by the bubbles.

The importance of pseudo-turbulence is emphasised by experiments of Lance & Bataille (1991; hereinafter referred to as LB) and Theofanous & Sullivan (1982; referred to as TS). An indicator is the extra turbulent energy arising from the bubbles,

$$\overline{\mathbf{u}'_E'^2} = \overline{\mathbf{u}'^2} - \overline{\mathbf{u}'_0'^2}, \quad (7.1)$$

where \mathbf{u}' represents the measured turbulent velocity fluctuations and \mathbf{u}'_0 is the corresponding value in the absence of bubbles. A first tentative explanation of this phenomenon was presented by van Wijngaarden (1998; hereinafter referred to as LvW), which was based on the rise of isolated bubbles, whereby the flow around the bubble is described with potential flow theory coupled with thin boundary layers. The

turbulent excess energy was found to be,

$$\overline{\mathbf{u}_E'^2} = \alpha_B U_T^2 \left[1 + 12 \frac{\overline{\mathbf{u}_0'^2}}{U_T^2} \right] \quad (7.2)$$

with $\alpha_B = \frac{4}{3}\pi r_{eq}^3 n$ the void fraction of bubbles, n the number density, r_{eq} the equivalent bubble radius and U_T the terminal rise velocity of the bubbles. In experiments, however, a much steeper rise of $\overline{\mathbf{u}_E'^2}$ with α_B , for a given turbulence level, is measured (Figure 7.2).

The aim of the present research is to incorporate vorticity effects. In this chapter, vorticity rearranged as Hill's spherical vortices (HSV) in the wake of bubbles is proposed as an extra source of turbulent excess energy. This model is based on our observation of vortex blob formation for bubbles bouncing against a vertical wall (Chapter 5).

2 Volume fraction of Hill's spherical vortices

The amount of vorticity on a spherical bubble can be estimated by $\Omega = \int \omega dV = 4\sqrt{2}\pi^2 \sqrt{\frac{1}{Re}} r_{eq}^2 U_T$ (6.14), where the integration is over the volume of the boundary layer. The vorticity production is even larger for non-spherical bubbles.

As a first estimate the vorticity advected in the wake of the bubble is neglected and an HSV is formed at every sudden acceleration of the bubble. Or in other words, an HSV is formed each time a bubble 'hits' a turbulent eddy. A similar HSV will be formed as observed for the bouncing bubbles (6.18): $U_H = 2r_{eq}^2 A/15 \approx 0.2U_T$ with $A = 16\sqrt{2\nu U_T/r_{eq}^5}$. The flow outside the HSV is equivalent to the potential flow due to a solid sphere moving with velocity U_H .

It is hard to estimate the number of vortex blobs produced in this way per unit time. An upper limit is found by considering that before another blob can be formed, vorticity has to be generated at the bubble surface again. The time needed for this is of the order $2r_{eq}/U_T$, so that each bubble produces at most $U_T/2r_{eq}$ blobs per unit time. For the bubbles discussed in this thesis this is of the order of a few hundred Hz.

A lower limit is obtained by considering bubbles that have zigzagging trajectories when freely rising. Since they are, in this model, supposed to form a vortical blob, accumulated at the rear, each time the path curvature changes sign, a lower bound is twice the natural frequency of the path of a free rising bubble. In the present experiments this frequency is: 4.5 Hz for bubbles of $r_{eq} = 0.80$ mm and 6.5 Hz for $r_{eq} = 1.1$ mm. In this chapter comparison is made with experiments for bubble sizes of $r_{eq} = 1.5$ mm. The lower bound for the frequency of shedding is then $f \approx 14$ Hz.

In this research the interest is in determining whether these HSV may play an important role, and thus the lower bound of HSV production is taken. The number

of vortex blobs produced in a unit volume of the flow per unit time is nf . The vortex blobs are dissipated by viscous diffusion, their lifetime can be estimated therefore as $r_{eq}^2/4\nu$. N denotes the number density of vortex blobs, to be represented as HSVs, the growth of N per unit time, with initial condition ($t = 0, N = 0$) is

$$\frac{dN}{dt} = nf - \frac{4N\nu}{r_{eq}^2}, \quad N = \frac{r_{eq}^2}{4\nu} \left(1 - e^{-4\nu t/r_{eq}^2}\right) nf. \quad (7.3)$$

Hence the equilibrium number density of HSVs is $N = nf r_{eq}^2/4\nu$. For $r_{eq} = 1.5$ mm and $\nu = 10^{-6}$ m²/s we get $N \approx 0.56nf$ and the corresponding volume fraction of the HSVs is,

$$\alpha_H \approx 8\alpha_B. \quad (7.4)$$

The value obtained for α_H with the upper bound $2r_{eq}/U_T$ for the frequency of vortical blob generation is about $50\alpha_B$ (for $U_T=0.3$ m/s). This is well above the estimate given in (7.4).

Note that although the void fractions are small and bubble-bubble interactions (α_B^2 terms) can be neglected, we should not neglect beforehand bubble-HSV interactions ($\alpha_B\alpha_H$ terms) as a bubble will interact with the HSVs shed by previous bubbles.

3 Turbulent excess energy

The excess turbulent energy is calculated following the method and notation of LvW. The coordinate system is defined in Figure 7.1. In the derivation the subscript B is used for the bubble terms and H for HSV terms, P denotes the probability density. $P_B(\mathbf{r})d^3\mathbf{r}$ denotes the probability of finding a bubble centre in the volume $d^3\mathbf{r}$ around \mathbf{r} . Similarly $P_H(\mathbf{y})d^3\mathbf{y}$ denotes the probability of finding an HSV centre in a volume $d^3\mathbf{y}$ centred around \mathbf{y} . Furthermore, a is used as the equivalent radius of the bubble and the HSV. The velocity, induced at \mathbf{x} by a bubble at $\mathbf{x} + \mathbf{r}$ and under the influence of an HSV at $\mathbf{x} + \mathbf{y}$ is indicated with \mathbf{q}_B^* . The velocity induced at \mathbf{x} by an HSV at $\mathbf{x} + \mathbf{y}$, by \mathbf{q}_H^* . Consequently the total velocity fluctuation in \mathbf{x} can be written as,

$$\mathbf{u}'(\mathbf{x}) = \mathbf{u}'_0(\mathbf{x}) + \mathbf{q}_B^*(\mathbf{x}, \mathbf{x} + \mathbf{r}, \mathbf{x} + \mathbf{y}) + \mathbf{q}_H^*(\mathbf{x}, \mathbf{x} + \mathbf{y}). \quad (7.5)$$

Averaging over all possible values of \mathbf{r} and \mathbf{y} gives

$$\mathbf{q}_B(\mathbf{x}) = \int_{r>a} \int_{\text{all } \mathbf{y}} \mathbf{q}_B^* P_B(\mathbf{x} + \mathbf{r}) P_H(\mathbf{x} + \mathbf{y}) d^3\mathbf{r} d^3\mathbf{y}. \quad (7.6)$$

\mathbf{q}_B^* can be derived from a potential ϕ_B . Restricting ourselves to dipoles the potential of the bubble for dilute mixtures can be written as

$$\phi_B = -\frac{[\mathbf{v}_{rel} a^3] \cdot \mathbf{r}}{2r^3}, \quad (7.7)$$

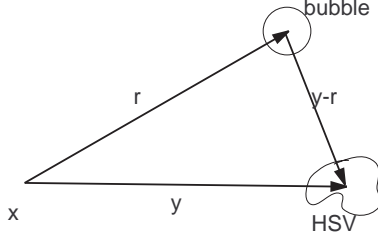


FIGURE 7.1: A bubble in $\mathbf{x}+\mathbf{r}$ and an HSV in $\mathbf{x}+\mathbf{y}$ inducing velocity fluctuations in \mathbf{x}

where \mathbf{v}_{rel} , the relative velocity of the bubble, can be written as

$$\mathbf{v}_{rel} = U_T \mathbf{k} + 2\mathbf{u}'_0 + 2\mathbf{q}_H^*, \quad (7.8)$$

with \mathbf{k} the unit vector in the vertical direction. Now we insert (7.8) in (7.7) and in evaluating $\mathbf{q}_B^* = \nabla\phi_B$ we distinguish between the direct contributions of bubbles to $\mathbf{q}_B(\mathbf{x})$, \mathbf{q}_{BB} , and the contributions from the HSV through the bubbles, \mathbf{q}_{BH} . In a similar fashion we define $\mathbf{q}_{BB} = \nabla\phi_{BB}$ and $\mathbf{q}_{BH} = \nabla\phi_{BH}$. Then $\mathbf{q}_B(\mathbf{x})$ in (7.6) can be written as

$$\begin{aligned} \mathbf{q}_B(\mathbf{x}) &= \mathbf{q}_{BB}(\mathbf{x}) + \mathbf{q}_{BH}(\mathbf{x}) \\ &= \int_{r>a} -\frac{(U_T \mathbf{k} + 2\mathbf{u}'_0)a^3}{2r^3} + \frac{3a^3(U_T \mathbf{k} + 2\mathbf{u}'_0) \cdot \mathbf{r}}{2r^5} \mathbf{r} P_B d^3 \mathbf{r} \\ &\quad + \int_{r>a} \int_{\mathbf{y}} -\frac{\mathbf{q}_H^*(\mathbf{y} - \mathbf{r})a^3}{r^3} + \frac{3a^3 \mathbf{q}_H^*(\mathbf{y} - \mathbf{r}) \cdot \mathbf{r}}{r^5} \mathbf{r} P_B P_H d^3 \mathbf{r} d^3 \mathbf{y} \end{aligned} \quad (7.9)$$

Turning to \mathbf{q}_H^* , we observe that this is given inside the HSV by a stream function $\bar{\psi}_H = \psi_H \mathbf{k}$, and outside by a potential $\phi_H = -\frac{a^3 U_H \mathbf{k} \cdot \mathbf{y}}{2y^3}$. Similar to \mathbf{q}_B we define,

$$\mathbf{q}_H(\mathbf{x}) = \int \mathbf{q}_H^* P_H d^3 \mathbf{y} = \int_{y \leq a} \nabla \times \bar{\psi}_H P_H(\mathbf{x} + \mathbf{y}) d^3 \mathbf{y} + \int_{y > a} \nabla \phi_H P_H(\mathbf{x} + \mathbf{y}) d^3 \mathbf{y} \quad (7.10)$$

Subsequently, twice the average energy in the fluctuations can be written as, $\langle \rangle$ denoting time averaging,

$$\begin{aligned} \langle \mathbf{u}' \cdot \mathbf{u}' \rangle &= \langle \mathbf{u}'_0 \cdot \mathbf{u}'_0 \rangle + 2 \langle \mathbf{u}'_0 \cdot \mathbf{q}_B \rangle + 2 \langle \mathbf{u}'_0 \cdot \mathbf{q}_H \rangle + \langle \mathbf{q}_B \cdot \mathbf{q}_B \rangle \\ &\quad + 2 \langle \mathbf{q}_B \cdot \mathbf{q}_H \rangle + \langle \mathbf{q}_H \cdot \mathbf{q}_H \rangle = A + B + C + D + E + F. \end{aligned} \quad (7.11)$$

The excess turbulent energy is defined as $\frac{1}{2}[\langle \mathbf{u}' \cdot \mathbf{u}' \rangle - \langle \mathbf{u}'_0 \cdot \mathbf{u}'_0 \rangle]$. As a result A does not need to be calculated. All terms will be rewritten in terms involving only the bubble terms or HSV terms in order to make use of the results of LvW.

$$\begin{aligned} B &= 2 \langle \mathbf{u}'_0 \cdot \mathbf{q}_B \rangle = 2 \langle \mathbf{u}'_0 \cdot \mathbf{q}_{BB} \rangle + 2 \langle \mathbf{u}'_0 \cdot \mathbf{q}_{BH} \rangle \\ &= E_1 \text{ (see LvW)} + 2 \langle \mathbf{u}'_0 \cdot \mathbf{q}_{BH} \rangle \end{aligned} \quad (7.12)$$

The last term in (7.12) is zero because there is no correlation between the HSV and the turbulence. In a similar way it can be proven that

$$C = \langle \mathbf{u}'_0 \cdot \mathbf{q}_H \rangle = 0. \quad (7.13)$$

D is solved using LvW, including the velocity induced by the HSV on the bubble.

$$\begin{aligned} D &= \langle \mathbf{q}_B \cdot \mathbf{q}_B \rangle = \langle \mathbf{q}_{BB} \cdot \mathbf{q}_{BB} \rangle + 2 \langle \mathbf{q}_{BB} \cdot \mathbf{q}_{BH} \rangle + \langle \mathbf{q}_{BH} \cdot \mathbf{q}_{BH} \rangle \\ &= E_2 \text{ (see LvW)} + 2 \langle \mathbf{q}_{BB} \cdot \mathbf{q}_{BH} \rangle + \langle \mathbf{q}_{BH} \cdot \mathbf{q}_{BH} \rangle. \end{aligned} \quad (7.14)$$

The third term on the right hand side of the of the last line in Equation (7.14), i.e. the effect of a velocity of the HSV through the bubble, is much smaller than the direct effect of the HSV in \mathbf{x} and can be neglected. Additionally, $U_H \approx 0.2U_T$ and so the second term is always much larger than the third. An extra effect which decreases the influence of the HSV in the third term is that the distance from the HSV to the bubble and then to the point, is always larger than the direct distance from the bubble to the point. The second term, however, has to be estimated, which is done as follows. The probability of finding an HSV in $\mathbf{x} + \mathbf{y}$, being a bubble in $\mathbf{x} + \mathbf{r}$ is, assuming the probabilities to be uncorrelated,

$$P(\mathbf{x} + \mathbf{y}, \mathbf{x} + \mathbf{r}) = \begin{cases} P_B(\mathbf{x} + \mathbf{r})P_H(\mathbf{x} + \mathbf{y}) = P_B P_H & |\mathbf{y} - \mathbf{r}| \geq 2a \\ 0 & |\mathbf{y} - \mathbf{r}| < 2a \end{cases}. \quad (7.15)$$

Then

$$\langle \mathbf{q}_{BB} \cdot \mathbf{q}_{BH} \rangle = \int \int \langle \nabla_r \phi_{BB} \cdot \nabla_r \phi_{BH} \rangle P_B P_H d^3 \mathbf{r} d^3 \mathbf{y} \quad (7.16)$$

$$= \int \int \left\langle \nabla_r \phi_{BB} \cdot \left[-\frac{a^3 \nabla_{(\mathbf{y}-\mathbf{r})} \phi_H}{r^3} + \frac{3a^3 \nabla_{(\mathbf{y}-\mathbf{r})} \phi_H \cdot \mathbf{r}}{r^5} \right] \right\rangle P_B P_H d^3 \mathbf{r} d^3 \mathbf{y}. \quad (7.17)$$

All terms are of the same order. Therefore we make an estimate of the first term, resulting in

$$\begin{aligned} \langle \mathbf{q}_{BB} \cdot \mathbf{q}_{BH} \rangle &\approx \int \int \left\langle \nabla_r \phi_{BB} \cdot -\frac{a^3 \nabla_{\mathbf{y}} \phi_H}{r^3} \right\rangle P_B P_H d^3 \mathbf{r} d^3 \mathbf{y} \\ &= a^3 \int_{r>a} d^3 \mathbf{r} \frac{P_B(\mathbf{x} + \mathbf{r}) \nabla \phi_{BB}(\mathbf{r})}{r^3} \cdot \int_{\mathbf{y}} d^3(\mathbf{y}) \nabla \phi_H(\mathbf{y}) P_H(\mathbf{x} + \mathbf{y}). \end{aligned}$$

The last integral is not uniformly convergent. To overcome this difficulty the technique proposed by Batchelor (1972), and used in bubble dynamics by van Wijngaarden (1976), is used. This technique is based on the fact that the averaged effect of bubbles, and thus of the HSV, on the mass flux should be zero. This means

$$\int_{\text{all configurations}} \mathbf{u}_H d^3 \mathbf{y} = 0, \quad \text{or} \quad (7.18)$$

$$\int_{0 < y \leq a} \mathbf{u}_H d^3 \mathbf{y} + \int_{a < y \leq 2a} \mathbf{u}_H d^3 \mathbf{y} + \int_{y > 2a} \mathbf{u}_H d^3 \mathbf{y} = 0 \quad (7.19)$$

The HSV vortices move with a velocity, $U_H \mathbf{k}$, and their concentration by volume is, α_H , so the first integral on the left hand side of (7.19) is equal to $\alpha_H U_H \mathbf{k}$. The second and third integrals are zero and equation (7.18) becomes

$$\begin{aligned}
\langle \mathbf{q}_{BB} \cdot \mathbf{q}_{BH} \rangle &\approx -\alpha_H a^3 U_H \mathbf{k} \cdot \int \frac{\nabla \phi_{BB}}{r^3} P_B d^3 \mathbf{r} \\
&= -\alpha_H a^3 U_H \mathbf{k} \cdot \left(n \int \nabla \left(\frac{\phi_{BB}}{r^3} \right) d^3 \mathbf{r} + 3n \int \frac{\phi_{BB}}{r^4} \frac{\mathbf{r}}{r} d^3 \mathbf{r} \right) \\
&= -\alpha_H U_H n a^3 \left[-\frac{20}{9} \pi U_T + \frac{4}{3} U_T \right] \\
&= \frac{2}{3} \alpha_B \alpha_H U_H U_T \approx \alpha_B^2 U_T^2 = \mathcal{O}(\alpha_B^2)
\end{aligned} \tag{7.20}$$

which can be neglected because α_B^2 is a bubble interaction term which is also neglected. Since all other neglected terms are of order α_B^2 , term D becomes

$$D \approx E_2 \text{ (see LvW)} + \mathcal{O}(\alpha_B^2) \approx E_2 \tag{7.21}$$

Likewise,

$$E = 2 \langle \mathbf{q}_B \mathbf{q}_H \rangle = 2 \int \int \nabla \phi_{BB} \cdot n_H \nabla \phi_H d^3 \mathbf{r} d^3 \mathbf{y} = \mathcal{O}(\alpha_B^2) \tag{7.22}$$

Up to now all parts including effects of the HSV could be neglected and only the effects already determined by LvW remain. Finally the term F , describing the energy of the HSVs, has to be determined. Using the results of Synge & Lin (1943),

$$F = \langle \mathbf{q}_H \mathbf{q}_H \rangle = n_H \frac{10}{7} \pi a^3 U_H^2 \approx \alpha_H U_H^2 \approx 0.35 \alpha_B U_T^2, \tag{7.23}$$

where we used $U_H = 0.2 U_T$ and $\alpha_H = 8 \alpha_B$. In conclusion it appears that only the energy of the HSV and the effects already given by van Wijngaarden (1998) have to be taken into account. The excess turbulent energy finally becomes,

$$\overline{\mathbf{u}_E'^2} = \alpha_B U_T^2 \left[1.35 + 12 \frac{\mathbf{u}_0'^2}{U_T^2} \right] \text{ as lower bound} \tag{7.24}$$

This lower bound is larger than the result obtained in LvW and closer to the experimental lines.

For the size of bubbles used in the above analysis, a double threaded wake is observed for free rising bubbles in quiescent water (Chapter 4). As this double thread is shown to become unstable on short time scales for large perturbations, a similar behaviour is expected in turbulence. In principle all the vorticity produced on the bubbles is transported in the wake and will affect the turbulence. If all the vorticity

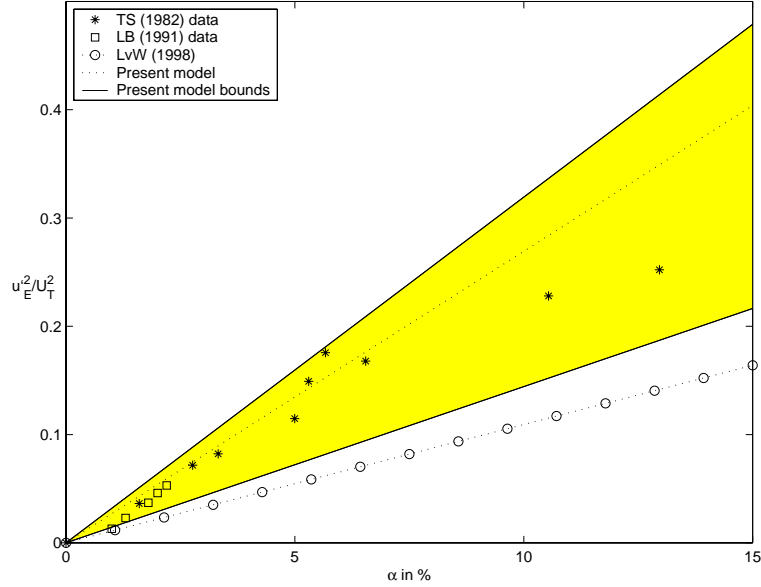


FIGURE 7.2: *Excess turbulent energy vs void fraction: Experiments of Theofanous & Sullivan (1982) for $\overline{u'_0}/\overline{U_T} = 0.088$ and Lance & Bataille (1991) for $\overline{u'_0}/\overline{U_T} = 0.085$. The grey area indicates the range of the present model, bounds defined by (7.24) and (7.25). The dashed line indicates the result of the present model, based on the wavelength of the instability (7.26)*

in the wake is rearranged into HSVs and the strength and size of the HSVs are as described above. Then the volume fraction of HSVs can grow up to $50\alpha_B$, which is the upper bound.

Although many assumptions made in the model are no longer valid for these large volume fractions of HSVs, a good approximation for the excess turbulent energy can be given by just taking into account the energy of the HSVs and the terms already obtained by van Wijngaarden (1998). The upper bound for the excess turbulent energy is approximately

$$\overline{u_E'^2} = \alpha_B U_T^2 \left[3.1 + 12 \frac{u_0'^2}{U_T^2} \right] \quad \text{as upper bound.} \quad (7.25)$$

It is hypothesised here that a good measure of the volume fraction of HSVs can be obtained from the wavelength of the instabilities observed in the wake. In Chapter 4 it is observed that for a free rising zigzagging bubble the wavelength of the Crow instability was about $5b \approx 3r_{eq}$. With a rise velocity of 30 cm/s and $r_{eq} = 1.5$ mm, the frequency of the ‘‘Crow’’ instability would be $f = 0.30/0.0045 = 67$ Hz. Then the volume fraction of HSVs would become about $40\alpha_B$. The excess turbulent

energy then becomes

$$\overline{\mathbf{u}_E'^2} = \alpha_B U_T^2 \left[2.6 + 12 \frac{\mathbf{u}_0'^2}{U_T^2} \right] \quad \text{as present model,} \quad (7.26)$$

which is in very good agreement with the experimentally observed values.

4 Conclusions

The present analysis shows the considerable effect of vorticity generated by the bubbles on the excess turbulent energy. The experimental results of Lance & Bataille (1991) and Theofanous & Sullivan (1982) are within the upper and lower bound of the model (Figure 7.2). The lower bound of this model is given by the natural frequency of a single rising bubble in quiescent water. The upper bound is given by the maximum amount of vorticity produced on the surface of the bubble in quiescent water.

In the model the vorticity is concentrated in Hill's spherical vortices. Admittedly, this is not necessarily so in the real situation. Therefore more research has to be performed to determine a better estimate of the produced vorticity distribution. It is expected, however, that the excess energy will be of the same order of magnitude as estimated in the present analysis.

CONCLUSIONS AND RECOMMENDATIONS



The main purpose of this study was to gain more fundamental knowledge on bubble dynamics. In particular to understand the causes of the remarkable disagreements between previous experimental results on the type of motions observed for path-unstable bubbles. The expectation was that the path of the bubble is strongly correlated with the wake behind the bubble. The latter is obviously correlated to the shape of the bubble and the purity of the water. The main problem was to visualise the wake without affecting the purity of the water.

A further fundamental question was how the path of bubbles bouncing against a vertical wall can be explained. The hypothesis was that there is again a strong correlation between the wake and the observed motion. Also we wanted to investigate whether a bouncing criterion holds, similar to that occurring for a colliding bubble pair. In addition to these questions, we wanted to understand the motion of the bubbles by constructing a simplified, generic model. This model should capture the most important features of the motion.

The main experimental tool is the schlieren visualisation method which allows to visualise the wake without affecting the purity of the water. For free rising bubbles a double-threaded wake occurs when the curvature of the path is non-zero. This double-threaded wake is shown to exist of two counter-rotating vortex filaments. This results in a lift force affecting the path of the bubble. The different methods to indirectly determine the strength of this lift force agree perfectly.

The bubble-production technique used in the present experimental study is shown to have several advantages, e.g. the accuracy of the bubble size, the spherical shape at release and the large time between consecutive bubbles. The latter ensures that bubbles are not affected by preceding bubbles. This contrary to the, most widely used, conventional bubble-production method. Furthermore, the conventional bubble-production method triggers shape, or volume, oscillations of the bubble. To study the path instability of free rising bubbles all disturbances should be avoided.

It should be stressed that the onset of path instability cannot be triggered by an instability of the standing eddy, as is observed for solid spheres. In the region where path instability sets in, a standing eddy has not been observed experimentally or is expected numerically. At the front of the bubble the curvature of its surface is relatively small. This means that the stabilising effect of the surface tension is relatively small. One possibility is that an instability sets in and travels as a wave to the side of the bubble and then triggers the wake to become non-axisymmetric. The double-threaded wake is formed and sets in the non-rectilinear motion. Unfortunately we were not able to observe such a wave in any of our experiments.

The double-threaded wake ‘far’ behind the bubble becomes unstable. This instability is very similar to Crow instability. In general this is associated with the instabilities observed for the trailing vortices behind airplanes. As a result vortical regions are formed.

The zigzagging motions is not maintained by vortex shedding at the point at which the horizontal velocity component of the bubble switches sign, but is associated with the sign change of the lift force as soon as the bubble’s curvature changes sign. The latter coincides with the mean position of the zigzag. The curvature of the path becomes zero as the lift force is balanced by the component of the buoyancy force normal to the path.

The model explaining the path of bubble, based on a lift force directed towards the inward curvature of the path, gives qualitatively correct results. The lift force is zero for a zero curvature of the path. This also agrees with the experimental observations for a zigzagging bubble where a single-threaded wake is observed as soon as the curvature of the path is zero.

The experimentally observed interactions of bubbles bouncing against a vertical wall can be split into four types: i) sliding along the wall, ii) multiple bounces, iii) bouncing separations and iv) multiple bounces with large amplitudes.

The parameter determining the transition between the first two interaction types is a critical Weber number ($We_{cr} = 0.165$) based on the approach velocity. This is in good agreement with the critical Weber number ($We_{cr} = 0.18$) determined by Duineveld (1994), in his bubble-bubble interaction study, for the transition from coalescence to bouncing. In the present experiments it was observed that for bouncing bubbles (types ii-iv) the vertical velocity component drops drastically and the horizontal velocity component changed sign at bouncing. The explanation for the appearance of the large amplitude of the bounces is that the attraction force of the wall just after bouncing is reduced significantly compared to the force just before bouncing. The reason for this is that this attraction force is proportional to the velocity magnitude squared.

The parameter for the transition from the third to the fourth type of bouncing is the same as the parameter used for the occurrence of path instability for a free rising bubble, i.e. the Weber number based on the velocity magnitude. And thus the lift force is assumed to play a very important role. From the curvature of the path in the bouncing regime, it was shown that the lift force is always attractive, explaining the reappearance of the multiple bounces with very large amplitudes for larger bubbles.

The results of the bouncing model, based on the equations of motion for a bubble pair given in Kok (1993a), including a bouncing criterion, gives qualitatively results similar to those observed in the present experiments. The ‘nose-like’ shape of the bubble path during bouncing is reproduced and the bounce amplitudes were in good agreement. The shortcomings of the model became obvious for the large bubbles.

Clearly for these bubbles the assumption of a spherical shape is no longer valid.

The model for the modification of turbulence by bubbles gives promising results. The experimental results of Theofanous & Sullivan (1982) and Lance & Bataille (1991) for the excess turbulence energy fall in between of the lower and upper bounds of the model. For the lower bound the frequency of vortical regions is associated with the natural frequency of a zigzagging bubble. The frequency for the upper bound is associated with the rearrangement of all vorticity produced on the bubble into vortical regions.

Summarising these conclusions we can state that the bubble motion and the wake are strongly related. For large bubbles a lift force is observed. The main bouncing phenomena are understood. Based on the vorticity production on the bubble's surface good predictions of the modification of turbulence can be obtained.

Recommendations

One essential part not understood in bubble dynamics is the trigger of the path instability. We suggest the trigger is a perturbation of the shape at the front of the bubble, but no evidence can be given at this time.

The model predicts a horizontal displacement of the mean position, with respect to the release point, of both spiralling and zigzagging bubbles. It should be checked whether this indeed takes place.

Another remaining question is the orientation of the bubble. For the analysis it is sufficient to assume that the short axis is in the direction of motion. This orientation, however, is in contradiction with a curvature in the path. The bubble cannot be aligned in this way or the bubble has no longer a perfect ellipsoidal shape. Certainly detailed experiments studying the shape and orientation of the bubble are necessary. Furthermore, it would be interesting to theoretically estimate the necessary misalignment or deformation.

For the bouncing bubbles many questions remain, although the fundamental physics are understood. The main focus at this moment should be the cause of the drop in vertical velocity. We expect that a combination of the boundary layer, the wake effect and the shape of the bubble can explain the observed phenomena. Furthermore an attempt should be made to determine the added mass coefficients and drag coefficients for an ellipsoidal bubble pair. Especially for the larger bubbles this can have import effects.

The model for the modification of turbulence by incorporating vorticity reorientation is far from complete, but gives promising results. More research should be performed on determining more precisely the configuration of the vorticity distribution. Furthermore, more experiments should be performed giving more data to compare with. These experiments should cover a wider field, e.g. bubble radii and turbulence intensities.

REFERENCES

- ACHENBACH, E. 1974 Vortex shedding from spheres. *J. Fluid Mech.* **62**, 209–221.
- AYBERS, N.M. & TAPUCU, A. 1969a The motion of gas bubbles rising through stagnant liquid. *Wärme und Stoffübertragung* **2**, 118–128.
- AYBERS, N.M. & TAPUCU, A. 1969b Studies on the drag and shape of gas bubbles rising through a stagnant liquid. *Wärme und Stoffübertragung* **2**, 171–177.
- BATCHELOR, G.K. 1972 Sedimentation in a dilute dispersion of spheres. *J. Fluid Mech.* **52**, 245–268.
- BEL Fdhila, R. & DUINEVELD, P.C. 1996 The effect of surfactant on the rise of a spherical bubble at high Reynolds and Peclet numbers. *Phys. Fluids* **8**, 310–321.
- BENJAMIN, T.B. 1987 Hamiltonian theory for motions of bubbles in an infinite liquid. *J. Fluid Mech.* **181**, 349–379.
- BIESHEUVEL, A. 1984 On void fraction waves in dilute mixtures of liquid and gas bubbles. Ph.D. thesis, University of Twente.
- BIESHEUVEL, A. & VAN WIJNGAARDEN, L. 1982 The motion of pairs of gas bubbles in a perfect fluid. *J. Engng Maths* **4**, 349–365.
- BIESHEUVEL, A. & VAN WIJNGAARDEN, L. 1984 Two-phase flow equations for a dilute dispersion of gas bubbles in liquids. *J. Fluid Mech.* **148**, 301–318.
- BLANCO, A. & MAGNAUDET, J. 1995 The structure of the axisymmetric high-Reynolds number flow around an ellipsoidal bubble of fixed shape. *Phys. Fluids* **7**, 1265–1274.
- BRÜCKER, C. 1999 Structure and dynamics of the wake of bubbles and its relevance for bubble interaction. *Phys. Fluids* **11**, 1781–1796.
- BULTHUIS, H.F. 1997 Dynamics of bubbly flows. Ph.D. thesis, University of Twente.
- CLIFT, R., GRACE, J.R. & WEBER, M.E. 1978 *Bubbles, Drops, and Particles*. Academic Press Inc.
- CROW, S. C. 1970 Stability theory for a pair of trailing vortices. *AIAA J.* **8**, 2172–2179.
- DUINEVELD, P. C. 1994 Bouncing and coalescence of two bubbles in water. Ph.D. thesis, University of Twente.

- DUINEVELD, P.C. 1995 The rise velocity and shape of bubbles in pure water at high Reynolds number. *J. Fluid Mech.* **292**, 325–332.
- ELLINGSEN, K. 1998 Hydrodynamique des écoulements pilotés par l'ascension de bulles d'air virevolantes. Ph.D. thesis, Institute National Polytechnique de Toulouse.
- ELLINGSEN, K. & RISSO, F. 1998 Measurements of the flow field induced by the motion of a single bubble. *Proc. Third Int. Symp on Multiphase Flows*, Lyon.
- GRIGORIEV, I. S. & MEILIKHOV, E. Z. 1997 *Handbook of Physical Quantities*. CRC Press.
- HABERMAN, W.L. & MORTON, R.K. 1954 An experimental study of bubbles moving in liquids. *Trans ASCE* **2799**, 227–252.
- HARTUNIAN, R.A. & SEARS, W.R. 1957 On the instability of small gas bubbles moving uniformly in various liquids. *J. Fluid Mech.* **3**, 27–47.
- HECHT, E. 1974 *Optics*. Addison-Wesley.
- JOHNSON, T.A. & PATEL, V.C. 1999 Flow past a sphere up to a Reynolds number of 300. *J. Fluid Mech.* **378**, 19–70.
- KARAMANEV, D.G., CHAVARIE, C. & MAYER, R.C. 1996 Dynamics of the free rise of a light solid sphere in liquid. *AIChE* **42**, 1789–1792.
- KOK, J. B. W. 1989 Dynamics of gas bubbles moving through liquid. Ph.D. thesis, University of Twente.
- KOK, J.B.W. 1993a Dynamics of a pair of gas bubbles moving through liquid part I. Theory. *Eur. J Mech., B/Fluids* **12**, 515–540.
- KOK, J.B.W. 1993b Dynamics of a pair of gas bubbles moving through liquid part II. Experiment. *Eur. J Mech., B/Fluids* **12**, 541–560.
- LAMB, H. 1932 *Hydrodynamics*. Dover, 6th edn.
- LAMMERS, J. H. & BIESHEUVEL, A. 1996 Concentration waves and the instability of bubbly flows. *J. Fluid Mech.* **328**, 67–93.
- LANCE, M. & BATAILLE, J. 1991 Turbulence in the liquid phase of a uniform bubble air-water flow. *J. Fluid Mech.* **222**, 95–118.
- LEVICH, V. 1962 *Physico-Chemical Hydrodynamics*. Prentice Hall.
- LONGUET-HIGGINS, M. S., KERMAN, B. R. & LUNDE, K. 1991 The release of air bubbles from an underwater nozzle. *J. Fluid Mech.* **230**, 365–390.
- LUNDE, K. & PERKINS, R.J. 1995 A method for the detailed study of bubble motion and deformation. In *Advances in Multiphase Flow* (eds. A. Serizawa, T. Fukano & J. Bataille), pp. 395–405, Elsevier Science Publishers.
- LUNDE, K. & PERKINS, R.J. 1997 Observations on wakes behind spheroidal bubbles and particles. No. FEDSM97-3530. ASME-FED Summer Meeting, Vancouver, Canada.
- MAGARVEY, R. H. & BISHOP, R. L. 1961 Transition ranges for three-dimensional wakes. *Can. J. Physics* **39**, 1418–1422.

- MAGARVEY, R.H. & BISCHOP, R.L. 1961 Wakes in liquid-liquid systems. *Phys. Fluids* **4**, 800–805.
- MAGNAUDET, J. & EAMES, I. 2000 The motion of high-Reynolds-number bubbles in inhomogeneous flows. *Ann. Rev. Fluid Mech.* **32**, 659–708.
- MANASSEH, R., YOSHIDA, S. & RUDMAN, M. 1998 Bubble formation processes and bubble acoustic signals. *Proc. Third Int. Symp on Multiphase Flows* .
- MAXWORTHY, T., GNANN, C., KÜRTEEN, M. & DURST, F. 1996 Experiments on the rise of air bubbles in clean viscous liquids. *J. Fluid Mech.* **321**, 421–441.
- MCLAUGHLIN, J.B. 1996 Numerical simulation of bubble motion in water. *J. Colloid Interface Sci.* **184**, 614–625.
- MERCIER, J., LYRIO, A. & FORSLUND, R. 1973 Three-dimensional study of the nonrectilinear trajectory of air bubbles rising in water. *Trans. ASME, J. App. Mech.* **40**, 650–654.
- MIKSYS, M., VANDEN-BROECK, J.-M. & KELLER, J.B. 1981 Axisymmetric bubble or drop in a uniform flow. *J. Fluid Mech.* **108**, 89–100.
- MINNAERT, M. 1933 On musical air bubbles and the sound of running water. *Phil. Mag.* **16**, 235–248.
- MOORE, D.W. 1963 The boundary layer on a spherical gas bubbles. *J. Fluid Mech.* **16**, 161–176.
- MOORE, D.W. 1965 The velocity rise of distorted gas bubbles in a liquid of small viscosity. *J. Fluid Mech.* **23**, 749–766.
- NATARJAN, R. & ACRIVOS, A. 1993 The instability of the steady flow past spheres and disks. *J. Fluid Mech.* **254**, 323–344.
- POORTE, R.E.G. 1998 On the motion of bubbles in active grid generated turbulent flows. Ph.D. thesis, University of Twente.
- RYSKIN, G. & LEAL, L.G. 1984a Numerical solution of free-boundary problems in fluid mechanics. Part 1. the finite-difference technique. *J. Fluid Mech.* **148**, 1–17.
- RYSKIN, G. & LEAL, L.G. 1984b Numerical solution of free-boundary problems in fluid mechanics. Part 2. buoyancy-driven motion of a gas bubble through a quiescent liquid. *J. Fluid Mech.* **148**, 19–35.
- SAFFMAN, P. G. 1956 On the rise of small air bubbles in water. *J. Fluid Mech.* **1**, 249–275.
- SAFFMAN, P. G. 1992 *Vortex dynamics*. Cambridge University Press.
- SMITH, T. B. & BEESMER, K. M. 1959 Contrail studies of jet aircraft. No. ASTIA AD 217 188. Meteorology Research Inc.
- SPELT, P. D. M. & BIESHEUVEL, A. 1997 On the motion of gas bubbles in homogeneous isotropic turbulence. *J. Fluid Mech.* **336**, 221–244.
- SPELT, P. D. M. & BIESHEUVEL, A. 1998 Dispersion of gas bubbles in homogeneous isotropic turbulence. *Appl. Sci. Res.* **58**, 463–482.

- STEWART, C.W. 1995 Bubble interaction in low-viscosity liquids. *Int. J. Multiphase Flow* **21**, 1037–1046.
- SYNGE, J.L. & LIN, C.C. 1943 On a statistical model of isotropic turbulence. *Trans. R. Soc. Can.* **3**, 45–79.
- TAKAGI, S., MATSUMOTO, Y. & HUANG, H. 1997 Numerical analysis of a single rising bubble using boundary-fitted coordinate system. *JSME B* **40**, 42–50.
- TAKAGI, S., PROPERETTI, A. & MATSUMOTO, Y. 1994 Drag coefficient of a gas bubble in an axisymmetric shear flow. *Phys. Fluids* **6**, 3186–3188.
- THEOFANOUS, T.G. & SULLIVAN, J. 1982 Turbulence in two-phase dispersed flows. *J. Fluid Mech.* **116**, 343–362.
- TSAO, H.-K. & KOCH, D.L. 1997 Observations of high Reynolds number bubbles interacting with a rigid wall. *Phys. Fluids* **9**, 44–55.
- TSUGE, H. & HIBINO, S.-I. 1977 The onset conditions of oscillatory motion of single gas bubbles rising in various liquids. *J. Chem. Eng. Japan* **10**, 66–68.
- WEGENER, P. P., SUNDELL, R.E. & PARLANGE, J.-Y. 1971 Spherical cap bubbles rising in liquids. *Z. Flugwiss.* **19**, 347–352.
- WIDNALL, S. E., BLISS, D. & ZALAY, A. 1971 Theoretical and experimental study of the stability of a vortex pair. In *Aircraft Wake Turbulence and its Detection* (eds J.H. Olsen, A. Goldberg & M. Rogers), pp. 305–338, Plenum Press.
- VAN WIJNGAARDEN, L. 1968 On the equations of motion for mixtures of liquid and gas bubbles. *J. Fluid Mech.* **33**, 465–474.
- VAN WIJNGAARDEN, L. 1972 One-dimensional flow of liquids containing small gas bubbles. *Ann. Rev. Fluid Mech.* **4**, 369–397.
- VAN WIJNGAARDEN, L. 1976 Hydrodynamic interaction between gas bubbles in liquid. *J. Fluid Mech.* **77**, 27–44.
- VAN WIJNGAARDEN, L. 1988 Flow of bubbly liquids. *Theoretical and Applied mechanics* **17**.
- VAN WIJNGAARDEN, L. 1993 The mean rise velocity of pairwise-interacting bubbles in liquid. *J. Fluid Mech.* **251**, 55–78.
- VAN WIJNGAARDEN, L. 1998 On pseudo turbulence. *Theor. Comp. Fluid Dyn.* **10**, 449–458.
- VAN WIJNGAARDEN, L. & KAPTEYN, C. 1990 Concentration waves in dilute bubble/liquid mixtures. *J. Fluid Mech.* **212**, 111–137.

SUMMARY

Bubbly flows are very common in both industrial and natural environments. In general bubbly flows are very complex. Detailed knowledge about all phenomena involved should be obtained to predict the behaviour of the bubbles and the implications on the flow. In this thesis the focus is on the motion and the flow around a single bubble in quiescent water.

One part of this thesis concerns the study of the path and the path instability of a single bubble. Although in general liquids are contaminated, the present experiments are performed in pure water to eliminate as many sources of disturbances as possible. A three dimensional schlieren visualisation technique has been developed to study the path of and the flow around a bubble without affecting the purity of the water. The shape oscillations generally observed at the bubble release have not been observed for the present bubble-generation method.

Based upon the experimental observations, a model is proposed to explain the spiralling and zigzagging motion of free rising bubbles. It was found that a lift force is crucial for the dynamics of these free rising, path unstable bubbles. The path of a zigzagging bubble appears not to be maintained by a periodic shedding of vorticity, but by a reconnection of vorticity in the wake. Subsequently a change of sign of the strength of the trailing vortex filaments, as a consequence of the change of the direction of the lift force. At the onset of path instability no standing eddy was observed experimentally nor appeared numerically.

Most (bubbly) flows are bounded by solid walls. Therefore also the interaction of a single bubble with a solid wall is studied. Some peculiar phenomena have been observed for a bubble near a vertical wall. Four distinct types of interactions were observed as bubble sizes increase: i) sliding along the wall, ii) 'nose-like' shapes of multiple bounces, iii) bouncing followed by separation and iv) reappearance of multiple bounces of symmetric appearance. In several cases the bounce amplitude was observed to increase. A comparison has been made with the observations and transition parameters for a bouncing bubble pair, investigated by Kok (1993a, b) and Duineveld (1994).

Based upon these experiments a bouncing criterion is determined and a model is

proposed which captures the most important phenomena. In addition to the bouncing criterion, it appears that again the wake again plays a crucial role. Furthermore the 'nose-like' type of bounces have been associated with a strong reduction of the attractive force of the wall just after collision. At bouncing a vortical region is formed near the wall, which develops into a spherical shape and has a self-induced vertical motion.

The observations for the single bubbles have resulted in a model for the modification of turbulence by bubbles. This model is based on vorticity shedding from the bubbles. A lower and upper bound was determined for the excess turbulent energy. These results have been compared to experimental data found in literature.

SAMENVATTING

Bellenstromingen komen veel voor in industriële en natuurlijke omgeving. In het algemeen zijn belenstromingen erg complex. Gedetailleerde kennis over alle aanwezige fenomenen is nodig om het gedrag van de belen en de implicaties voor de stroming te voorspellen. In dit proefschrift wordt vooral aandacht besteed aan de beweging van, en de stroming om, een enkele opstijgende bel in stilstaand water.

Een deel van dit proefschrift richt zich op het bestuderen van de baan en de baaninstabiliteit van een enkele vrij opstijgende bel. Alhoewel in het algemeen vloeistoffen verontreinigd zijn, zijn de huidige experimenten in puur water verricht om zoveel mogelijk verstoringen uit te sluiten. Een drie dimensionale optische meettechniek, schlieren, is gebruikt voor het visualiseren van het zog achter een opstijgende bel. Hiertoe is er een temperatuur gradient aangebracht in de waterbak. Doordat de brekingsindex van water een functie van de temperatuur is, kan naast de contour van de bel ook het zog zichtbaar gemaakt worden. De zuiverheid van het water is door het gebruik van deze meetmethode niet aangetast.

De grootte van de belen wordt geregeld door middel van het volume en/of de druk van zuivere lucht. De bel wordt langzaam door een smalle buis geduwd met behulp van zuiver water. Het uiteinde van deze buis bevindt zich in de waterbak. De bel wordt op deze buis gezet en de bel is op dit moment bolvormig. Overal om de bel heen, ook binnen in de buis, bevindt zich nu zuiver water. Bij het loslaten van de bel is deze dus bolvormig; zonder volume of oppervlakte oscillaties. Deze oscillaties zijn in het algemeen wel aanwezig in eerdere onderzoeken en blijken een grote invloed te kunnen hebben op de baan van de bel.

In de huidige experimenten stijgt elke bel eerst recht op. Kleine belen stijgen in stilstaand water altijd recht op. Als het volume van de bel echter een bepaalde grootte overschrijdt, blijken de belen ook in de horizontale richting te gaan bewegen. Deze belen kunnen een spiraalbaan of een zigzagbaan beschrijven. Een zigzagbaan is een beweging in één vlak. Uit de experimenten is gebleken dat het zog van kleine, recht opstijgende, belen een enkele draad is. Het zog van spiraliserende en zigzaggende belen is opgebouwd uit twee draden, zolang de baan geen buigpunt vertoont. Verdwijnt de kromming, dan kan de baan echter ook weer lokaal rechtlijnig bewegen. Op

dat moment is het zog weer opgebouwd uit een enkele draad.

Uit de dynamica van het dubbele zog en de instabiliteiten van dit zog, blijkt dit zog grote overeenkomsten te vertonen met het zog achter een vliegtuig. Het zog is opgebouwd uit twee tegen elkaar indraaiende wervelbuizen en kan gerelateerd worden aan een lift kracht. Voor een spiraliserende bel is deze lift kracht van constante sterkte, geleidelijk veranderend van richting. Voor een zigzaggende bel verdwijnt deze liftkracht op het moment dat de baan rechtlijnig wordt. Uit de analyse volgt dat op dat moment de enige kracht loodrecht op de baan een component van de zwaartekracht is. Hierdoor kan er weer een kromming in de baan komen en er weer een dubbel zog ontstaan. Echter de draairichting van de wervelbuizen is nu tegengesteld en dus is de liftkracht van teken veranderd. Met behulp van het invoeren van de liftkracht kunnen de spiraal en zigzag baan van een bel verklaard worden.

Er is echter nog geen verklaring gevonden voor het ontstaan van de baan instabiliteit. Er is wel aangetoond dat deze niet veroorzaakt kan worden door het instabiel worden van een aangesloten zog achter een bel. Dit aangesloten zog is nooit gezien in onze experimenten en uit numerieke berekeningen blijkt dat dit aangesloten zog pas ontstaat in een parameter regime waarin de baan van een enkele opstijgende bel in zuiver stilstaand water al instabiel is. De baan instabiliteit van één bel is dus anders dan die van een vaste bol en rechtvaardigt daarmee de behoefte van experimenten in zuiver water, daar het gedrag van een bel in voldoende vuil water identiek is aan het gedrag van een vaste bol. Naar aanleiding van het huidige onderzoek zijn er twee mogelijk kandidaten voor het ontstaan van baan instabiliteit: een oppervlakte golf en symmetrie breking van het zog.

In de meeste (bellen) stromingen zijn wanden aanwezig. Daarom is er in dit proefschrift ook aandacht besteed aan het gedrag van een bel bij een verticale wand. Hierbij zijn er enige erg interessante verschijnselen geobserveerd: i) glijden langs de wand, ii) 'neusvormige' banen tussen opeenvolgende stuits, iii) enkele stuit, iv) hoge, opeenvolgende, symmetrische stuits. De hoogte van de stuit kan groter zijn dan de initiële afstand van de wand, en groter zijn dan de hoogte van de voorgaande stuit.

Deze verschijnselen hebben grootte overeenkomsten met gedrag van een bellenpaar. Dit is niet verwonderlijk daar, in de limiet van een potentiaal stroming, een bel dicht bij een wand opgevat kan worden als een bellenpaar: de bel en zijn spiegelbeeld. In dit proefschrift zijn dan ook de bewegingsvergelijking van een bellenpaar gebruikt om de banen van de stuiterende bellen te verklaren. Uit de experimenten bleek dat er een botsingcriterium, $We_{cr} = 0.165$, bestaat dat de overgang tussen glijden en botsen typeert. Voor glijdende bellen (snel uitdovende stuits) kan de botsing opgevat worden als een elastische botsing ($u \rightarrow -u, v \rightarrow v$); voor stuiterende bellen ($u \rightarrow -u, v \rightarrow 0$). Deze voorwaarde, het onttrekken van kinetische energie voor een stuiterende bel, kan verklaren waardoor de amplitude van een stuit kan groeien. Dit komt doordat de aantrekkende kracht van de wand recht evenredig is met het

kwadraat van de totale snelheid. Voor een stuitende bel kan de aantrekkende kracht vlak na de stuit significant kleiner zijn dan vlak voor de stuit en kan deze met dezelfde horizontale impuls verder van de wand komen. Ook kan hiermee de neusvormige baan verklaard worden.

Voor grote stuitende bellen zijn de banen niet rechtstreeks te beschrijven met het model. In overeenstemming met de vrij opstijgende bellen, blijkt dat er ook nu weer een dubbel zog gevormd wordt. De hieraan gerelateerde liftkracht blijkt altijd aantrekkend te zijn. Door deze, voor grote bellen, mee te nemen in het model kunnen de banen van stuitende bellen kwalitatief beschreven worden.

Met de waarnemingen voor enkele bellen is een model opgesteld om de invloed van vele bellen in een turbulente stroming op de turbulente energie te bepalen. Dit model berust op het feit dat de vorticeiteit geproduceerd aan het bel oppervlak zich herorienteert in bolvormige vorticeiteits gebieden. Op deze manier zijn een onder en een boven grens voor de extra turbulente energie geschat. De resultaten zijn in overeenstemming met experimentele resultaten uit de literatuur.

ACKNOWLEDGEMENTS

In February 1997, I started my research in the Fluid Dynamics Group in Enschede. I would like to thank everybody who, to a different degree of involvement, have contributed to the completion of this work.

I would first like to express my gratitude to Leen van Wijngaarden. Although he retired in March 1997, he agreed upon supervising me. In fact, I felt privileged to be invited for his retirement symposium, being a starting scientist among the many 'famous' researchers. In particular, I am grateful for the motivating and stimulating discussions and the never ending friendliness.

I would also like to thank Arie Biesheuvel for his supervision during these troublesome years. The lively discussions and opposition encouraged me to fully understand the problems and provide proof for my statements.

In 1997 the group was split into a Mechanical Engineering part, chaired by Harry Hoeijmakers, and an Applied Physics part, chaired by Detlef Lohse. I would like to thank both for giving me the opportunity to finish my research, make use of their facilities, and the many remarks and suggestions.

I would like to thank Andrea Prosperetti for the motivating and stimulating discussion and the opportunity to visit his group at the Johns Hopkins University in Baltimore. I would like to thank Shu Takagi for giving me the opportunity to use his numerical code and the help by the adaptations. For the latter I would also like to thank Emmanuel Ory.

The final results in the experimental work would not have been obtained without the support of the technicians. I would like to thank Henni Scholten and Gert wim Bruggert for their invaluable contributions. Furthermore they provided me parts of my "Twents" accent. I thank Wouter den Breeijen for keeping the computers running at most times.

A very important factor is the working environment. I would like to thank all staff, PhD students and students of both groups for their support. Especially I would like to thank the secretaries Marianne, Susan and Yvonne. And of course, special thanks to the students Jan Aiso Lycklema a Nijeholt, Michiel Houkema, Wilbert Grevers and Giel Linthorst whose work can be found throughout this thesis.

Another part of the working environment are the contacts with other researchers in the field of fluid dynamics. I would like to thank all these researchers for the stimulating discussions, the many remarks and the enjoyable chats. In particular I am grateful for the possibilities offered by the Burgerscenter and FOM.

But maybe even the most important factor is the social environment. I would like to thank all members of the kayak club DKV Euros for the physically necessary training and relaxation, and all instructors of Brandsport for the challenging and enjoyable times. Furthermore I would like to thank my family. Ultimately, I am grateful to Marit van Lunssen for the support and patience throughout the completion of this thesis.

Antoine de Vries
Enschede, February 2001

ABOUT THE AUTHOR

Antoine de Vries was born on June 10, 1972 in Sittard. He lived in Geleen and graduated from Sint Michiel high school (VWO) in 1990. During these years he played soccer at a RKSVD Lindenhevel. After graduation he went to the University of Twente to study Applied Physics. He became a member of the student kayakclub DKV Euros and soon became interested in white water kayaking. In 1992 he became an outdoor instructor in the weekends and summer holidays. He fulfilled his trainee-ship in 1995 at the University of South Australia, under the supervision of Dr. Stan Miklavcic and Prof. Roger Horn on the subject of the drainage of thin liquid films. In 1996 he graduated in the Fluid Mechanics and Heat Transfer Group of the University of Twente on the subject of mixing behaviour of the 2D cavity transfer mixer under supervision of Dr. Arend Woering. In 1997 he started the research reported in this thesis in the same Fluid Mechanics and Heat Transfer Group under supervision of Dr. Arie Biesheuvel and Prof. Leen van Wijngaarden. During his PhD he was a representative of his Group and the University of Twente in the Burgerscenter, the national Research School for Fluid Mechanics.



The author enjoying Fluid Dynamics in all its aspects, GOSLO-tour 2000.